This is to certify that the

dissertation entitled

Proximity Induced Superconductivity
in Multilayered Metallic Systems

presented by

Michael L. Wilson

has been accepted towards fulfillment
of the requirements for

PhD degree in Physics

Major professor

Date Feb 14, 1994

PROXIMITY INDUCED SUPERCONDUCTIVITY IN MULTILAYERED METALLIC SYSTEMS

by

Michael L. Wilson

A DISSERTATION

submitted to
Michigan State University
in partial fulfillment of the requirements
for the degree of

DOCTOR OF PHILOSOPHY

Department of Physics and Astronomy

1994

ABSTRACT

PROXIMITY INDUCED SUPERCONDUCTIVITY IN MULTILAYERED METALLIC SYSTEMS

by

Michael L. Wilson

The superconducting transition temperature T_c and superconducting upper critical field $H_{c2}(T)$ have been measured in the proximity coupled superconductor/normal-metal multilayered system Nb/CuX, where CuX represents Cu, $Cu_{1-y}Mn_y$, or $Cu_{0.95}Ge_{0.05}$. This represents the first study in which a single system has been used to examine the proximity effect through independent variation of the superconductor layer thickness d_s, and the normal-metal layer thickness d_n, concentration of magnetic impurities y, and resistivity ρ_n. The dependence of T_c on d_n reveals that Ge atoms elastically scatter proximity induced superconducting pairs in the normal metal layer N, while Mn impurities predominantly act as pair breakers, destroying the induced superconducting state. At a fixed d_n, the variation of T_c with changing d_s exhibits scaling consistent with the equation $\left(T_c^b - T_c\right)/T_c^b \cong \left(d_s/d_o\right)^{-p}$ where d_o is a scale length and T_c^b is T_c for bulk Nb. The exponent p increases systematically as either d_n or y increase, but is unchanged by the addition of Ge to the Cu layer. This scaling form is consistent with the limiting forms of two proximity effect theories. Quantitative agreement between the theories and the experimental data, however, is only achieved if T_c^b is allowed to decrease with decreasing d_s. The temperature dependence of the upper critical field $H_{c2}(T)$ was measured for

applied fields directed parallel and perpendicular to the plane of the layers $H_{c2\|}$ and $H_{c2\perp}$, respectively. The dependence of $H_{c2\perp}(T/T_c)$ follows trends similar to those of the T_c data, but $H_{c2\perp}$ appears to measure a slightly different superconducting pair penetration depth in N than does T_c. The behavior of $H_{c2\|}(T)$ changes from that indicating a 3D-coupled state near T_c, to a 2D-decoupled state below a temperature T^*. This dimensional crossover is described by a model in which the application of a field parallel to the layers predominantly destroys the induced superconductivity in the CuX layers without destroying the superconductivity in Nb. This model is opposed to earlier models of dimensional crossover which attribute crossover to the temperature dependence of the superconducting coherence length.

to my parents

ACKNOWLEDGEMENTS

I would like to thank Dr. Jerry Cowen for his guidance and support these last few years. I especially thank him for his patience during the writing and editing of this dissertation.

I also thank Dr. Carl Foiles for his many hours of discussions about structural analyses.

For their invaluable aid in maintaining my sanity during this project, I thank all the graduate students and staff at MSU. Special thanks, though, need to go out to Mike Jaeger, Dan Koppel, Roseann Miller, Diandra Leslie-Pelecky, and Reza Loloee. Their discussions have helped more than they probably know.

My parents also deserve special recognition since, without their support for the last 28 years, I could never have made it this far.

My greatest appreciation and thanks must extend to my wife Jennifer for keeping me going these last few years. Without her support, help, and even some needed prodding, I would probably still be writing.

Finally, I would like to thank the Department of Physics and Astronomy, the Center for Fundamental Materials Research, and the National Science Foundation for their financial support throughout my studies.

TABLE OF CONTENTS

LIST OF TABLES

LIST OF FIGURES

CHAPTER 1
INTRODUCTION

A superconducting metal (S), placed in physical contact with a normal, non-superconducting metal (N), can induce a superconducting pair density into N. This phenomenon, known as the proximity effect, is useful because it can be used to study the superconducting properties of traditionally non-superconducting materials.

One class of materials particularly suited to investigation using the proximity effect are magnetic materials. In typical bulk superconductors the addition of a few atomic percent of magnetic impurities destroys the superconducting state. This occurs because the superconducting state is composed of electrons whose spins are opposite to one another. When such a pair scatters from a magnetic ion, the electron spins are scattered into two unrelated spin states, thereby breaking the spin pair. This interaction is so strong that only in a few rare earth (RE) alloys and compounds can the magnetic impurity concentration be made high enough to observe effects related to interactions between the magnetic ions.[1] The properties of these RE systems, however, appear to be uniquely related to the f-band magnetic state of RE ions. Since the proximity effect can induce superconductivity into any normal metal, one can use the proximity effect to study the effect of magnetism on the superconducting state in any magnetic system.

Superconductor/ferromagnetic multilayers have been studied as candidate proximity effect systems in which to examine the behavior of coexistent magnetism and superconductivity.[2,3,4,5] Although the superconducting state for these materials has been observed at temperatures well below the magnetic phase transition temperature T_f, it has not been determined if the ferromagnetic state still exists below T_c.[4] In addition, one cannot easily examine the regime where T_f is of order T_c since the bulk T_f for most ferromagnets is two orders of magnitude greater than the T_c's of most conventional superconductors. Another difficulty of using these systems is that ferromagnets strongly break

superconducting pairs both because of their high concentration of magnetic spins and their spontaneous magnetization below T_f. Due to this effect, superconductivity can only be induced a short distance into the magnetic layer. Hence, to examine these systems in the layer thickness regime where superconductivity is induced within the entire magnetic layer one must use very thin layers where problems related to layer thickness uniformity and connectivity become severe.

To avoid some of these difficulties this thesis entails a study to determine if superconducting/spin-glass (SC/SG) multilayers can be used to study the interplay between magnetic and superconducting order. In particular, the multilayer system Nb/CuMn has been examined where Nb is a bulk SC and CuMn is a bulk SG. Due to the large spin of Mn in a Cu host ($S_{Mn} = 5/2$), one can shift smoothly from the non-magnetic limit to the strongly magnetic limit simply by increasing the Mn concentration y. Increasing y leads to an increase in the spin-freezing transition temperature of CuMn T_f and to a decrease in the electron mean-free-path ℓ_n. To correct for ℓ_n induced changes in the measured superconducting properties of these multilayers, the results were compared with those measured in Nb/CuGe samples. In a Cu host, Ge impurities are non-magnetic and lead to roughly the same increase in ℓ_n with impurity concentration as occurs in CuMn alloys.[6] CuGe layers are, therefore, expected to correctly model changes in the superconducting properties of these systems which are related to changes in ℓ_n. For simplicity in the following discussions, CuMn and CuGe will generically be denoted CuX.

There are several advantages to using spin-glasses over ferromagnets in these studies:

1. CuMn is a dilute magnetic alloy that undergoes a magnetic phase transition into a state having no net magnetization. Therefore, the superconducting pair penetration depth should be much larger for CuMn than it was for ferromagnetic layers and more easily used deposition techniques can be used to fabricate the samples.

2. The dependence of T_f on the CuMn layer thickness d_n, the Nb thickness d_s, and the Mn concentration y is fairly well known.[7,8] Therefore, T_f can easily be adjusted to fall near or below T_c.

The primary disadvantage to using spin-glass layers is that any interactions between the superconducting and magnetic states are likely to be weak. This is the result of the weakly-coupled magnetic state and the dilute magnetic ion concentration of spin-glass alloys. Hence, the main problem in establishing if SC/SG multilayers can be used to study interactions between superconductive and magnetic order will be understanding the superconducting properties of these materials well enough so that changes in the superconducting behavior of the samples can be related to a magnetic state, or to some other phenomenon—changes in crystal structure, effects due to the paramagnetic nature of the spins, effects related to ℓ_n, etc.

Few studies have examined the proximity effect in dilute magnetic N layers,[9,10,11,12,13] and none have studied these effects in multilayered systems. Therefore, this thesis focuses on the study of the dependence of T_c and the superconducting upper critical field, H_{c2}, on d_s, d_n, y, and ℓ_n.[14] It represents the first study in which such a wide range of material properties have been systematically varied within the same multilayered system.

To set the stage for the rest of this thesis, the remainder of this introduction discusses what is currently known about the superconducting state in proximity effect multilayers. Chapter 2 covers the details of sample preparation, and Chapter 3 covers sample characterization. The experimental section begins with Chapter 4 and a discussion of the experimental procedures used to take the T_c and H_{c2} data sets. Chapter 5 then presents the analyses of T_c, while Chapter 6 presents a discussion of the H_{c2} results. Chapter 7, then discusses what has been learned about the interplay between T_f and T_c. Finally, Chapter 8 summarizes the findings of this project.

1.1 Previous Studies of T_c and H_{c2} in Multilayered Superconductors

Even though the superconducting transition temperature is the easiest experiment with which to study multilayered superconductors, only three significant experiments on the dependence of T_c in multilayered superconductors have been performed: Bannerjee et al.[15] studied Nb/Cu multilayers; Missert and Beasley[16] studied S/N multilayers of the amorphous superconductor $Mo_{79}Ge_{21}$ and the amorphous metallic alloy $Mo_{1-x}Ge_x$; and Wong and Ketterson[2,4] studied superconducting/ferromagnetic V/Fe multilayers. The main findings of these studies are summarized below.

As d_n increases in V/Fe and $Mo_{79}Ge_{21}/Mo_{1-x}Ge_x$ multilayers T_c decreases monotonically until it saturates to a minimum value T_c^m for $d_n > d_{nc}^*$. For layer thicknesses greater than d_{nc}^*, pairs cannot cross N without being broken. Therefore, d_{nc}^* is proportional to the superconducting-pair penetration depth in N. Wong and Ketterson indicate that d_{nc}^* may decrease slightly with decreased d_s. Missert and Beasley found that in $Mo_{1-x}Ge_x$ alloys d_{nc}^* increases as the electron mean free path ℓ_n increases. Therefore, the pair penetration depth appears to increase with increased electron mean free path, and may depend slightly on the S layer thickness.

T_c^m was observed to decrease with increasing ℓ_n in the $Mo_{79}Ge_{21}/Mo_{1-x}Ge_x$ series. While this trend is readily apparent in the data, Missert and Beasley did not speculate on a cause. One possibility, however, is that increased ℓ_n leads to a greater ability for superconducting pairs to enter N and subsequently be broken. This idea will be discussed again in Chapter 5.

In Nb/Cu multilayers having $d_s = d_n = d$, Bannerjee et al. found that T_c decreased more rapidly with decreasing d than could be explained using the available proximity effect models.[15,17] They attributed this discrepancy to a decrease in the effective bulk superconducting transition temperature of Nb, T_c^e, with decreased d_s. In thin Nb films, the electron mean free path ℓ_s is dependent on the mean crystallite size and both are typically $\leq$

d_s. Hence, the reduction in T_c^e is related to a reduction in ℓ_s. Such a dependence of T_c on ℓ_s is known to occur in radiation damaged Nb samples,[18,19,20] and has been associated with broadening of a peak in the electronic density of states of Nb near its Fermi energy. As this peak broadens it leads to a decrease in the density of states at the Fermi level, which in turn leads to a decrease in T_c^e.

In the limit that $d_n \rightarrow 0$, T_c should approach the bulk superconducting transition temperature of S. If however, T_c was reduced by structural disorder within the S layer, this disorder would remain constant as d_n decreased, and T_c would approach the effective bulk T_c discussed above. In V/Fe multilayers, $T_c(d_n \rightarrow 0)$ is independent of d_s as is expected since V does not have a sharp peak in its density of states near the Fermi energy. In $Mo_{79}Ge_{21}/Mo_{1-x}Ge_x$ multilayers, however, $T_c(d_n \rightarrow 0)$ appears to increase as ℓ_n increases. While noting that this effect existed, Missert and Beasley did not explain the observed difference between $T_c(d_n \rightarrow 0)$ and the true bulk transition temperature of $Mo_{79}Ge_{21}$.

One of the reasons that the T_c experiments have received so little attention may be because studies of the superconducting upper critical field H_{c2} have located a unique dimensional crossover transition. $H_{c2}(T)$ provides a measure of the superconducting coherence length in a plane perpendicular to the direction of the applied field, so that in multilayers, H_{c2} is strongly dependent on the angle between the field and the plane of the layers. There are two limiting values of $H_{c2}(\theta)$: $H_{c2\perp}$ for external fields directed perpendicular to the plane of the layers, and $H_{c2\parallel}$ for external fields directed parallel to the layers. $H_{c2\perp}$ has been related to the superconducting coherence length in the plane of the film ξ_{in} while $H_{c2\parallel}$ has been related to both ξ_{in} and to the coherence length perpendicular to the layers ξ_z.[21]

In most multilayer experiments, $H_{c2\perp}(T) \propto (T_c - T)$, as is found in typical bulk superconductors.[4,22,23,24,25] This indicates that for most multilayered systems, the temperature dependence of ξ_{in} is not strongly affected by the layering. In some V/Ag multilayers, however, Kanoda et al. observed a significant positive curvature of $H_{c2\perp}$ near T_c[25] which

became more noticeable as d_n and d_s were increased in tandem. They did not, however, study the curvature as d_n or d_s was varied independently. A curvature similar to this is predicted by the theoretical models of Biagi, Kogan, and Clem,[26] and Takahashi, and Tachiki (TT).[27] TT argue that the curvature is related to the variation of the pair density along a vortex line. As d_n or d_s increase, the pair density becomes more localized within the S layers and leads to the observed curvature. This is a very rough conjecture, and it will be reexamined in Chapter 6.

$H_{c2\|}(T)$ has proven particularly interesting. As the temperature T decreases below T_c, the temperature dependence of $H_{c2\|}$ changes from being indicative of a 3D coupled superconductor to that indicative of an isolated 2D superconductor. This behavioral change is related to a decoupling of the superconducting layers in a multilayered stack and has been argued to occur when ξ_z became approximately equal to a physical length scale ξ^* which is related to the two layer thicknesses.[24,25] The model used to interpret both these experiments begins near T_c, where ξ_z diverges as $(T_c - T)^{-1/2}$ and is larger than any physical length scale in the multilayer. Therefore, ξ_z is large enough to average over the superconducting properties of the S and N layers with behavior similar to that observed for $\xi(T)$ in bulk superconductors. As the temperature decreases, ξ_z decreases until it becomes approximately equal to ξ^*. At lower temperatures, ξ_z is too short to effectively couple superconductivity between two S layers, and the superconductive coupling and the 3D state are lost. While this model is in qualitative agreement with the previously published data,[24,25] there are some subtle problems with it which will be elucidated in the $H_{c2\|}$ section of Chapter 6.

To summarize, a good deal is known about the qualitative dependence of T_c and H_{c2} on such parameters as d_n, d_s, ℓ_n, and ℓ_s, but high quality quantitative information is still lacking. To provide this quantitative level of understanding, most of this thesis is spent in examining T_c and H_{c2} in S/N multilayers.

CHAPTER 2
SAMPLE PREPARATION AND FABRICATION

All of the samples used in these studies were created using the MSU condensed matter physics group sputtering system designed primarily by Dr. William Pratt Jr. and built by Simard Inc.[28] This system consists of an ultra-high-vacuum compatible chamber housing 4 sputtering guns and up to 16 substrates. The base pressure of this system, prior to sputtering, was 2.0×10^{-8} torr. This, along with the ultra high purity gases used in the sputtering process, limited background contamination of the gas in the chamber to less than 10 ppm. Most samples were deposited onto polished, single-crystal, (001)-oriented, Si substrates. Additional samples were made on glass, mica, and single-crystal KCl substrates which were used in a variety of analytical tests to be discussed in the structure section.

The remainder of this section will detail the substrates used, the general aspects of sputter deposition using this system, the temperature control systems for the substrates, the preparation of the initial sputtering targets, and the cleaning procedures used to insure a low level of contamination in the system.

2.1 The Substrates

The typical substrates used were of polished, boron-doped, single-crystal, (001)-oriented, Si. The dopant levels were such that the room temperature resistivity was at least 10 Ω·cm/□. A rather high resistivity substrate was chosen to avoid problems due to the possibility of measuring currents shorting out through the substrates.

Substrates were purchased as 3 inch diameter wafers from Silicon Quest International.[29] The wafers were cleaved into 1/2"x1/2" squares for use. The cleaving process

determined the use of (001)-oriented Si, other orientations ((111) in particular) proved difficult to cleave reliably.

2.2 Sample Mounting

The substrates were mounted in an aluminum holder as shown in Figure 2.1. The substrate temperature was stabilized during sample deposition by using a Cu block and foil to thermally link the substrate to the Al holder. Details of the temperature control scheme will be discussed below. The holder also employed a rotatable shutter so that only one of the substrates was used at any one time.

The 8 substrate holders, each holding 2 substrates, were arranged on the SPAMA (Substrate Positioning And Masking Apparatus) plate as shown in Figure 2.2. The position and orientation of the sample holders ensured that each substrate saw the same sputtering conditions. In addition to the substrate holders, the SPAMA plate also held two film thickness monitors, one each for Nb and CuX.

Substrates were cooled by a small liquid N_2 reservoir located near the SPAMA plate. This reservoir was thermally linked to the sample holders as shown in Figure 2.3. Incoming high pressure (1000 psi) N_2 gas passed through a thin stainless steel tube which was cooled by a liquid N_2 bath inside the sputtering chamber. This caused the high pressure gas to liquefy. The liquefied N_2 was then forced through a fine stainless-steel tube into a small reservoir near the SPAMA plate. Heat, deposited in the substrate by the incoming sputtered atoms was conducted off the sample by Cu foils and into the sample holder. Heat was then progressively transferred to the SPAMA plate, to a series of OFHC (Oxygen Free High Conductivity) Cu pieces and finally to the liquid N_2 reservoir. Evaporation of liquid N_2 then carried the heat energy out of the system. With this cooling

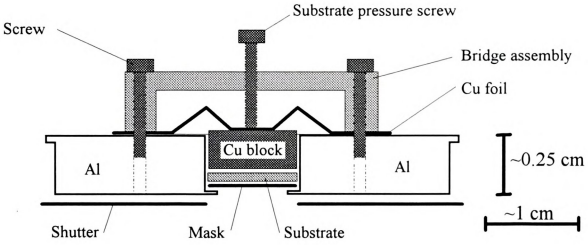

Figure 2.1: Sample holder

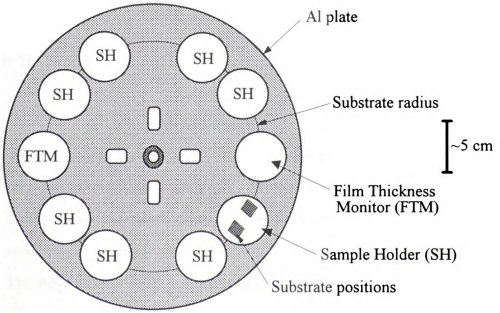

Figure 2.2: The sample positioning and masking apparatus (SPAMA) plate.

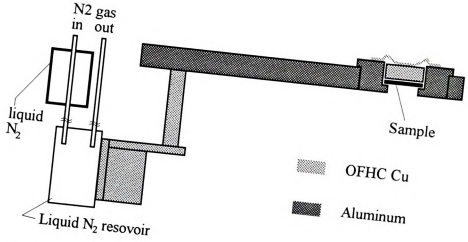

Figure 2.3: The substrate cooling system.

system in place, substrate temperatures were kept between -20 and +20°C for the duration of a sputtering run (typically 4-10 hours). Without cooling, the temperature of the SPAMA plate rose to over 100°C in approximately 1 hour.

2.3 The Sputtering Guns

The CFMR sputtering system contained four triode, magnetron, sputtering guns. A schematic of one gun is shown in Figure 2.4. In the sputtering process, ionized Argon atoms were accelerated toward the target. On impact with the target, the ion's kinetic energy was transferred to target atoms. These atoms were then ejected from the target surface resulting in a beam of target atoms.

The Argon atoms were ionized by stabilizing a highly energetic electric current between the anode and the filament. Typically, this current operated at 500 to 700 kV and 5 to 7 Amps. The energies of these electrons were high enough to knock electrons off any argon atoms which they struck, thereby creating a plasma. An applied magnetic field

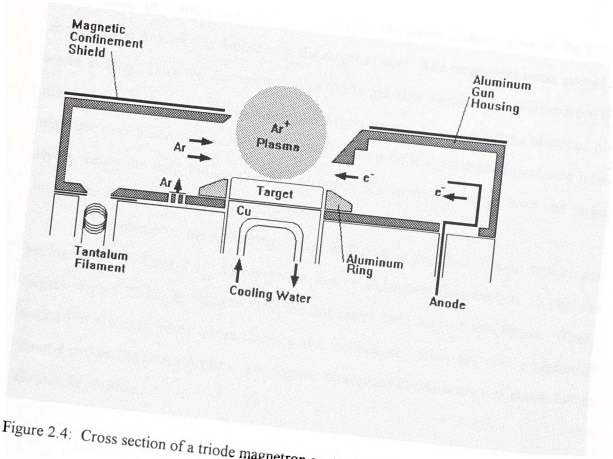

Figure 2.4: Cross section of a triode magnetron sputtering gun.

confined the Ar plasma to the region just above the target. A high negative potential was then applied between the Ar plasma and the target to accelerate the ions toward to target. Finally, a collimation shield limited the ejected material to a beam approximately 5 cm across.

Although material was readily ejected from the target surface, most of the kinetic energy of the Ar ions was deposited in the target as heat. The target was water cooled to avoid melting. Once the Argon ions struck the target, they acquired an electron from the metal surface and were reemitted as neutral Argon atoms. To provide these electrons one must use electrically conducting targets. This made it difficult to deposit insulating inter-layers, hence the only 'insulator' used was doped Si, where the dopant level and target temperature were high enough to allow sputtering to proceed.

A schematic of the sputtering system is shown in Figure 2.5, with typical gun settings listed in Table 2.1. The target to sample separation distance was 12 cm, the targets were 5.72 cm in diameter, and the collimator hole was ~5 cm across. These resulted in a atomic beam whose intensity was uniform to within 5% over a region of about 4 cm^2 on the SPAMA plate. The angular divergence of this beam was about 25° at the sample position.

Table 2.1: Sputtering gun settings.

Argon flow rate	35	cm^3/min
Anode-to-Filament potential	50-60	V
Anode-to-Filament current	5-7	Amp
Argon Plasma-to-Target potential	500-700	kV
Argon plasma-to-target current	0.5-1.1	mAmp

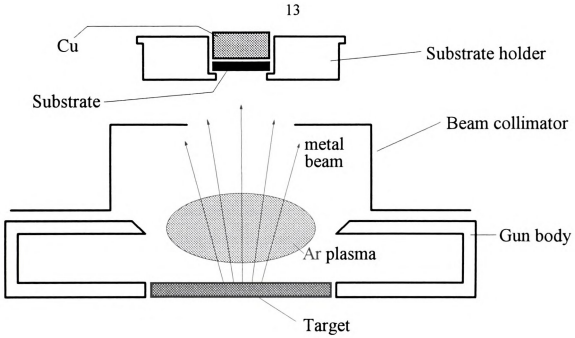

Figure 2.5: Overall view of the sputtering configuration.

All the activities of the sputtering system were coordinated by an external computer which directly controlled the angular position of the SPAMA plate, and performed all calculations and timing needed to deposit layers of the desired thicknesses. The computer system also monitored, but did not interactively control, the voltage applied to the sputtering target and the current passing through the target. These parameters were adjusted manually during each run to provide a constant sputter deposition rate. The actual deposition rate was measured a few times during each run using the film thickness monitors and manually entered into the computer. With this system, run-to-run variability of the deposited layer thicknesses were typically $\pm$5%.

2.4 Target Production and Preparation

Sputtering targets were cut to the desired cylindrical shape, 5.72 cm diameter by 0.64 cm thick, by the staff of the Physics Shop at MSU. Pure Nb and Cu targets were cut

from 0.64 cm thick plate obtained from Angstrom Sciences[30]. The purity of these bulk materials was 99.95% for Nb and 99.999% for Cu. The CuX alloy targets were cut from alloyed ingots fashioned here using an rf-induction furnace.

The alloy targets were made from 99.9999% pure Cu, 99.9% pure Mn, and 99.999 pure Ge, obtained from Aesar/Johnson Matthey inc.[31] The raw materials were cleaned in dilute nitric acid before being placed in a boron nitride lined graphite crucible. The boron nitride was needed to avoid carbon contamination of the alloy. This crucible was then placed in a vacuum chamber which was evacuated to $5x10^{-6}$ torr before alloying began. The chamber was then back filled to a pressure of ~250 torr using a 90 % Ar and 10 % H_2 gas mixture. The H_2 gas helped to remove residual oxygen from the system. The mixture was heated to a temperature between 1100 and 1150°C and the alloy was kept molten for ~15 minutes. It was then cooled slowly to avoid formation of cracks in the alloy block. To gain the maximum homogeneity, the block was typically inverted in the crucible and remelted at least one additional time. The final Ge and Mn concentrations were determined from EDX and magnetic measurements on thick sputtered films. These measurements will be detailed in the structural analysis section.

2.5 Cleanliness

Substrates were cleaned ultrasonically in acetone, and then alcohol. If residues remained on substrates after this procedure, the substrates were re-cleaned in hexane, followed by acetone, and then alcohol. A more lengthy cleaning procedure was avoided by keeping the substrates as clean as possible from the time the full wafers were removed from their factory container.

An acid etch consisting of a mixture of 50% HNO_3 and 50% water was used to clean most of the other parts of the sputtering system. These included the sample holders, sample shutters, SPAMA plate, sample masks, gun body, Al target confinement ring, and

film-thickness-monitor covers. Deposits not readily removed by the acid were scrubbed vigorously with a iron wire brush and then re-etched. Nb proved very difficult to remove from the gun parts because the Al metal of the gun parts etched away nearly as fast as the Nb deposits. A razor blade was used to scrape away most of the Nb deposits, after which approximately 5% HF was added to the acid solution to help remove the remaining Nb. The stainless steel sample masks are unaffected by HF, and were always etched with a HNO_3/water/HF solution. After the acid etch, all these parts were cleaned ultrasonically, using a process similar to that used for the substrates. The SPAMA plate is too large to fit in the ultrasound bath, and so was rinsed by hand with acetone and alcohol.

The shutters for the sputtered beams were never cleaned directly. Before each run, the collimating chimneys were covered with Al foil which was discarded at the end of the run. In addition, the iron magnetic confinement plates, sample bridge assemblies, Cu heat sinks and thermocouples were not cleaned before each run, but were simply kept clean between runs. These components were not cleaned because the were either, never in contact with the sputtered metal beam (and therefore have no significant deposits on them), were not in close proximity with the polished face of the substrate, or, in the case of the magnetic shield, were highly reactive in all acids, and so were discarded when their deposits became severe.

CHAPTER 3
STRUCTURAL ANALYSES

The purpose of structural analysis was to determine the internal structure of each sample and to identify structural trends that may effect its magnetic and conductive properties. To this end, the primary questions of interest were

- Were the samples layered?
- Were the layer thicknesses as expected from the sputtering conditions?
- Were the layer thicknesses uniform?
- Was the Nb/CuX interface sharp?
- What were the concentrations of desired and undesired impurities in the Nb and CuX layers?
- Were the Nb and CuX layers crystalline or amorphous?
- What were their crystallite sizes?
- Were there any changes in the Nb or CuX lattice spacings as the layer thicknesses were reduced?
- Were there strains in the Nb or CuX lattices near the Nb-CuX interface?
- Were the Nb or CuX crystallites preferentially oriented?

All these questions, with the exception of chemical impurity concentrations, were addressed by analyzing x-ray diffraction data taken on as-produced samples. Many of the x-ray diffraction results were also checked by studying x-ray absorption fine structure (XAFS) studies and cross-sectioned multilayer films. The cross-section experiments focused on imaging and electron diffraction. The chemical concentrations were determined using energy dispersive x-ray (EDX) analysis and, in the case of CuMn, by measuring the spin-freezing transition temperature.

3.1 Elemental Compositions

EDX and magnetic measurements were used to determine the concentrations of the various desired and undesired impurities in the layers. EDX measures the elemental compositions by exciting a sample with a high energy electron beam (typically 100-300 keV) and comparing the relative fluorescent x-ray line intensities from the host, Cu or Nb, and impurity atoms. These intensities were suitably normalized and compared with those expected from each pure material. For the CuGe alloy, EDX data provided the only measure of the Ge concentration, which was 4.9 ± 0.3 atomic percent (at. %) for the target used in these experiments. An analysis of EDX data also found no evidence for any unwanted impurities in either the Nb or CuX films above the detection limit (~0.1 at. %) of the method .

CuMn(y) is a spin-glass alloy with a magnetic phase transition which is sensitively dependent on the Mn impurity concentration y. The spin-glass freezing temperature is roughly given by

$$T_f = T_{f,o} y^{\upsilon} \qquad (3.1)$$

where y is the Mn impurity concentration in atomic percent (at. %) and $T_{f,o}$ and υ were derived from a least squares fit to data for $T_f(y)$ taken from the Landolt-Börnstein Tables.[32,33] A fit to these data for $y \leq 11$ at. % resulted in the values: $T_{f,o} = 9.89 \pm 0.27$ K and $\upsilon = 0.659 \pm 0.014$. Hence, a measurement of T_f provides values of y. For $y > 3$ at. %, magnetization and EDX measurements agreed to within 10%. Larger disagreements were observed at low y due to the increased difficulty of quantitative x-ray peak detection.

3.2 X-ray Diffraction

X-ray diffraction was used to study the spacing of atomic planes within the Nb and CuX crystal structures. An x-ray beam incident on a crystal will diffract from sets of atomic planes within that crystal because the x-ray wavelength is of the order of the planar spacings. The diffraction condition, known as Bragg's law, is

$$m\lambda_x = 2d\sin(\theta) \qquad (3.2)$$

where d is the spacing between two planes of atoms within a crystal, λ_x is the wavelength of the incident x-ray beam, m is the order number of the diffracted beam, and 2θ is the angle between the incident and diffracted x-ray beams.

3.2.1 The Diffractometer

All the x-ray data sets discussed in this section were taken on a Rigaku powder x-ray diffractometer. The general layout of this system is shown in Figure 3.1. The x-rays were emitted from a rotating Cu anode and collimated by a set of divergence slits. The divergence angle of the x-ray beam was set to $(1/6)^\circ$ for most scans. After the beam interacts with the sample, it was recollimated by a second set of slits and passed into a graphite monochrometer. This selected out Cu-K_α radiation from the total emission spectrum of the Cu source. The wavelength of Cu-K_α is 0.1542 nm.

The samples were mounted on the sample goniometer using an aluminum holder consisting of a flat Al sheet with four protruding feet on one side and a stainless steel spring clip on the back, as shown in Figure 3.2. This arrangement insured that the front surface of the sample was parallel to the front surface of the sample holder, the position required to ensure that the sample was in the proper alignment for the goniometer.

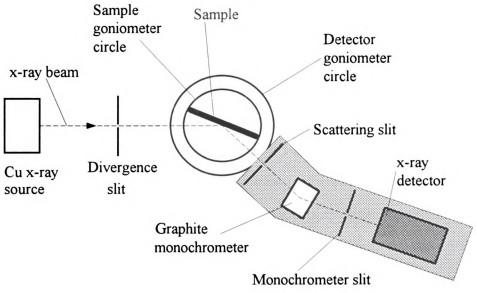

Figure 3.1: The x-ray diffractometer.

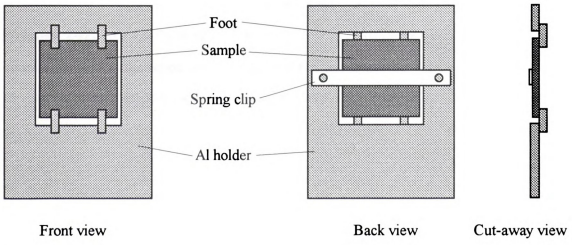

Figure 3.2: The x-ray diffraction sample holder.

Due to the fabrication tolerance of this holder (± 0.025 mm on each foot) the sample was parallel to the surface to within only ± 0.1°. This possible misalignment did not effect spectra for scanning at angles greater than ~10°, but may have induced small errors in the peak positions observed at smaller angles.

The sample and detector goniometer angles, α and 2θ respectively, are driven independently by computer. In the reflection geometry α was set equal to θ, hence, the incident and diffracted beams appeared to reflect from the sample surface. For the other common drive geometries the detector and sample angles were set so that $\alpha = \theta - \phi$, as shown in Figure 3.3. In the off-axis geometry ϕ was fixed and θ and 2θ were varied in tandem, while in the rocking curve geometry ϕ was varied for fixed θ and 2θ. These scans will be described in detail below.

The instrumental resolution of the apparatus was limited by two effects. The first was the inherent minimum line width measurable by the system. This width is primarily related to the widths of the various collimation slits used in the system. This led to an apparent x-ray line width ranging from 0.05° for $2\theta = 10°$ to 0.11° for $2\theta = 120°$. The second resolution limitation arose because the monochrometer was not sensitive enough to separate the narrowly spaced Cu-K_α doublet ($K_{\alpha 1}$ and $K_{\alpha 2}$). The effective peak

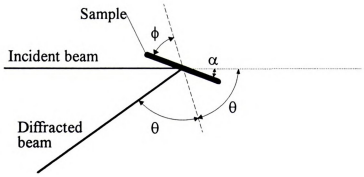

Figure 3.3: Definitions of scattering and goniometer angles.

separation of the $K_{\alpha 1}$ and $K_{\alpha 2}$ lines was 0.025° at 2θ = 10° and 0.49° at 2θ = 120°. Therefore, analysis of peak widths, to be described below, was not performed on peaks whose widths were comparable to either of these two instrumental widths.

3.2.2 Reflection Scans

In the reflection geometry, diffraction only occurs from planes of atoms parallel to the substrate, this results in a set of x-ray diffraction peaks related only to structure along a line normal to the sample. Such data measures the Nb and CuX lattice spacings, crystal structures, orientational texture of the metal film perpendicular to the layers, and the thicknesses of the two layers.

A reflection diffraction pattern for a Nb/CuMn(13%) 2.0 nm/2.0 nm sample is shown in Figure 3.4. Aside from the broad peak near 25° due to scattering from the amorphous glass substrate used for this sample, there are three regions of immediate interest. At small angles $0° < 2\theta < 9°$, a series of closely spaced peaks appear which are due to Bragg reflection from the bilayer periodicity Λ. This was the region of small-angle x-ray diffraction (SAXD). The peaks near 40° are first order (m = 1) while those near 90° are second order (m = 2) diffraction peaks from the Nb (110) and CuMn (111) planes. These three regions will be discussed in detail below following discussion of one broad feature typical of all spectra.

In Figure 3.4, no peaks were observed which could be related to scattering from any Nb or CuX crystal planes except for Nb (110) and (220) and CuX (111) and (222). This indicates that the Nb and CuX crystallites were oriented with these planes parallel to the substrate. This behavior was related to the type of film growth which occurs in sputter deposited films.

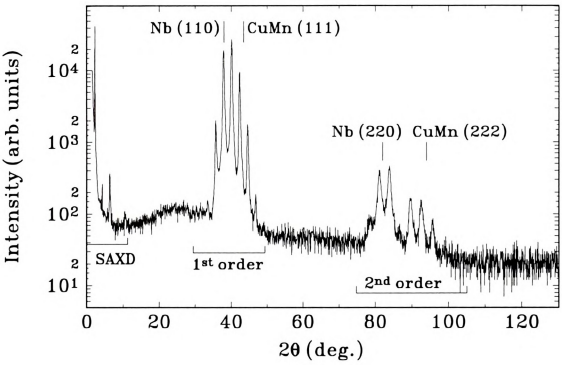

Figure 3.4: Full scattering spectra for a Nb/CuMn(13%) 2.0 nm/2.0 nm multilayer.

As each atom arrives on the film surface during film growth, it has enough energy to wander about on the surface before settling into a stable site. Due to this motion, the atom seeks out a position that maximizes the number of nearest neighbor bonds, resulting in the most densely packed atomic planes being oriented parallel to the surface of the sample. For the Nb bcc and CuX fcc lattices, the densest planes are the (110) and (111) planes respectively. Therefore, the deposition process lead to polycrystalline films with their Nb bcc (110) and CuX fcc (111) planes parallel to the sample surface. While these analyses imply that the growth process leads to oriented crystallites, it does not provide any information about the extent of orientational ordering within the film plane.

3.2.2.1 Small-Angle X-Ray Diffraction

In addition to the Nb (110) and CuX (111) lattice spacings there is a third structural periodicity perpendicular to the layers, the bilayer period: $\Lambda = n_{Nb}d_{110} + n_{CuX}d_{111}$, where n_{Nb} and n_{CuX} are the number of atomic planes within the Nb and CuX layers. This period is much larger than either d_{110} or d_{111}, therefore this period should produce diffraction peaks at very low angles. Furthermore, the Bragg condition is slightly modified in this regime because at low scattering angles ($< 5°$), the difference between the x-ray index of refraction in air and in a metal must be taken into account. In most metals, the index of refraction at x-ray wavelengths n_m is slightly less than that of air n_a, resulting in x-ray scattering as depicted in Figure 3.5. Based on this figure, Bragg's law was written

$$j\lambda = 2\Lambda \sin(\theta_m)$$

where j is the order number of the reflection.

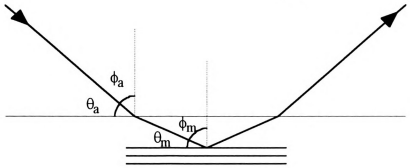

Figure 3.5: Low angle x-ray scattering in a metal film.

Snell's law was then used to relate θ_a to θ_m

$$n_m \sin(\phi_m) = n_a \sin(\phi_a) \tag{3.3}$$

where θ and ϕ are related by $\sin(\phi) = \cos(\theta)$. Then, n_a and n_m were set to 1 and $1-\delta$ respectively, and ϕ was replaced by θ in Snell's law to obtain (in the limit that $\delta << 1$):

$$\sin^2(\theta_a) \cong \sin^2(\theta_m) + 2\delta \tag{3.4}$$

which was used to replace θ_m by θ_a in Bragg's law. This finally lead to an equation relating the measured angle θ_a to Λ and δ:

$$\sin^2(\theta_a) \cong \left(\frac{\lambda}{2\Lambda}\right)^2 j^2 + 2\delta \tag{3.5}$$

Λ was then extracted from a least squares fit of $\sin^2(\theta_a)$ to j^2. A low angle data set and resulting fit are depicted in Figure 3.6.

The derived Λ's were typically within 7% of those expected from the fabrication conditions. Agreement between measured and expected values for Λ suffered in part

because of the small number (typically 2 to 4) of low angle peaks observed for each sample.

Reliable values for δ, the deviation of n_m from 1, were unobtainable from these fits because the internal accuracy of the low angle measurement in the Rigaku system was not high enough for such an analysis. Therefore, δ was only used as a fitting parameter.

3.2.2.2 First-order Region

Figure 3.7 shows x-ray diffraction data for two Nb/ CuMn(0.3%) multilayered samples, 70.0 nm/70.0 nm and 10.0 nm/13.0 nm. For large layer thicknesses [Figure 3.7(a)], the Nb and CuX bulk lines were virtually identical to those measured in bulk films. The widths of these lines were related to the average crystallite size perpendicular to the layers through Scherrer's equation:

$$S = \frac{\lambda_x}{\beta \cos(\theta)} \qquad (3.6)$$

where S is the crystallite size and β is the width of the diffraction peak in 2θ radians.[34] Using Equation (3.6), the crystallite sizes of thick Nb and CuX films were found to be approximately 25 nm .

As the layer thicknesses decreased, the Nb and CuX peaks broadened, but their positions remain unchanged [Figure 3.7(b)]. The crystal sizes obtained from the line width showed that the crystallites extended across the entire Nb or CuX layers. In addition, for Λ below about 30 nm, small satellite peaks appeared flanking the bulk peaks. The spacing of these peaks was directly related to Λ through Bragg's law with $m \sim 80$.

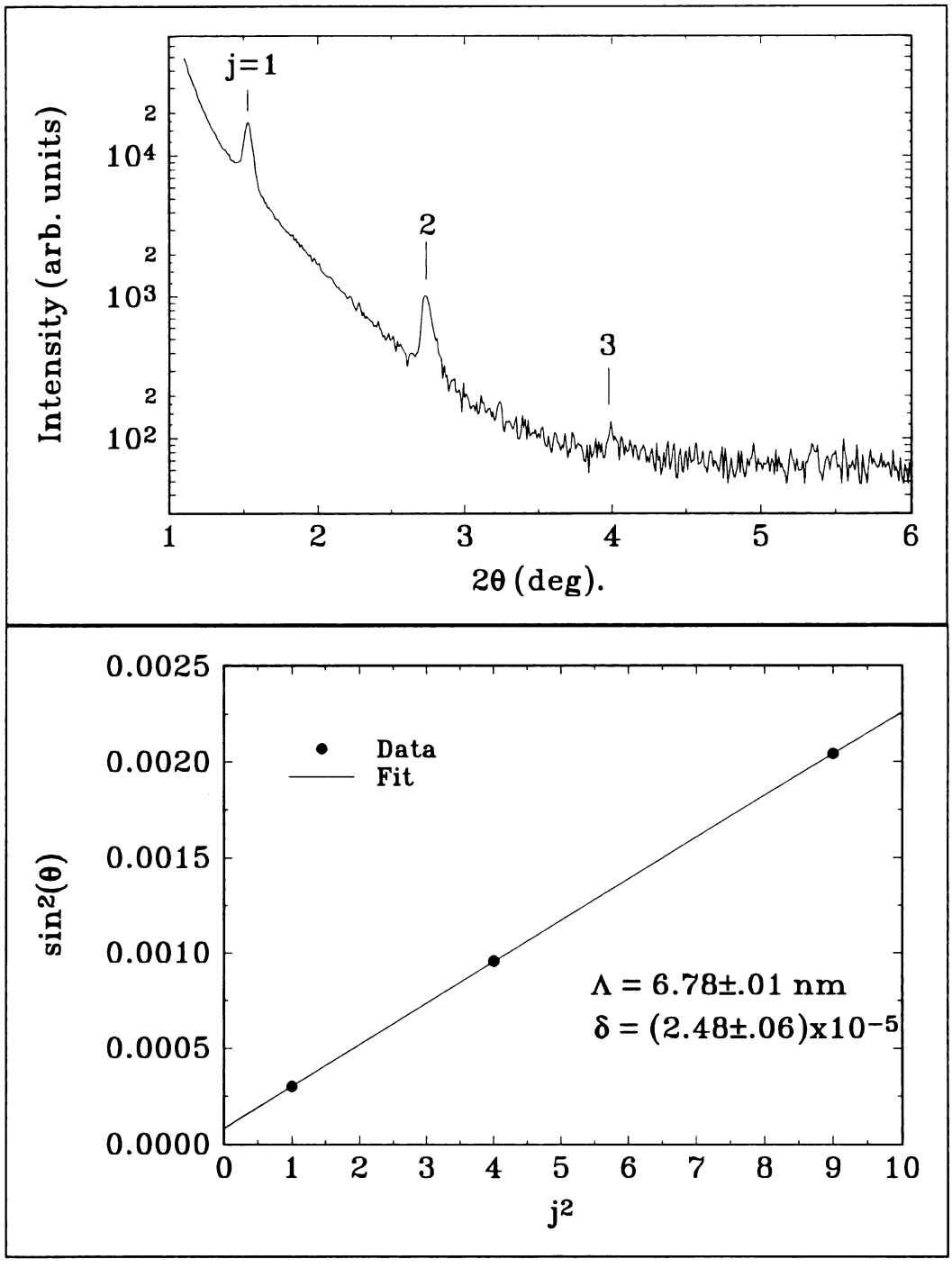

Figure 3.6: Small-angle diffraction scan and peak analysis used to determine Λ for Nb/ CuGe(5%) 5.0 nm/2.0 nm.

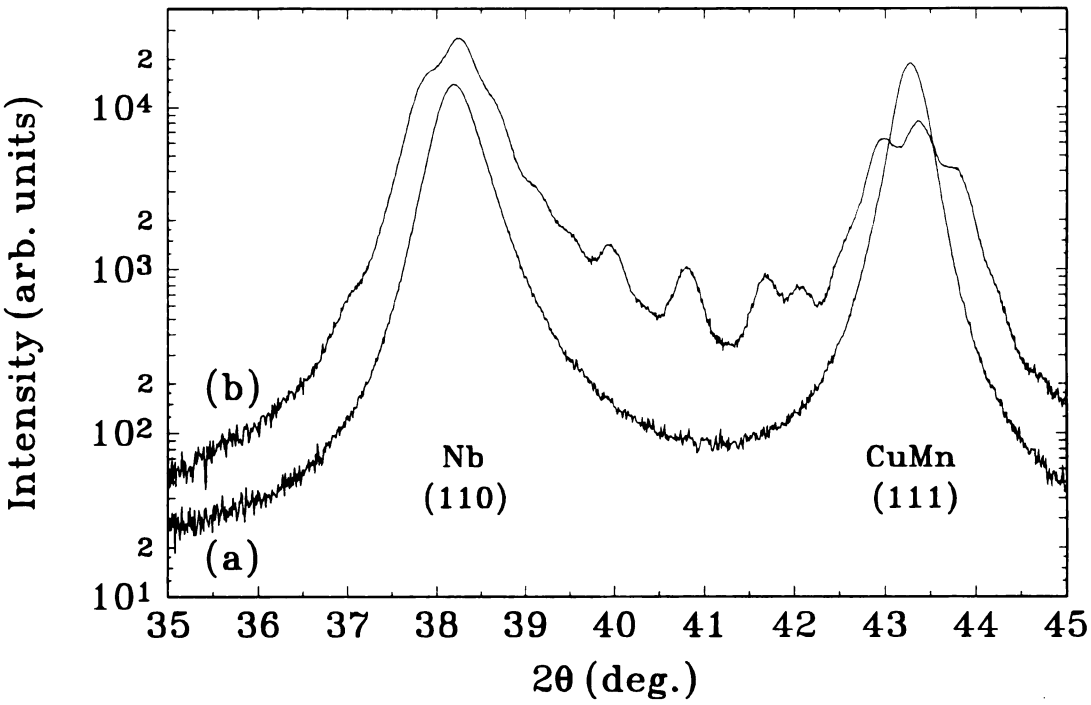

Figure 3.7: First order diffraction peaks for Nb/CuMn(0.3%) 70.0nm/70.0nm (a) and 10.0nm/13.0nm (b).

Λ was extracted from a least squares fit to Bragg's law as shown in Figure 3.8 for a Nb/CuMn(10%) 15.0 nm/7.0 nm multilayer. Due to the large number of satellites typically observed (5 to 12), the statistical uncertainty of the resulting Λ's was much lower than was the case with Λ derived from low angle data. The statistical and systematic errors of the x-ray determination were considered low enough that most of the observed deviations between fabricated and measured Λ's (~ 5%) were attributed to errors made during the fabrication process. This lead to the 5% uncertainty in deposited layer thicknesses quoted in the sample preparation chapter.

The peak widths are related to a Fraunhofer type diffraction pattern due to there being coherent diffraction within a single layer thickness. This results in there being an overall Fraunhofer type diffraction envelope which modulates the intensity of the satellites. This is clearly observed in Figure 3.8: the missing peaks (m = 3 and 6) occur at the minimum positions for a Fraunhofer pattern due to the 7.0 nm thick CuX layer. The Nb layer does not show a significant Fraunhofer pattern because its thickness is significantly larger than that of CuX.

For very small layer spacings (< 4 nm), the peak broadening due to decreased layer thickness became of order the separation between the bulk Nb and CuX peaks, and the bulk Nb and CuX lines were entirely washed out by the satellite peaks. Hence, for these small layer thicknesses, data taken at the first order peaks could not be used to determine the lattice parameters of the individual constituents.

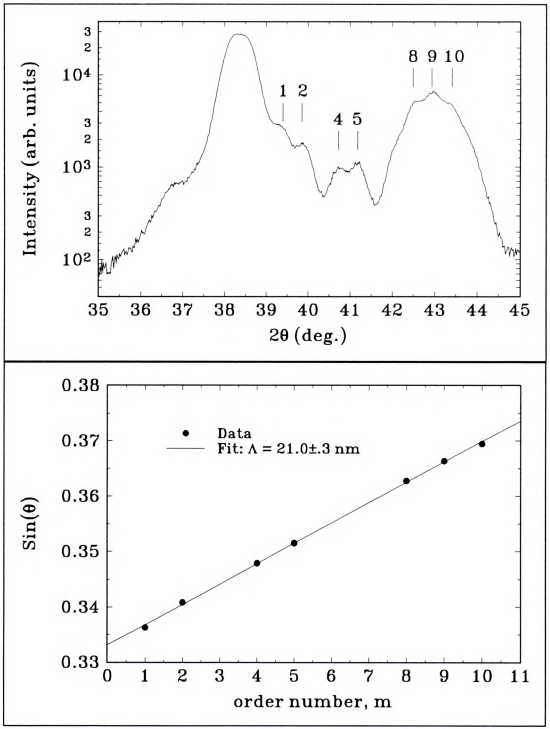

Figure 3.8: First order spectrum and peak analysis used to determine Λ for Nb/CuMn(10%) 15.0nm/7.0nm.

3.2.2.3 Second-order Region

The difficulty of resolving the bulk Nb and CuX peaks was avoided by examining the second order spectra. Here the enhanced resolution due to scattering at large angles allowed the lattice spacing of Nb and CuX to be determined on layer thicknesses down to 2.0 nm (Figure 3.9). By estimating an envelope for the Nb and CuX peaks sets, the lattice spacing can be calculated. The resulting spacings agreed to within 2% and 3% with the expected Nb and CuX spacings, respectively. In addition, the crystallite sizes determined from the Nb and CuX peak widths confirmed that the layer thicknesses were roughly equal to their expected values.

Fullerton et al.[35] recently developed a recursive x-ray diffraction modeling program to study layer thickness fluctuations in Nb/Cu multilayers. Their analysis of sputtered Nb/Cu 2.6 nm/2.6 nm multilayers showed that experimental observation of satellites associated with the Nb (220) and Cu (222) peaks placed an upper limit of 0.3 nm on the rms fluctuations in the two layer thicknesses. On the basis of the similarity in layer thicknesses and satellite structure of their published Nb/Cu data and the above Nb/CuX 2.0 nm/2.0 nm and 3.0 nm/3.0 nm data (Figure 3.9) we inferred that the rms fluctuations in the Nb and CuX layer thicknesses in our samples were no more than 0.3 nm. Satellites were observed near the Nb (220) and CuX (222) peaks for all samples with Nb thicknesses $\leq$ 6.0 nm and CuX thicknesses $\leq$ 5.0 nm. Since satellites could be resolved for these samples, there could be no large changes in the magnitude of layer thickness fluctuations for multilayers having layer thicknesses greater than 3.0 nm.

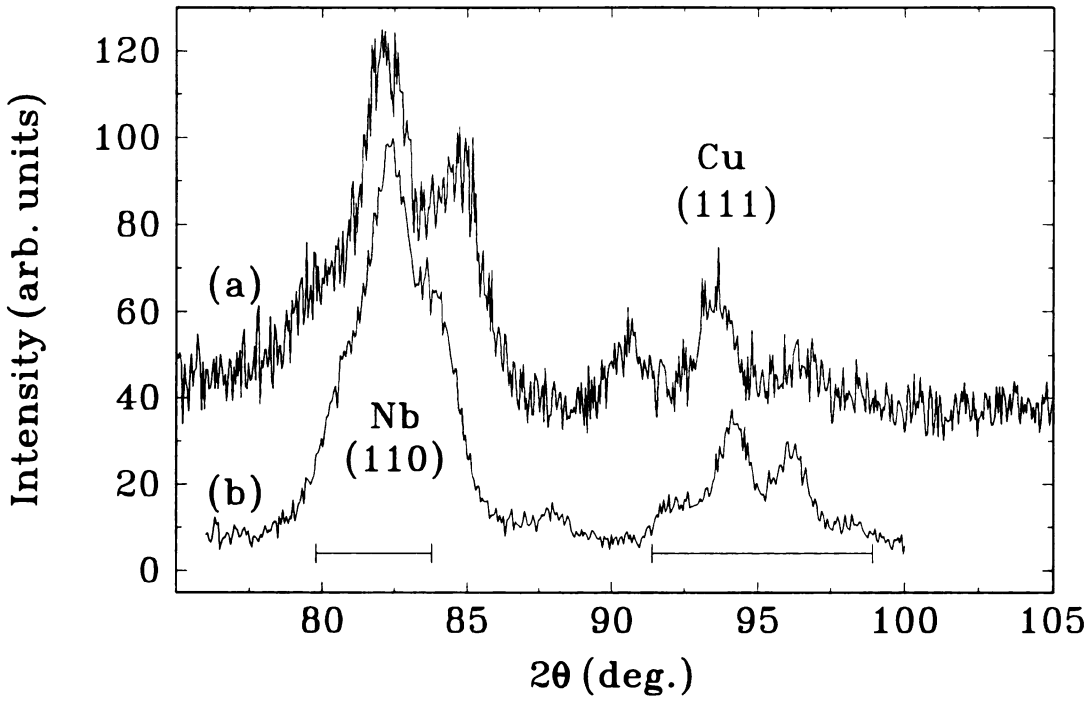

Figure 3.9: Second order peaks for a Nb/Cu 2.0 nm/2.0 nm (a) and a 3.0 nm/3.0 nm (b) multilayer. Error bars are bounds for a ± 2% change in d_{Nb}, and a ± 3% change in d_{CuX}.

Analysis of the reflection x-ray diffraction data shows that the Nb and CuX layers crystallized in their bulk crystal structures (bcc for Nb and fcc for CuX) with their bulk lattice spacings. The data showed that the Nb and CuX crystallites were preferentially oriented with their Nb (110) and CuX (111) planes roughly parallel to the substrate. This growth was a direct result of the sputtering process. Analyses of the SAXD, First, and Second-order data showed that the samples were layered with individual layer spacings and bilayer repeat distances approximately equal to those expected from the sputtering conditions. The second-order spectra were also used to show that the rms deviations of the Nb and CuX layer thicknesses were less than about 0.3 nm for layer thicknesses greater than 2.0 nm.

3.2.3 Off-axis Scans

While a great deal of information was gained from the reflection scans described above, they provided no information about in-plane ordering between crystallites or about changes in atomic spacing within the layer planes. In multilayered materials, in-plane strain may be induced in the crystallites due to the occurrence of epitaxial growth at the metal-metal interface. Epitaxial growth occurs when material B attempts to grow in atomic registry with the existing atomic order of material A. This registry typically requires one or both of the crystal lattices to strain to improve the registry. Hence, these strains will lead to the most significant changes in the A and B lattice constants for spacings parallel to the interface.

The most straight-forward means of measuring these in-plane parameters is to rotate the sample by 90° and then perform a normal θ-2θ scan. Figure 3.10 shows such a scan taken on a 500 nm thick Nb film deposited on a 120 μm thick glass substrate.

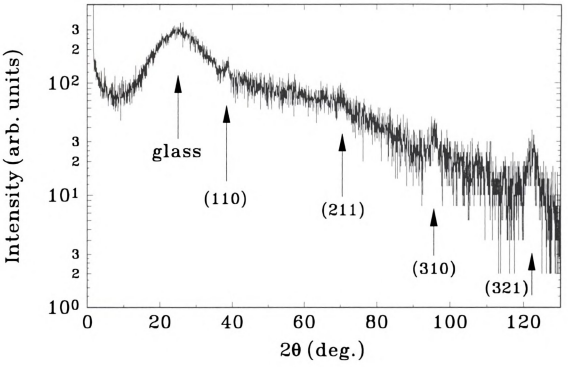

Figure 3.10: Transmission scan for a 500 nm thick Nb film.

The measured intensities were very low because the diffracted beam passed through the substrate. Glass substrates were used in these experiments because, for a thickness of 120 μm, a transmission of about 10% of the incident x-ray intensity was expected. Although diffraction peaks were observed, the peaks were anomalously broadened. In addition, some of the peaks in bulk films were shifted from their expected positions. These effects were attributed to inelastic scattering of the diffracted beam within the glass substrate. Attempts to remove the sample from the substrate resulted in samples that crinkled or rolled up into tiny tubes and were nearly impossible to flatten and measure. For these reasons, transmission experiments were abandoned.

A more subtle means of determining in-plane structure is to examine x-ray lines that contain information about both the in-plane and out-of-plane lattice spacings. By examining several such peak positions, the in-plane lattice spacing can be extracted. For instance, in the 2-D square lattice shown in Figure 3.11, the (01) planes are aligned parallel to the substrate. Therefore a normal reflection scan will measure only a_x. By rotating the entire sample by 45° the (11) planes are brought into the proper alignment for a diffraction scan. This scan then measures d_2 given by

$$\frac{1}{d_2^2} = \frac{1}{a_x^2} + \frac{1}{a_y^2} \tag{3.7}$$

where a_y is the in-plane lattice spacing. Hence, by combining the results of the two measurements, both lattice spacings can be determined.

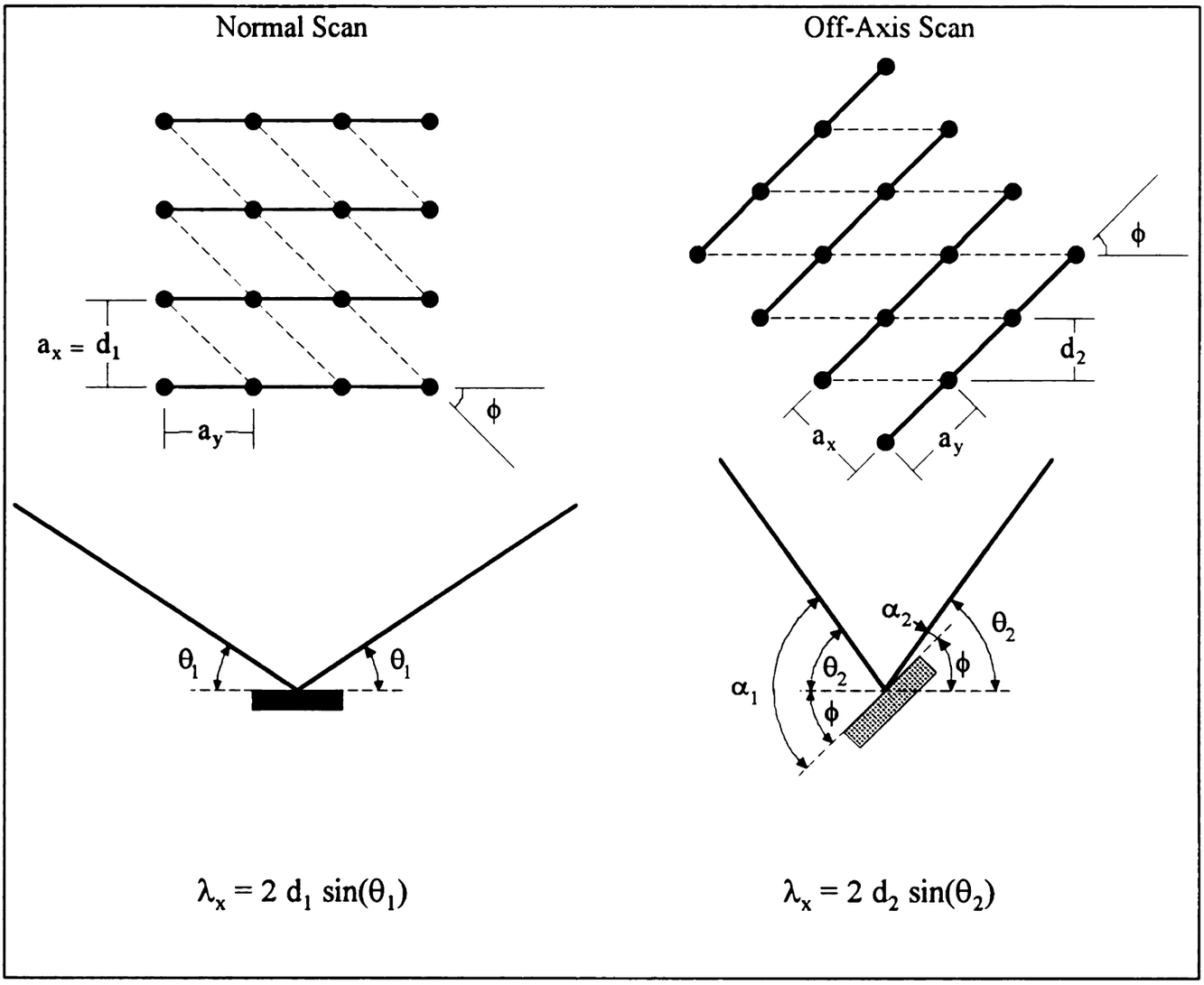

Figure 3.11: Off-axis scattering geometry.

The off-set angles ϕ are related to the geometry of the crystal structure and, for a cubic lattice, are calculable using the equation[36]

$$\phi = \frac{h_1h_2 + k_1k_2 + l_1l_2}{\sqrt{\left(h_1^2 + k_1^2 + l_1^2\right)\left(h_2^2 + k_2^2 + l_2^2\right)}} \qquad (3.8)$$

where $(h_1k_1l_1)$ and $(h_2k_2l_2)$ are the Miller indices for the two sets of planes involved (i.e. (01) and (11) for the case in Figure 11) and ϕ is the angle between the planes. $(h_1k_1l_1)$ is the plane from which the off set angles are measured, for Nb and CuX these were the (110) and (111) planes, respectively. ϕ is sensitive to the absolute order $h_2k_2l_2$, therefore, several values of ϕ can be calculated for each family of $h_2k_2l_2$ indices. For instance, for a bcc crystal, the angle between the (110) and (211) planes is 30°, while the angle between the (110) and (112) planes is 54.7°. All possible ϕ for the $(h_2k_2l_2)$ families up to Nb (440) and CuX (620) are listed in Table 3.1.

Diffraction from most of these planes still resulted in diffracted beams which passed through the substrate. For a small subset of these lines the diffracted beam was observed above the substrate when $\phi < \theta$. These lines are listed in Table 3.2. Off-axis diffraction was been observed for all these lines using Nb and CuX films and Nb/CuX multilayers. From an analysis of these peak positions and the peak positions observed at $\phi = 0$, the in-plane lattice spacing was determined.

Figure 3.12 shows the off axis (311) peaks observed for a CuMn(13%) film and a 3.0 nm thick CuMn(13%) layer. Within the accuracy of the data, there was no change in the in-plane atomic spacing for CuX thicknesses down to 3.0 nm. In addition, analyses of the off-angle CuX peak widths showed that the CuX crystallites had the same dimension within and across the layer both for bulk CuX films and for thin CuX layers.

Table 3.1: Off-axis angles, planer spacings, and diffraction angles for bcc Nb and fcc Cu.

	Line	Off set angles, ϕ (degrees)						d (nm)	2θ (deg.)	# of ϕ's
Nb	110	0	60	90				0.237	37.9	3
(110)	200	45	90					0.1675	54.8	2
	211	30	54.7	73.2	90			0.137	68.4	4
	220	0	60	90				0.118	81.5	3
	310	26.6	47.9	63.4	77.1			0.106	93.2	4
	222	35.3	90					0.0970	105.2	2
	321	19.1	40.9	55.5	67.8	79.1		0.0895	118.8	5
	400	45	90					0.0838	133.7	2
	330	0	60	90				0.0790	154.5	5
	411	33.6	60	70.5	90					
	420	18.4	50.8	71.6				0.0749		3
	332	25.2	41.1	81.3	90			0.0714		4
	422	30	54.7	73.2	90			0.0684		4
	431	13.9	46.1	56.3	65.4	73.9	82.0	0.0657		7
	510	33.7	46.1	56.3						
	520	25.4	39.2	58.9	67.2			0.0612		4
	440	0	60	90				0.0592		3
Cu	111	0	70.5					0.2090	43.3	2
(111)	200	54.7						0.1810	50.4	1
	220	35.3	90					0.1280	74.0	2
	311	29.5	58.5	80.3				0.1090	90.0	3
	222	0	70.5					0.1045	95.0	2
	400	54.7						0.0905	116.7	1
	331	22.0	48.5	82.4				0.0830	136.3	3
	420	39.2	75.0					0.0809	144.	2
	422	19.5	61.9	90				0.0739		3
	511	38.9	56.2	70.5				0.0697		4
	333	0	70.5							
	440	35.3	90					0.0640		2
	531	28.6	46.9	73.0	84.4			0.0612		4
	600	54.7						0.0603		3
	442	15.8	54.7	78.9						
	620	43.1	68.6					0.0572		2

Table 3.2: Off-axis lines observable using Cu K_α radiation.

	Line	ϕ (deg.)	2θ (deg.)
Nb	321	19.1	119
(110)	310	26.6	93.2
	211	30.0	68.4
	222	35.3	105
	312	40.9	119
	213	55.5	119
Cu	331	22.0	136.
(111)	311	29.5	90
	220	35.3	74
	$33\bar{1}$	48.5	136
	400	54.7	117

Nb proved to be more interesting. As ϕ was increased, the diffraction peaks broadened, an effect which was related to a decrease in the effective crystallite size. This implied that in bulk sputtered Nb, the crystallites were not isotropic, rather they were rod-like with length ~ 25 nm and diameter ~ 6.0 nm. In addition, bulk Nb was expected to be cubic with $a_x = a_y = a_z$. However, analyses of the bulk Nb (321), (312) and (123) peaks, shown in Figure 3.13, showed that the peak shifted to a larger angle (and smaller planer spacing) with increasing ϕ. Table 3.3 lists the planar spacings determined from these peaks. When all 6 lines listed in the table are taken into account, the peak shift corresponds to a (1.1 ±0.2)% change in the in-plane lattice spacing in plane spacing a_z relative to the normal lattice spacing a_x. Although this effect appears real, it must be related to an instrumental artifact since there are no driving forces in a pure Nb film that might cause a change in a_z relative to a_x.

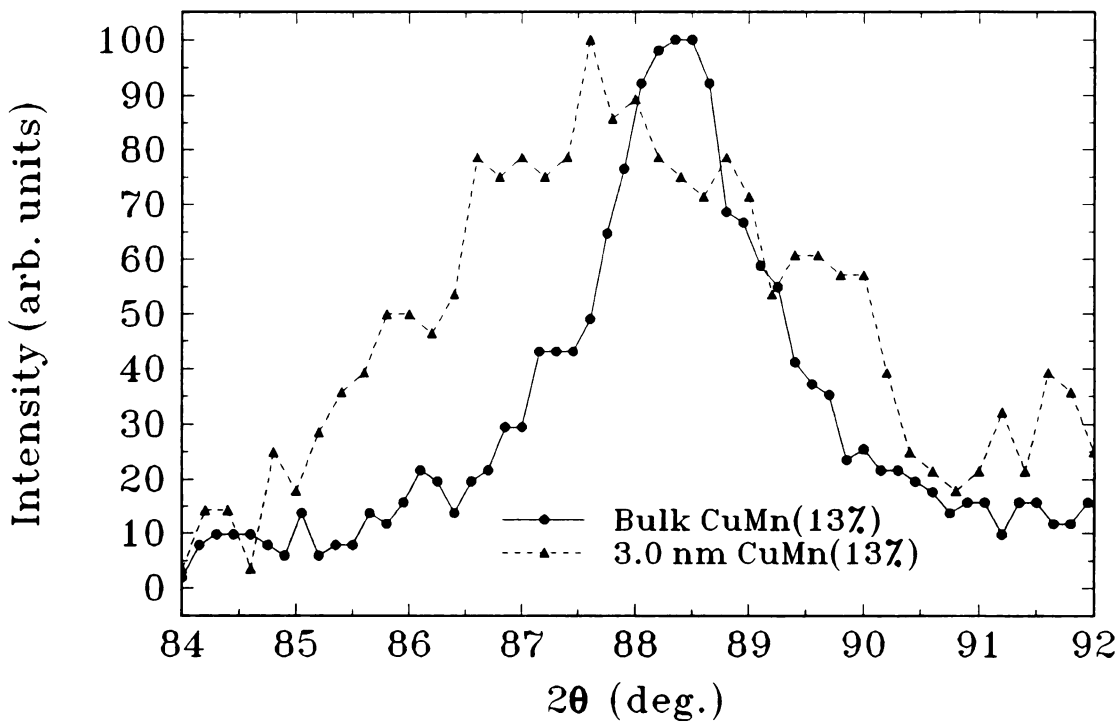

Figure 3.12: CuMn (311) peaks observed in a 500 nm thick CuMn(13%) film, and a Nb/CuMn(13%) 3.0 nm/3.0 nm multilayer.

The Nb (321) family of peaks for a Nb/CuMn(13%) 3.0 nm/3.0 nm multilayer displayed a similar shift in peak position with increasing ϕ. This shift resulted in an apparent change in the in-plane lattice spacing of (1.9 ± 1.0)% relative to a_x. Since this shift was significantly larger than the bulk Nb lattice shift there may be a real change in the in-plane Nb lattice spacing in these thin Nb layers. Additional studies need to be performed to definitively test if the Nb lattice is really strained in thin Nb layers.

Table 3.3: Off-axis peak positions recorded for Nb crystallites.

		bulk Nb			3.0 nm Nb layer		
Line	ϕ (deg.)	2θ (deg.)	d (nm)	*S* (nm)	2θ (deg.)	d (nm)	*S* (nm)
110	0	38.1±0.1	0.2359	26.	--	--	--
220	0	--	--	--	82.2±1.5	0.1172	--
310	26.6	94.4±0.3	0.1050	9.9	94.8±1.2	0.1047	3.3
222	35.3	107.2±0.4	0.0957	7.5	110.0±1.5	0.0942	2.8
321	19	120.0±0.3	0.0890	7.9	120.9±1.5	0.0886	3.4
312	41	121.0±0.4	0.0885	6.3	122.3±1.5	0.0880	3.4
123	55.5	121.6±0.6	0.0883	6.0	123.6±1.5	0.0874	3.5

3.2.4 Rocking Curves

Rocking curves were used to determine the approximate angular distribution of crystallite orientations normal to the metal film plane. For the rocking curves, the detector angle 2θ was held fixed, thereby fixing the planar spacing examined, and the sample angle α was swept through the diffraction peak at $\alpha = \theta$. For a sample composed of randomly oriented crystallites, the rocking curve is expected to show little change in intensity as α is changed. If, however, the crystallites are preferentially ordered along the direction normal to the layers, the rocking curve is expected to show a peak at $\alpha = \theta$ whose width is proportional to the distribution of normals to the crystallites.

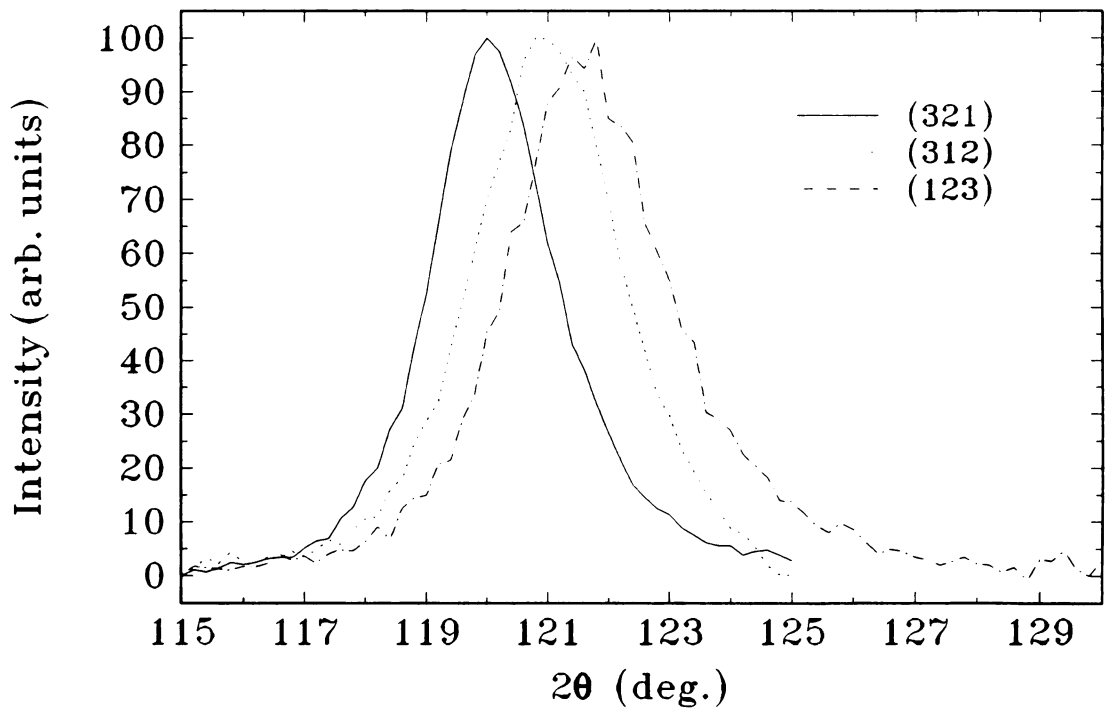

Figure 3.13: Off-axis peaks observed in a 500 nm thick Nb film: (a) (321) peak, (b) (312) peak and (c) (123) peak.

Figure 3.14, shows a rocking curve for a 500 nm Nb film. On the basis of the width of this peak, the (110) planes were interpreted as being parallel to the substrate to within ~ 5°. Similar data were recorded for thin Nb and Cu layers. From these data one can infer that in all the multilayers of this study, the Nb (110) and CuX (111) planes lay parallel to the substrate to within ~5°.

3.3 XAFS Measurements

X-ray absorption fine structure (XAFS) analysis was used to check the lattice parameters and crystal structure in very thin CuX layers (< 4.0 nm thick). On the high energy side of the x-ray absorption edge of an element, resonances occur between the excited core electron and electrons bound to neighboring atoms. These resonances lead to oscillations of the absorption spectrum of the element whose period is proportional to the fourier transform of the radial electron distribution near the absorbing atom. One of the main drawbacks to XAFS measurements is the sensitivity of the extracted radial distribution function to systematic effects. To get meaningful measurements of lattice spacings and crystal structures using XAFS, a standard sample must always be run whose XAFS spectra are very similar to that of the measured sample. This sample is then used as an internal standard and lattice and crystal structure changes are then determined relative to the standard. The XAFS analyses software package used for these comparisons was developed at the University of Washington.[37]

The XAFS data were taken using beam line X23b at the National Synchrotron Light Source at Brookhaven National Laboratory. A monochromatic x-ray beam was sent through an Ar filled proportional counter to measure the incident beam intensity. The beam then passed through the sample, and into a second proportional counter. The

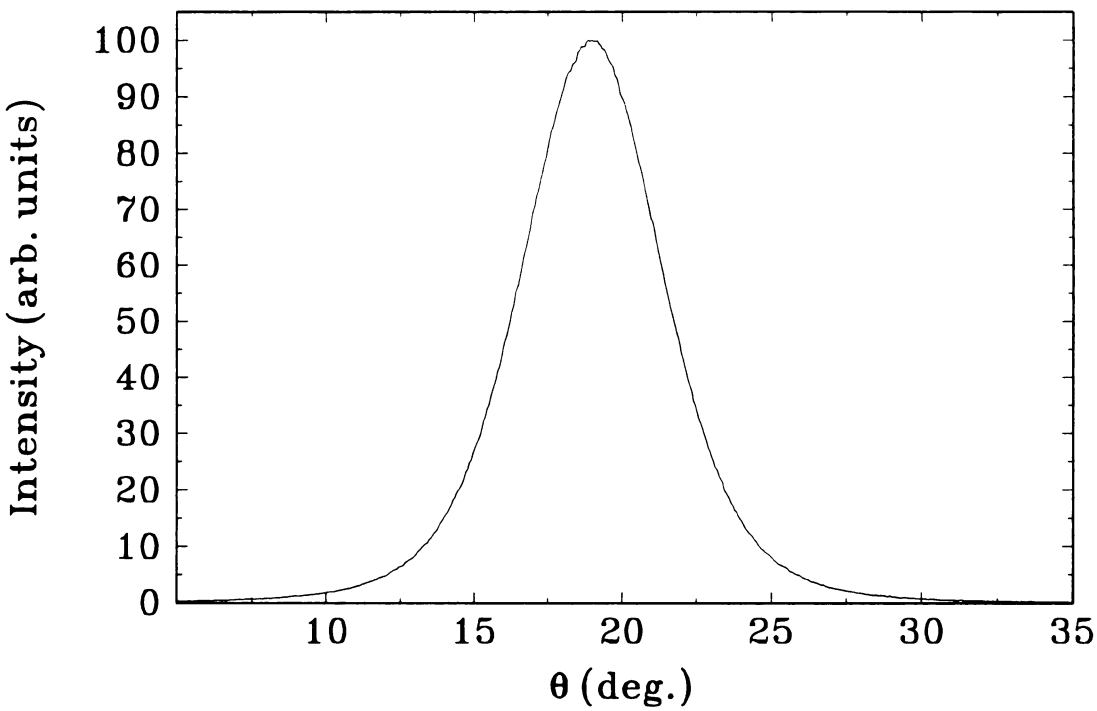

Figure 3.14: Rocking curve for the (110) line of a bulk Nb film.

absorption was defined as the ratio of the intensities measured in the two counters. The recorded absorption spectrum for the Cu edge in a Nb/CuMn(1%) 5.2 nm/4.6 nm sample is shown in Figure 3.15.

The linear background was removed from these data and the intensity of the oscillations was normalized to the height of the absorption edge. In addition, the horizontal scale was converted from energy to *k*-space using $k = \sqrt{26.3(E - E_o)}$, where *k* is in nm^{-1} and E is in eV. E_o was always defined as the energy at the midpoint of the absorption step. The extracted oscillations for the above Nb/CuMn(1%) sample, now called a Chi plot, are shown in Figure 3.16.

These *k*-space data were then fourier transformed into real space to create the radial distribution function. The end points in *k*-space for the back transform were picked to include as large a span of *k*-values as possible, but still be usable for all the data sets measured. The resulting picks for the maximum and minimum *k*'s are shown in Figure 3.16. The resulting radial distribution function for the Nb/CuMn(1%) sample is shown in Figure 3.17.

The position and intensity of the peaks in Figure 3.17 are related to the number of nearest neighbors and the distance to each shell of neighbors. Here one shell, at 0.226 nm, and three weaker shells at 0.35 nm, 0.42 nm, and 0.48 nm were observed, the other small peaks appearing in Figure 6.17 were attributed to artifacts of the fourier transform because they were not observed in all samples. For the CuMn(1%) fcc lattice there should be 12 nearest neighbors appearing at a distance of 0.2556 nm. The observed peaks in the r-space plots did not coincide with the expected distance because of systematic changes related to the analyses and choice of k-space cut points. For this reason, accurate measurements of atomic spacing and numbers of neighbors were made by comparing the data from the unknown sample with data taken on a standard 2 μm thick pure Cu foil. By analyzing the standard and sample using the same apparatus and choice of k-space cut points, the systematic effects altered both data sets in the same manner. Therefore, by

comparing the standard and sample radial distribution functions, the true lattice spacings and nearest neighbor numbers were determined.

To compare the Cu foil and Nb/CuMn(1%) data, the data for the first atomic shell (near R = 0.226 nm) were back transformed into k-space. An analytic routine was then used to fit the standard data set to the multilayer data. To systematize these back transformed data, the same R-space end-points (0.182 nm and 0.255 nm) were used both for the Nb/CuMn sample data and the standard Cu film data. Table 3.4 shows the resulting values for the number of nearest neighbors N, distance to the nearest shell of atoms, R_{nn}, and a parameter related to the thermal broadening of the XAFS oscillations σ^2. The table shows that a slight change of about 0.02 nm in the CuX lattice may occur in very thin (2.0 nm) CuX layers. This was consistent with the previously discussed x-ray studies on Nb/Cu 2.0 nm/2.0 nm multilayers which showed that the CuX lattice spacing was within ±0.070 nm of its bulk value. Therefore, XAFS analyses provided a significantly more accurate measure of the CuX lattice constant than was possible using x-ray diffraction.

The observed trend of decreasing N with decreased CuX layer thickness is not understood but is consistent with Cu XAFS data taken on Co/Cu multilayers by Dr. Carl Foiles of Michigan State University.[38]

XAFS measurements were attempted on thin Nb layers. The observed signal to noise ratio, however, was sufficiently low that the data could not be analyzed.

Table 3.4: XAFS derived parameters for Nb/CuMn(1%) samples.

Sample	N	R_{nn} (nm)	σ^2
Cu standard	12	0.2556	0
7.6 nm CuMn(1%)	10.6±2	0.2550±0.0020	0.0003
4.6 nm CuMn(1%)	9.9±2	0.2554±0.0020	0.0007
2.1 nm CuMn(1%)	8.2±2	0.2534±0.0020	0.0012

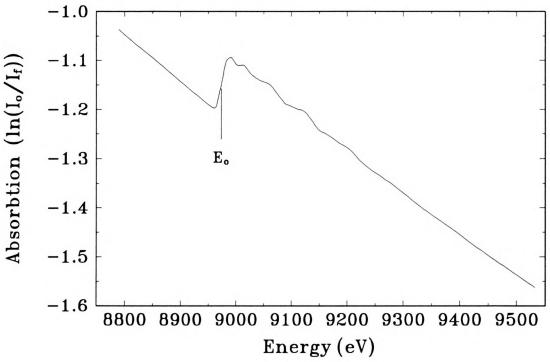

Figure 3.15: Raw Cu absorption data for a Nb/CuMn(1%) 5.2 nm/4.6 nm multilayer.

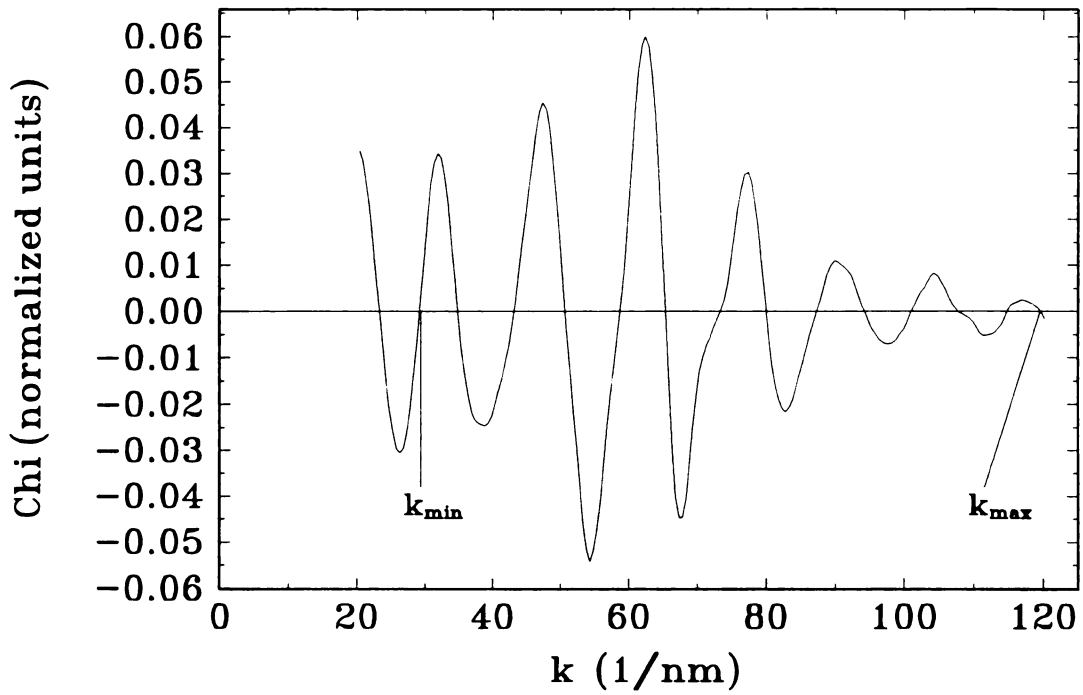

Figure 3.16: Chi plots for a Nb/CuMn(1%) 5.2 nm/4.6 nm multilayer.

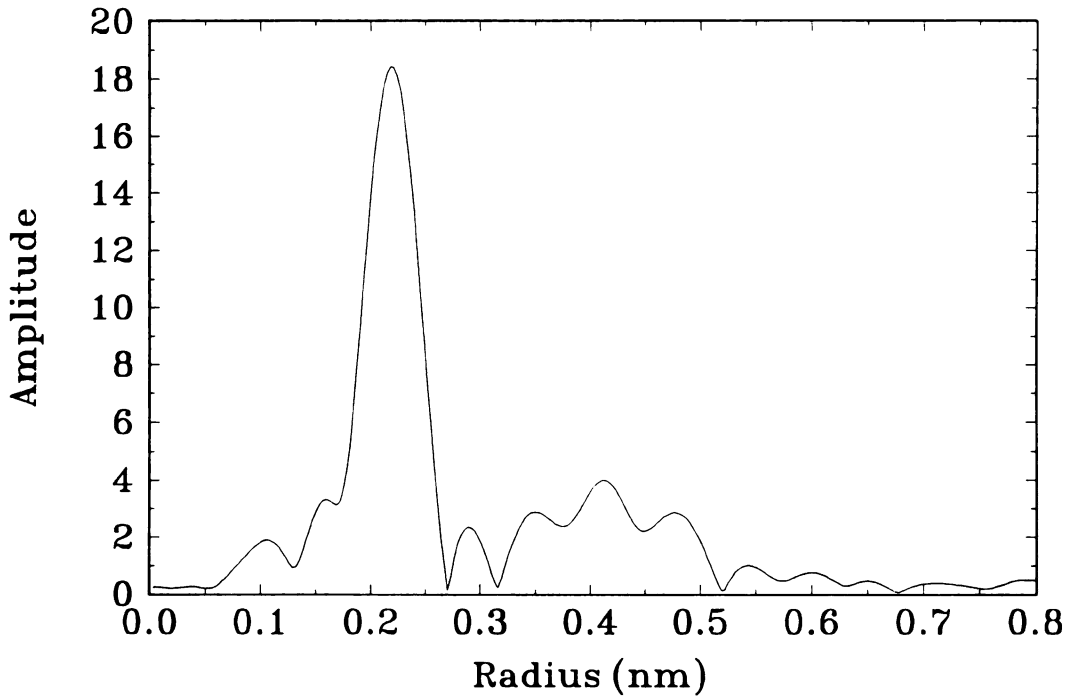

Figure 3.17: Radial mass distribution function surrounding Cu in a Nb/CuMn(1%) 5.2 nm/4.6 nm multilayer.

3.4 Studies of Cross-Sectioned Samples

In principle, a thorough study of cross-sectioned multilayer films using electron diffraction and electron imaging can provide information on most of the structural parameters described above. The primary problem with this as a generally applied technique is the difficulty of preparing satisfactory cross-sections. David Howell of the Materials Science and Engineering Department of Michigan State University prepared the cross-sections used and took the electron micrographs and electron diffraction scans used in the following analysis.

The cross-sections were prepared by removing a multilayered sample from its substrate, embedding it in an epoxy block and then sectioning the sample and epoxy using an ultramicrotome. The resulting sections were typically 60-70 nm thick, just thin enough for good electron transmission. The primary preparation problem was the lack of adhesion of the multilayer film to the epoxy. Usually, the films detached from the epoxy as they were sectioned, thereby ruining the section. The above preparation difficulties limited the study to only one sample: Nb/CuMn(7%) 28.0 nm/4.0 nm with 25 bilayers.

Figures 3.18 and 3.19 show a dark field image and the corresponding electron diffraction pattern, respectively, for the Nb/CuMn(7%) 28.0 nm/4.0 nm sample. A dark field image highlights individual crystallites whose orientations are such that they diffract electrons into one of the spots on the electron diffraction pattern. These images provided better contrast between the Nb and CuMn layers than was obtained from normal transmission (bright field) images.

In the dark field image, (Figure 3.18), the Nb and CuMn layers appear continuous with no large scale fluctuations in their layer thicknesses. In addition, the Nb crystallites were observed to extend across the entire thickness of each Nb layer. This agrees with the previously discussed x-ray diffraction results. As the electrons pass through the section, they are inelastically scattered. This scattering broadens the sample features to

such an extent that good images of the CuMn layers or Nb-CuX interfaces were not achievable.

The electron diffraction pattern (Figure 3.19) showed a great deal of detail about the crystallite orientations within the Nb and CuX layers. The diffraction spots lie on concentric circles. These circles correspond to diffraction from the Nb and CuX planes listed in Table 3.1. The angular spread of the diffraction spots provided a measure of the angular spread in orientations of the Nb and CuMn crystallites. These spreads were found to be ~5°, in agreement with the rocking curve data. Note that for the (110) circle, spots appear at 0°, 60°, and 90° away from the line normal to the film. These positions concur with the expected off-set angles listed in Table 3.1. By carefully indexing these diffraction spots with the expected off-angle peak positions, an absolute identification was made of all the diffraction spots in this, and other, diffraction patterns. Most of the observed diffraction spots were indexed to scattering from Nb. The only clearly resolved CuMn spots observable in Figure 3.19 were the (200) spots occurring at ~55° from the Nb(110) growth direction.

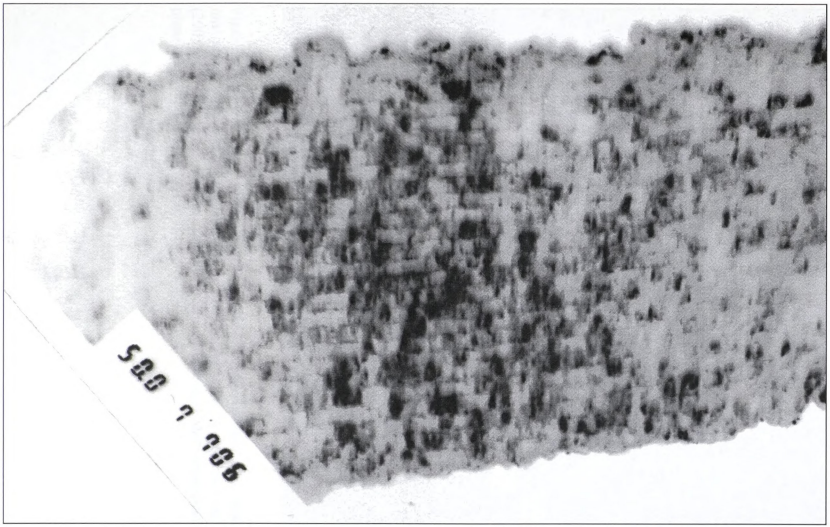

Figure 3.18: Dark field electron image of a cross-section of a Nb/CuMn(7%) 28 nm/4.0 nm multilayered sample.

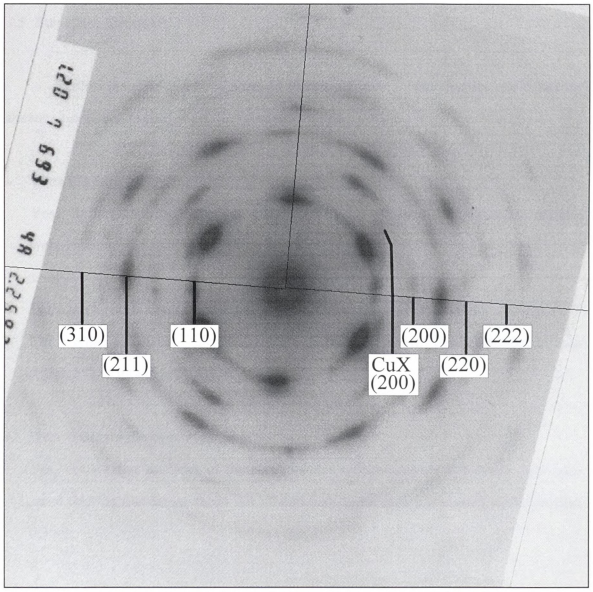

Figure 3.19: Electron diffraction pattern taken from a cross sectioned Nb/CuMn(7%) 28 nm/ 4.0 nm multilayered sample. Miller indices for the observed Nb planes and the CuX (200) plane are labeled. Thin lines denote the direction parallel and perpendicular to the plane of the Nb and CuX layers.

3.5 Structure Summary

Returning to the questions posed in the introduction to this chapter, the following answers have been found:

- Were the samples layered?

  Yes. Reflection x-ray diffraction and electron micrographs showed that the samples were layered.

- Were the layer thicknesses as expected from the sputtering conditions?

  Yes. Analyses of the reflection scans indicated that the bilayer separation Λ was within 5% of its expected value.

- Were the layer thicknesses uniform?

  Yes. Qualitative analyses of the second-order reflection x-ray diffraction data indicated that the rms deviations in the Nb and CuX layer thicknesses were no larger than 0.3 nm.

- Was the Nb-CuX interface sharp?

  Unresolved. The resolution of the electron micrographs was not high enough to study the interfaces. More studies need to be done to answer this question.

- What were the concentrations of desired and undesired impurities in the Nb and CuX layers?

  Analyses of EDX and magnetization data showed that the Ge concentration of CuGe was 4.9 at. % and the Mn concentrations of the primary CuMn layers used were 0.3

at. %, 1.0 at. % and 2.2 at. %. No other stray impurities were observed in either the Nb or CuX materials.

- Were the Nb and CuX layers crystalline?

  Yes. The x-ray diffraction, XAFS, and electron diffraction experiments all indicated that the Nb and CuX layers were crystalline for all layer thicknesses studied.

- Were there any changes in the Nb or CuX lattice spacings as the layer thicknesses were reduced?

  Perhaps. The XAFS data indicated that a slight (~1%) change may occur in the CuX lattice spacing for CuX thicknesses 2.0 nm thick, while the x-ray results concluded that the CuX lattice changes by no more than 3%. The Nb data indicated that the in-plane lattice spacing of Nb may decrease by ~1% for Nb layers 3.0 nm thick, but this change was very tentative.

- Were there strains in the Nb or CuX layers near the Nb-CuX interface?

  Perhaps. Such a strain would provide the driving force for the small shifts in lattice spacing described above. More studies need to be made, especially electron diffraction on very thin Nb and Cu layers, to be sure that these observed shifts were real.

- Were the Nb or CuX crystallites preferentially oriented?

  Yes. Analyses of the reflection x-ray diffraction and the electron diffraction patterns showed that the Nb (110) and (111) planes were parallel to the sample substrate to within approximately 5°.

Other than a decrease in the mean crystallite size, these studies have indicated that there were no changes in the Nb or CuX crystal structures for Nb and CuX layer thick-

nesses greater than about 4.0 nm. For thinner layers, there were some indications that both the Nb and CuX lattice were slightly strained, possibly due to ordering at the Nb-CuX interface. Further studies need to be performed to determine if the changes described above for thin Nb and CuX layers were real or simply systematic effects.

CHAPTER 4
EXPERIMENTAL PROCEDURES

All of the experimental results reported in this thesis were obtained using electrical resistivity and magnetization measurements. Resistivity was used to determine the superconducting transition temperature T_c, and the superconducting upper critical field $H_{c2}(T)$, while magnetization was used to determine the spin-glass freezing temperature T_f. Both these experiments were carried out utilizing a Quantum Design Magnetic Property Measurement System (MPMS). The magnetization experiments used the system's SQUID magnetometer circuits, while the resistivity measurements used the MPMS system as a precision cryostat and for computer control of a Keithley K181 nanovoltmeter and a K224 current source.

All samples used in these studies were sputtered through a patterned mask during fabrication to produce both a 5-probe resistivity sample and a separate magnetization sample on each substrate. Figure 5.1 shows the resulting sample pattern. The right side was used in a four probe resistance geometry and was used for measurements of T_c and $H_{c2}(T)$ with the magnetic field parallel to the sample surface $H_{c2\parallel}(T)$. The left side was used for magnetization measurements and for $H_{c2}(T)$ measurements with the magnetic field applied perpendicular to the sample surface $H_{c2\perp}(T)$. The magnetization measurements used the entire left sample. However, the $H_{c2\perp}(T)$ measurements were made using only a small, 3 mm x 4 mm, piece, the maximum size which would fit into the MPMS sample holder.

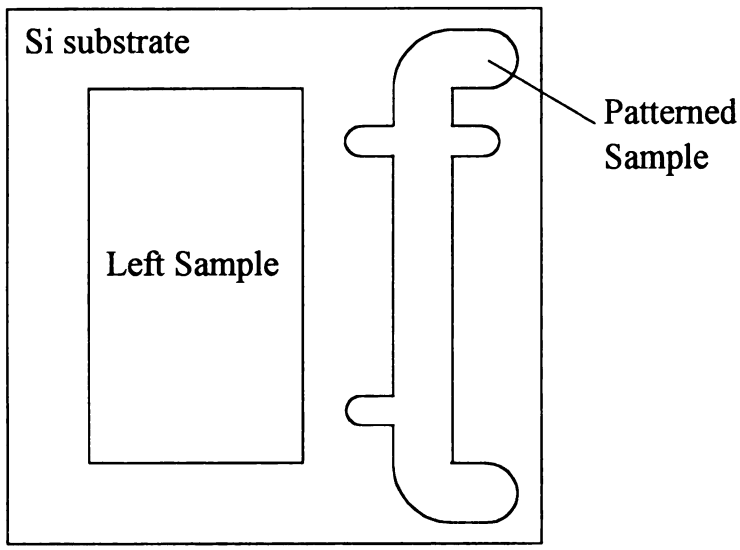

Figure 4.1: Diagram of the sample pattern.

4.1 Magnetic Measurements

Magnetization measurements were used to determine the spin-glass freezing temperature T_f. For each sample, the left side (Figure 4.1) was cleaved from the remainder of the substrate, then all uncoated regions of Si were also cleaved away from the sample. This was done to limit the mass of Si that was measured along with the sample. The remaining sample was then cleaved into three 3 mm x 5 mm pieces which were stacked together, sealed in a small close-fitting plastic bag and mounted on the MPMS sample holder with the long axis of the sample perpendicular to the long axis of the system.

In the MPMS system, M(T) was measured using a difference technique. The sample is raised vertically through a set of three pickup coils attached to the MPMS SQUID circuit. The resulting SQUID response was then used to calculate M. The response of this system was sensitive to the length of the sample along the axis of the pickup coils. By positioning the sample as described above, a slight improvement in signal to noise was found compared to orienting the sample with its plane along the coil axis.

In a spin-glass, T_f is typically defined by the temperature of a cusp in M(T), as shown in Figure 4.2. To obtain the zero-field-cooled (zfc) data, the sample was cooled from well above T_f to well below T_f in zero applied magnetic field. A measuring field of 50 or 100 gauss was then applied to the sample and the magnetization was measured as the temperature was increased. Here, T_f was defined as the temperature at the maximum in M(T). For field-cooled (fc) data, the sample was cooled to below T_f with the measuring field (50 or 100 gauss) already on. Then M(T) was measured as the temperature was increased, similar to the zfc data. For the fc data, T_f was defined as the temperature at a kink in M(T), as shown in Figure 4.2. Typically the fc and zfc measurements of T_f agreed to within 0.3 K. This combined with the sample-to-sample variability, measurement-to-measurement reproducibility, and natural width of the peak at T_f limited the final systematic error in T_f to ± 0.5 K.

4.2 Resistivity Measurements

The current and voltage leads were attached to each sample using silver paint. The paint was applied and allowed to air dry for 30 minutes prior to use in the cryostat. For the T_c and $H_{c2\|}$ measurements, the current leads were attached to the ends of the sample, while the voltage leads were attached to the tabs along the right side of the sample. For the $H_{c2\perp}(T)$ sample chip, the two current leads were attached to two corners on one side of the sample while the voltage contacts were attached to the remaining corners.

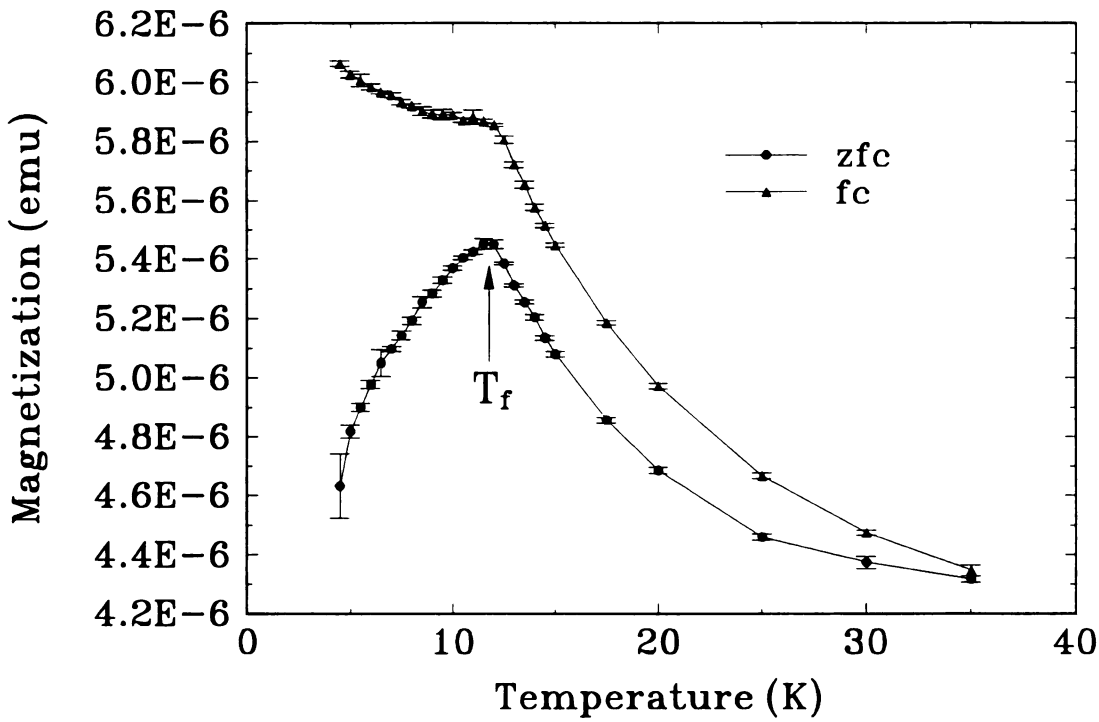

Figure 4.2: Zero-field-cooled (zfc) and field-cooled (fc) magnetization data for a 500 nm thick CuMn(1%) film.

The resistance measurements were performed by decreasing the temperature stepwise through the superconducting transition at a fixed external magnetic field. The standard temperature interval used, 0.02 K, was the smallest reliable increment produced by the MPMS system. Once the temperature was stabilized, the voltmeter was set to read zero for zero applied current, a positive current of 1.00 mA was applied and the voltage was measured 20 times. The current was then reversed and 20 additional data points taken. The absolute values of these voltages were averaged and divided by the current (1.0 mA) to yield the resistance R. The current was then turned off to limit sample heating and the temperature changed to the next value. The resultant R's were typically in the range 10^{-3} to 1.0 Ω, depending on the layer thicknesses used, and the noise level (i.e. the voltage measured for $T << T_c$) was ~5 x 10^{-6} Ω for all samples. The 1 mA measuring current corresponded to a current density of 40 to 120 A/cm^2, well below the critical current of Nb (~10^6 A/cm^2).[39]

Measuring the (H, T) phase diagram for a single sample is a very time consuming process, typically taking 12 to 24 hours per sample. To minimize this time and use the MPMS more efficiently, the following procedures were derived. During each temperature series at constant field H_o, the computer monitored the decreasing resistance until it dropped to less than 10^{-5} Ω, at which point the run was stopped. The computer then calculated the transition temperature $T_c(H_o)$ and began a new run at a field $H_o + \Delta H$ and a starting temperature $T_c(H_o)$ + 0.06 K. Typically, small field increments 250 G < ΔH < 500 G were used when H_o was less than 2000 G while larger increments 1 kG < ΔH < 2 kG were used at larger fields.

The patterning process used to fabricate the 5-probe samples lead to rather broad sample edges (sometimes up to 35 % of the total sample width). To check that these edges were not affecting the T_c and $H_{c2\|}(T)$ measurements, data was compared with T_c and $H_{c2\|}(T)$ measured in portions of the unpatterned left side of the sample. The unpatterned samples were prepared by cleaving all the sputtered edges away from the left-hand

sample and then attaching leads as was done for the $H_{c2\perp}(T)$ samples. No significant or systematic change in either T_c or $H_{c2\parallel}(T)$ was observed when the data for these two samples were compared.

Based on the sample-to-sample and measurement-to-measurement variability of T_c the total error in T_c was approximately $\pm$ 0.10 K. For the $H_{c2}(T)$ experiments, most of the sample-to-sample reproducibility error was related to errors in T_c. When $H_{c2}(T)$ data were normalized to T_c, the variability in $H_{c2}(T)$ data sets was found to be of order $\pm$ 2 % of $H_{c2}(T)$. In the temperature regime from 4.10 K to 4.40 K however, the inherent error in temperature was greatly increased due to temperature instability of the MPMS system in this regime over the long times needed to measure $H_{c2}(T)$. Hence, most $H_{c2}(T)$ data sets display small glitches in this temperature regime. For samples in which T_c was in this region the increased error became rather serious, therefore, several $H_{c2}(T)$ data sets were averaged to create a single $H_{c2}(T)$ set.

CHAPTER 5
THE SUPERCONDUCTING TRANSITION TEMPERATURE

In S/N multilayers, the superconducting transition temperature will be affected both by the extent of proximity effect induced superconductivity in N and by the influence of reduced S layer thickness on the superconducting properties of S. In this chapter, measurements and models for the behavior of the zero field superconducting transition temperature T_c of an S/N multilayer will be used to study these phenomena. First, the experimental results will be discussed along with a qualitative model for some of the results. Then, two theoretical models for proximity effect superconductivity will be presented. Finally, the results of these models will be compared to the experimental data.

5.1 T_c Experiments

5.1.1 The Dependence of T_c on the N Layer Thickness

In this section studies of how the thickness and impurities in the N layer (at fixed S layer thickness) modify T_c through the scattering of coherent electrons induced in N by the proximity effect will be examined. For small d_n, the superconducting pair density in N is large, few pairs are destroyed in N, leading to strong coupling between S layers and $T_c \cong T_c^b$ the bulk superconducting transition temperature of S, as shown in Figure 5.1. As d_n increases, T_c decreases monotonically due to the breakup of superconducting pairs in the N layer and a decrease in proximity effect coupling between S layers. Eventually, for very large d_n, all superconducting pairs entering N are destroyed before reaching the next S layer, hence the S layers are decoupled from one another. In this large d_n regime, T_c reaches a minimum value T_c^m determined by the maximum loss of superconducting pairs into N. Since there is no longer any superconductive coupling, T_c^m should be the same for

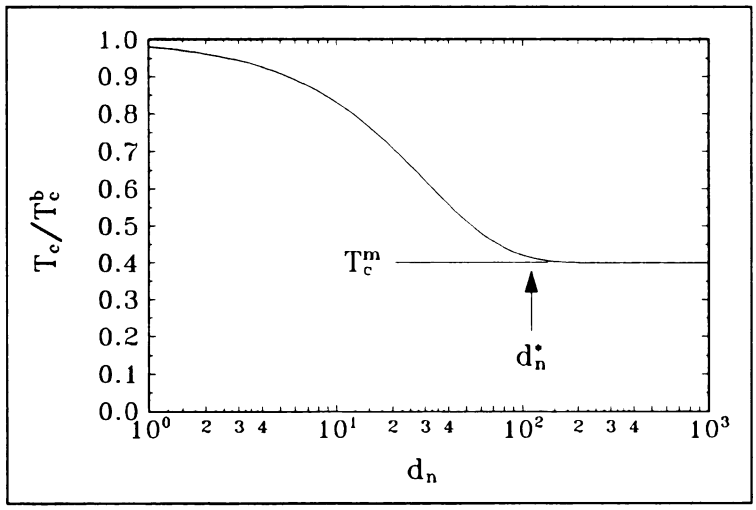

Figure 5.1: Qualitative dependence of T_c on d_n for fixed d_s.

multilayers, where coupling can occur, and for bilayer films, where coupling cannot occur. Therefore, d_{nc}^*, the N layer thickness beyond which $T_c = T_c^m$, is representative of the penetration depth of induced superconductivity into the N layer.

Figure 5.2 presents experimental data for the dependence of T_c on d_n for multilayer series having fixed Nb thickness (28.0 nm) and Cu, CuGe(5%), and CuMn(y) interlayers. All series exhibited a decrease of T_c with increasing d_n, consistent with the penetration of superconductivity into N. For thin non-magnetic layers, T_c was independent of whether Cu or CuGe(5%) layers are used, while for thick non-magnetic layers (d_n > 20 nm), T_c was larger for Nb/CuGe(5%) samples than for Nb/Cu. Associated with this enhancement of T_c there was also a reduction in d_{nc}^*. These differences between Cu and CuGe for thick N layers also held for other S layer thickness, as shown in Figure 5.3.

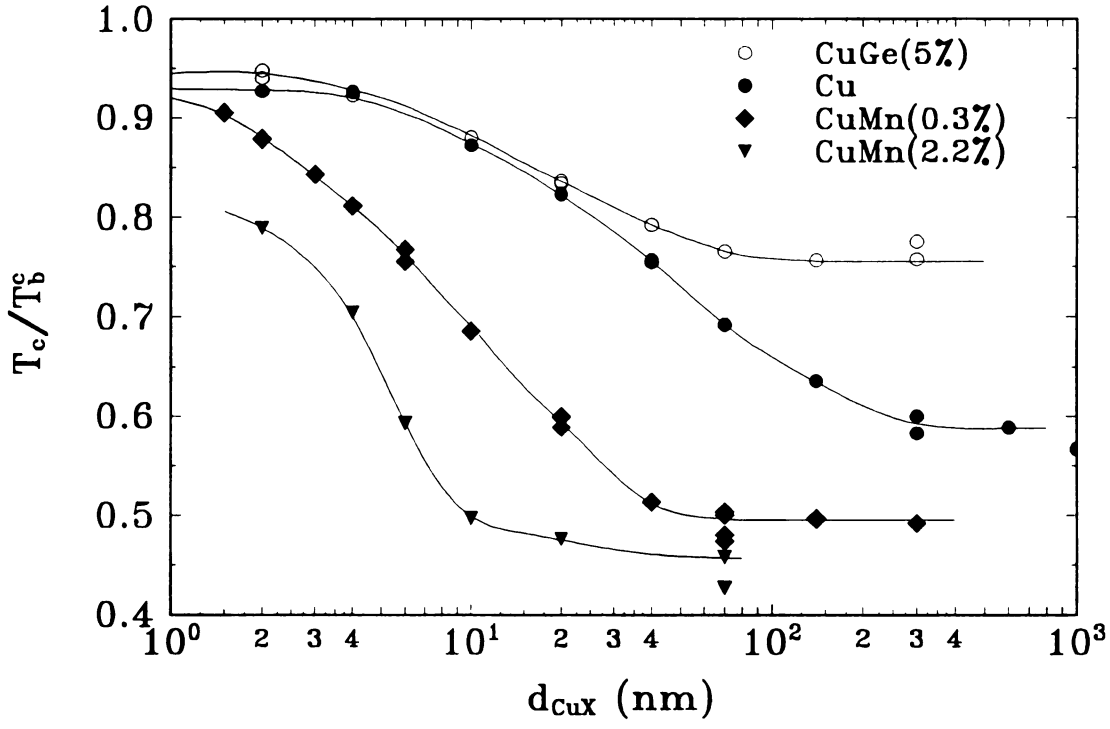

Figure 5.2: The dependence of T_c on d_n for d_s = 28.0 nm and various CuX materials.

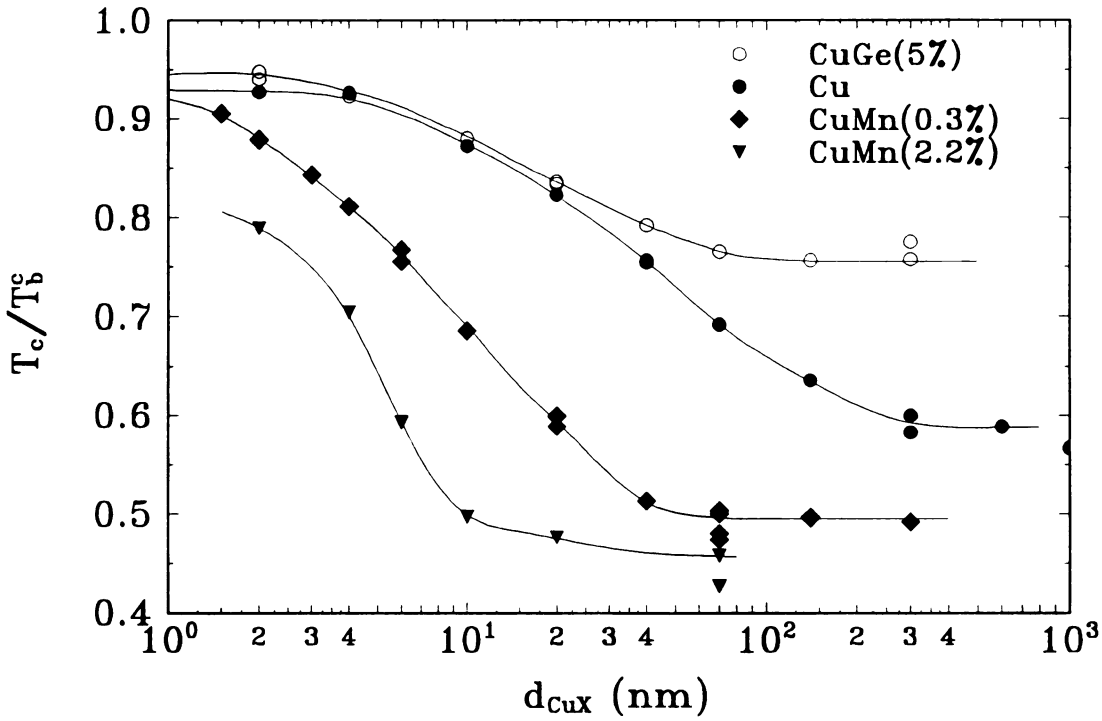

Figure 5.2: The dependence of T_c on d_n for d_s = 28.0 nm and various CuX materials.

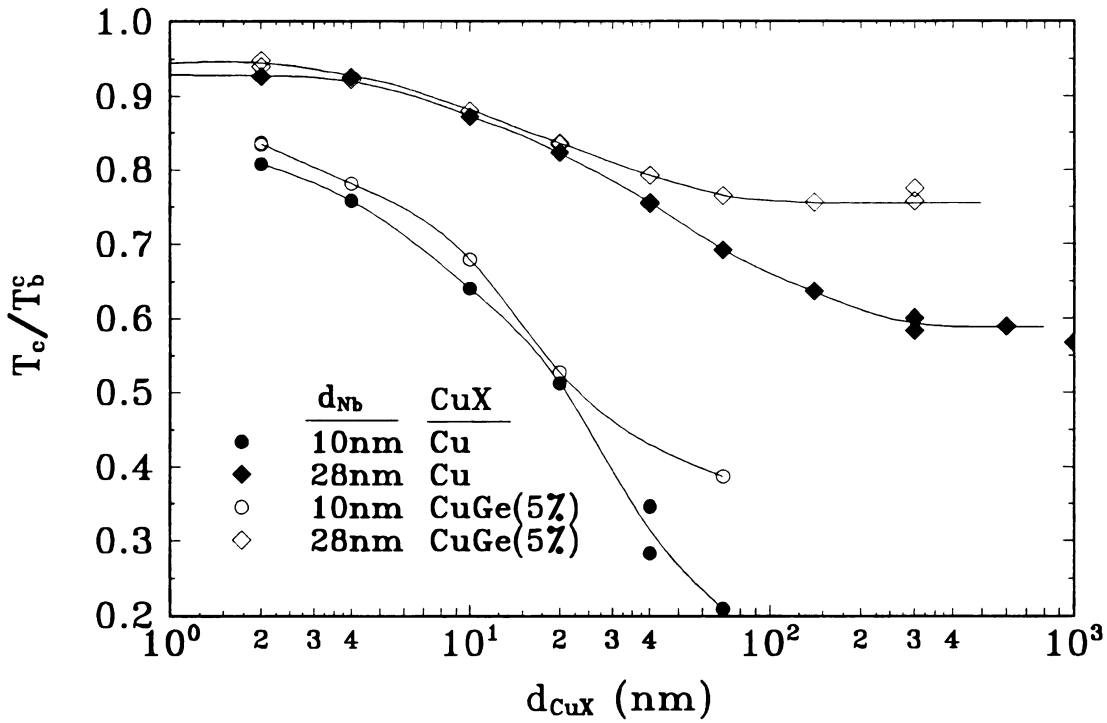

Figure 5.3: The dependence of T_c on d_n in Nb/Cu and Nb/CuGe(5%) multilayers for Nb layer thicknesses of 10 nm and 28 nm.

At small d_n and d_s, T_c did not tend toward T_c^b, rather, it saturated to a value well below T_c^b. This may be an effect of the depression of the superconducting properties of S observed in isolated Nb films.[15] Such a depression of T_c^b in Nb will be discussed more fully below.

Series having magnetic CuMn(y) interlayers displayed the same general behavior. For magnetic interlayers, however, T_c and d_{nc}^* decreased with increasing impurity concentration while T_c^m remained fairly constant for $y \geq 0.3$ at. %. There was a magnetic effect on T_c^m, however, since it decreased significantly when the N layer was changed from Cu to CuMn(0.3%).

These results can be qualitatively understood using a scattering model for the behavior of electrons in the N layer. In a lowest order approximation, electrons traveling in N can be treated as traveling by way of a random walk. Electrons entering N from S are phase coherent with the superconducting layer from which they originate. As phase coherent electrons traverse the N layer one of three things can occur:

- Transmission: The electron can remain phase coherent and traverse the entire thickness of the N layer to enter the next S layer thereby coupling the phases of the two S layers.
- Spin-Scattering: The electron can spin-scatter from an impurity in N and lose its phase memory. This removes the electron from its phase coherent state.
- Reflection: The electron can scatter back into the S layer from which it originated. This increases the superconducting pair density in S as ℓ_n decreases.

These three processes are sketched in Figure 5.4.

For thin normal metal layers, the electron mean free path ℓ_n is greater than d_n, so little scattering occurs in N and the transmission coefficient T is approximately unity. Hence, in the thin N limit, T_c should be independent of the N material used. Qualitatively,

this is the behavior observed for very thin Cu, CuGe(5%), and CuMn(0.3%) N layer materials.

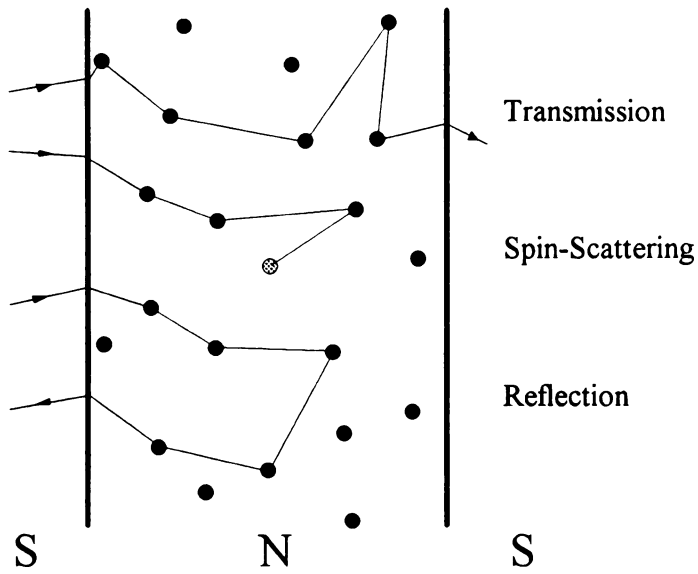

Figure 5.4: The three dominant processes for a phase coherent electron entering a normal metal layer.

As d_n is increased for fixed ℓ_n, spin-scattering and reflection begin to be important. If a small amount of Mn is added to Cu, the spin-scattering probability increases and the probability for a superconducting pair to be destroyed in N also increases. This should result in a decrease in the superconducting pair density in both S and N, and hence a decrease in T_c. This was the behavior observed as Mn ions were added to Cu. This simple picture, however, does not explain why T_c^m is independent of the Mn concentration at very large CuMn layer thicknesses. This phenomenon will be discussed in the theory section.

If the spin-scattering probability is low, as occurs for non-magnetic N materials, then reflection should dominate. This leads to an enhancement in the superconducting pair density in S, and hence a higher T_c as ℓ_n is decreased. This increase was observed for thick N layers in which 5 at. % Ge was added to the Cu.

5.1.2 The Dependence of T_c on the S Layer Thickness

An analysis of how T_c depends on d_s at fixed d_n provides information on how the superconducting properties of S are altered by the influence of the N layer. In general, as d_s is decreased, for fixed d_n, T_c should decrease toward zero. In bulk Nb, T_c is strongly related to the electron mean free path ℓ_s. As ℓ_s decreases, a peak in Nb's density of states near the Fermi energy broadens resulting in a decrease in Nb's density of states at the Fermi energy N(0), and hence a decrease in T_c. In thin films, ℓ_s is often proportional to the mean crystallite size, which, as was discussed in the structure chapter, is proportional to the sample layer thickness d_s. T_c should, therefore, decrease with decreasing d_s. For Nb, Cooper has theoretically modeled this process and found that T_c is roughly given by:[40]

$$\frac{T_c^b - T_c^f}{T_c^b} \cong \left(\frac{d_o^f}{d_s}\right)^1 \qquad (5.1)$$

where T_c^f is T_c in the Nb film, and d_o^f is a scale factor for the layer thickness. The proximity effect may alter this relationship depending on how the superconducting pairs are scattered in N and on how the S layers are coupled.

Figure 5.5 shows the dependence of T_c as a function of d_s, $T_c(d_s)$, for two strongly coupled (d_n = 2.0 nm of CuGe(5%) and CuMn(0.3%)) and two weakly coupled (d_n = 300 nm of CuGe(5%) and 70 nm of CuMn(0.3%)) multilayered series. T_c was observed to decrease with increased Mn concentration and increased N layer thickness for all d_s. On the basis of this figure, however, it was difficult to determine if there were any quantitative changes in the behavior of $T_c(d_s)$ as either d_n or the composition of the N layer were changed.

In Figure 5.6, the reduced temperature $t \equiv (T_c^b - T_c)/T_c^b$ is plotted as a function of d_s for the same data as in Figure 5.5. All four series were found to scale according to:

$$t = \left(\frac{d_o}{d_s}\right)^p \qquad (5.2)$$

with $1 \leq p < 1.7$. All Nb/CuX series studied show this behavior. Values for p and the scale factor d_o for the series in Figure 5.6, for all other measured series, and for data on V/Fe multilayers taken from Wong et al.,[2,4,41] are listed in Table 5.1.

Thin, non-magnetic N interlayer series (2.0 nm of Cu or CuGe(5%)) were best fit using $p = 1$. As the non-magnetic interlayer thickness was increased, p increased systematically reaching an average of 1.24 for samples having decoupled S layers. Series having CuMn layers showed a rapid increase of both p and d_o as y was increased. These changes were related to the destruction of pairs by the Mn spins. In the decoupled limit ($d_n > d^*_{nc} \sim$ 60 nm) p was not significantly dependent on y, which showed that T_c^m was nearly independent of y for all d_s. That p was larger for CuMn interlayered series than for similar Cu or CuGe series indicated that the Mn ions did significantly alter the superconducting state of the multilayer.

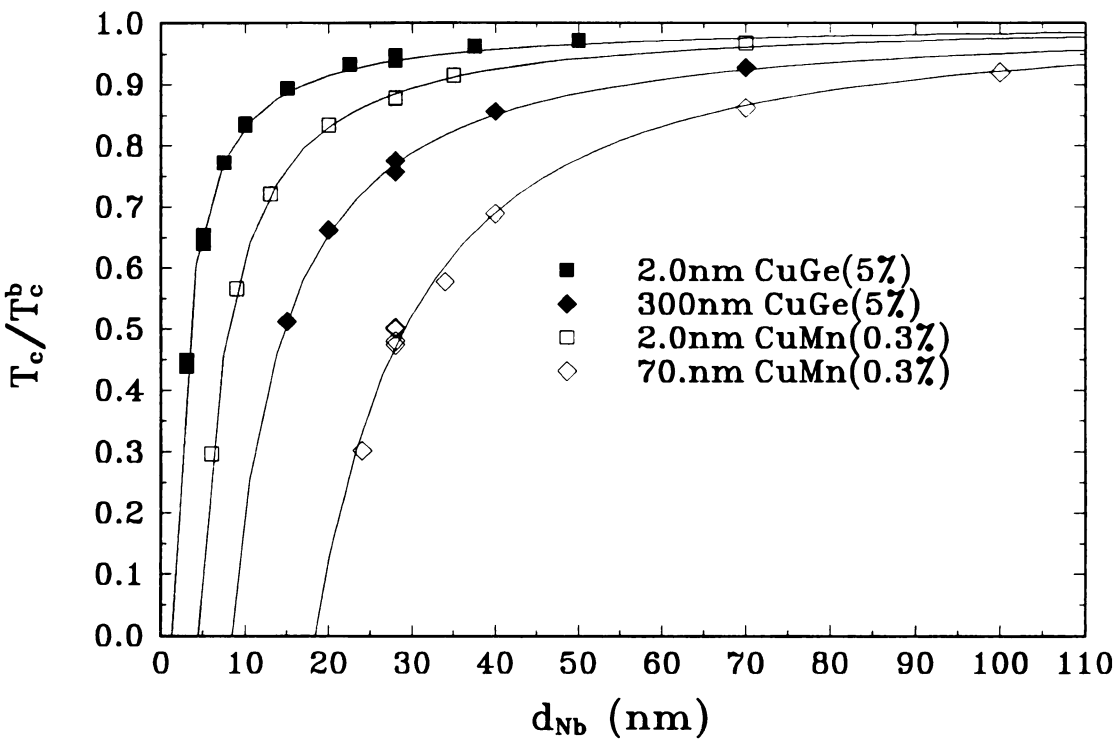

Figure 5.5: Normalized superconducting transition temperature T_c/T_c^b vs. Nb layer thickness. Solid lines are the results of fits to Equation (5.2).

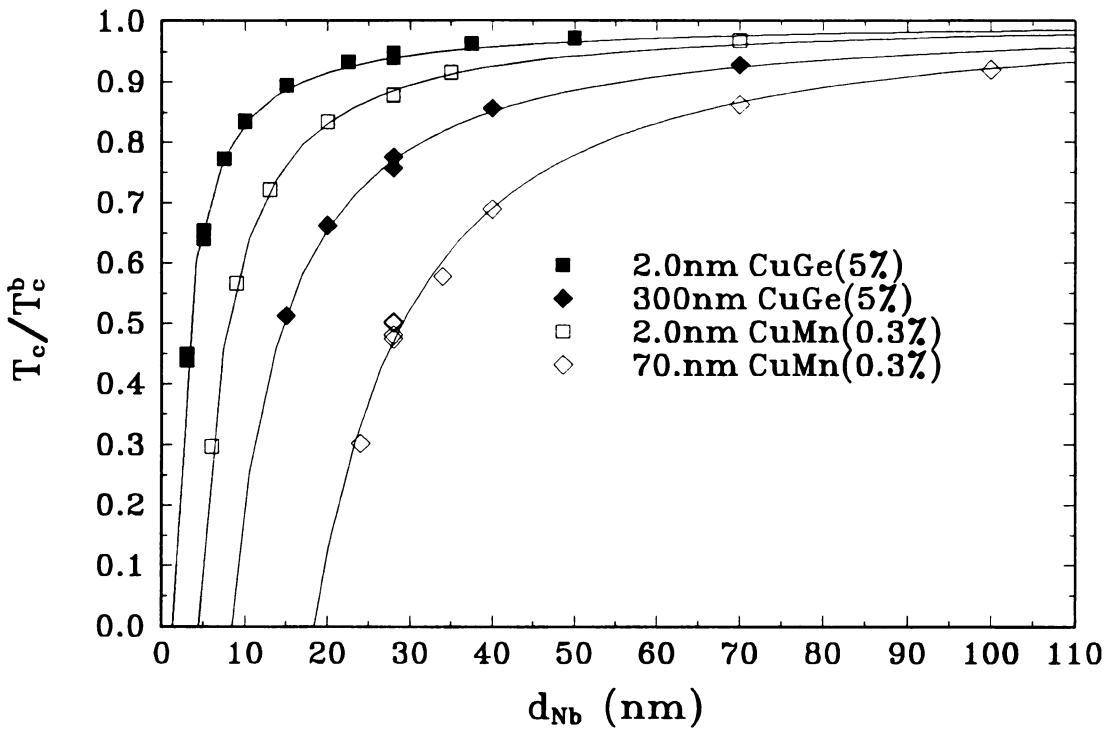

Figure 5.5: Normalized superconducting transition temperature T_c/T_c^b vs. Nb layer thickness. Solid lines are the results of fits to Equation (5.2).

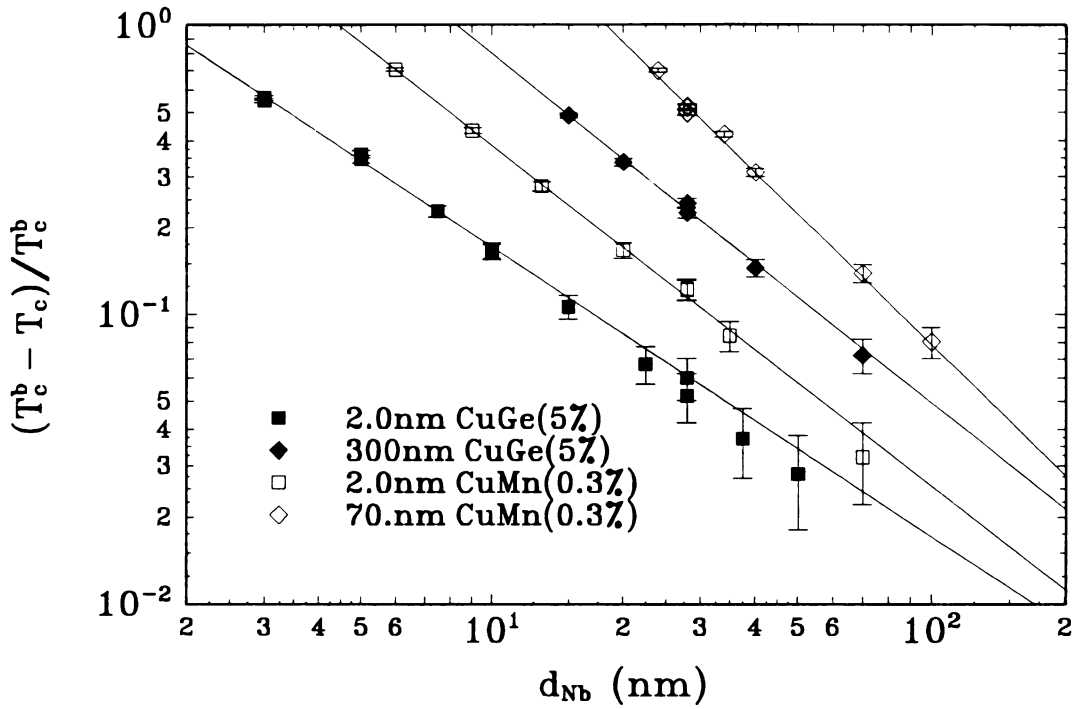

Figure 5.6: Reduced superconducting transition temperature t vs. Nb layer thickness for the same data series as in Figure 5.5. Solid lines are the results of fits to Equation (5.2).

Table 5.1: Scaling parameters for $T_c(d_s)$. *Data from Wong et al.[2,4,41]

Interlayer	d_n (nm)	d_o (nm)	p
CuGe(5%)	2.0	1.70 ± 0.03	1.00 ± 0.02
CuGe(5%)	20.	4.6 ± 0.1	0.99 ± 0.03
CuGe(5%)	300.	8.3 ± 0.2	1.21 ± 0.04
Cu	2.0	1.76 ± 0.04	0.98 ± 0.02
Cu	40.	7.4 ± 0.4	1.08 ± 0.08
Cu	300.	13.6 ± 0.4	1.27 ± 0.06
CuMn(0.3%)	2.0	4.45 ± 0.04	1.18 ± 0.02
CuMn(0.3%)	20.0	14.3 ± 0.2	1.35 ± 0.02
CuMn(0.3%)	70.0	18.3 ± 0.6	1.50 ± 0.10
CuMn(1.5%)	2.0	8.6 ± 0.1	1.42 ± 0.03
CuMn(2.2%)	2.0	9.4 ± 0.2	1.45 ± 0.04
CuMn(2.2%)	6.0	15.2 ± 0.2	1.38 ± 0.02
CuMn(2.2%)	70.0	20.0 ± 0.5	1.64 ± 0.10
V/Fe*	0.27	13.1 ± 0.1	1.26 ± 0.02
V/Fe*	0.41	21.8 ± 0.3	1.42 ± 0.05
Fe/V/Fe*	~5.0	12.5 ± 0.6	1.10 ± 0.04

To provide a check of Equation (5.2) in the extreme magnetic limit, data published by Wong et al. on T_c in V/Fe multilayers[2,4] and Fe/V/Fe sandwiches[41] have been reanalyzed. Their data on V/Fe multilayers was published as T_c as a function of d_n for various constant values of d_s. These data have been interpolated to extract sets of T_c as a function of d_s at two values of d_n, 0.27 nm and 0.41 nm. These extracted data sets could be scaled according to Equation (5.2) indicating that this relationship holds for strongly magnetic N. In addition, similar trends in the dependence of p and d_o on the N layer thickness were found (Table 5.1).

The Fe/V/Fe sandwich data, however, did not agree with either the V/Fe multilayer results or with those observed in the Nb/CuX studies. In V/Fe/V sandwiches, $p \approx 1$ while $p > 1.4$ would have been more consistent with the multilayer data. Wong et al. noted that the T_c's of multilayers having thick Fe layers (approximately equal to those used in the sandwich films) deviated from the behaviors they had observed in samples having smaller Fe thicknesses.[4] They proposed that their observed deviations at large d_n were related to a change in the internal structure of the multilayer but were unable to validate this proposal.

All these experimental data indicate that the superconducting state of the S material is altered in a different fashion by magnetic N layers than by non-magnetic N layers. A qualitative model for the mechanism behind the dependence of T_c on d_n for varying Mn concentration has been included above, but an explanation of the dependence of p and d_o on y and d_n requires a more careful theoretical treatment.

5.2 T_c Theory

Most models of proximity effect superconductivity can be classified into two general forms: those based on McMillan's model;[42] and those based on de Gennes and Guyon's model.[43] Both these forms were originally derived in the early 1960's, but much

work has been done on refining them. Of particular interest are extensions of these models to the case of magnetic normal layers. The appropriate extension of McMillan's model was developed by Kaiser and Zuckermann (KZ)[44], while de Gennes and Guyon's model was extended by Hauser, Theuerer, and Werthamer (HTW).[14,45,46]

These models are similar in that they both require that the electron mean-free-path of the S and N material ℓ_i^o is less than its respective coherence length ξ_i^o where i stands for the S or N material. This assumption, known as the dirty limit approximation, has proven vital in making the proximity effect problem tractable. There are other models that relax this constraint but their final forms have proven too complex to be applied here.[28]

The primary difference between these two model classes lies in how they treat the boundary conditions at the S-N interface and the spatial dependence of the superconducting pair function within each layer F(z). F(z) is defined as $\Delta(z)/V(z)$, where $\Delta(z)$ is the position dependent superconducting gap parameter, and V(z) is the position dependent electron-phonon coupling parameter. The importance of F(z) is that it is directly proportional to the superconducting pair density at each position, z, within the multilayer. Due to the nature of the differences between these models, each will be discussed in turn, then both models will be compared to the experimental data.

5.2.1 The KZ Model

The KZ model will be introduced by developing the basic concepts and assumptions needed for the model, then the results will be written down and expanded upon in a few limiting cases.

KZ's first assumption was that a multilayered sample can be described as a series of bilayer films as shown in Figure 5.7, where the thickness of each layer in the bilayer is half the thickness of that layer in the multilayer. This assumption is justified because the

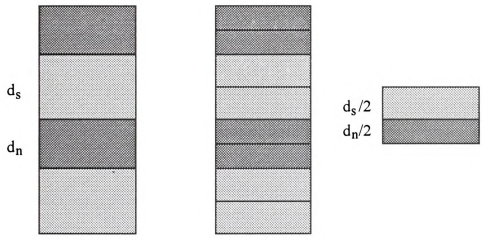

Figure 5.7: Multilayer to bilayer deconvolution.

superconducting boundary conditions on the metallic side of a superconductor-vacuum interface are the same as those appearing at the center of a symmetric S or N layer.

The next, and perhaps most important assumption was that both layers were much thinner than their respective coherence lengths, but they are thicker than their respective mean-free-paths: $\ell_i^o < d_i << \xi_i^o$. Since $d_i << \xi_i^o$, F(z) is expected to vary only slightly across each layer which leads to the condition that F(z) is approximately given by:

$$F(z) = \begin{cases} F_n \text{ in the N layer} \\ F_s \text{ in the S layer} \end{cases} \qquad (5.3)$$

Therefore, F(z) is discontinuous at the S-N boundaries. This may seem to be a rather severe constraint; however, as will be shown below, the KZ model is applicable for many of the systems studied here.

Although F(z) is discontinuous at the S-N interface, there are still matching conditions to be taken into account. Kaiser and Zuckermann created boundary conditions at the S-N interface by treating the interface as a superconducting-pair tunneling barrier. The basic energy scales arising from this barrier are:

$$\Gamma_n = \frac{\pi}{2} T^2 A d_s N'_s(0) = \hbar / 2\tau_n \tag{5.4}$$

$$\Gamma_s = \frac{\pi}{2} T^2 A d_n N'_n(0) = \hbar / 2\tau_s \tag{5.5}$$

where T is the tunneling matrix element, A, the area of the interface, $N'_i(0)$ is the density of states per unit volume at the Fermi energy, τ_i is an associated response time, and i stands for the S or N material. They also showed that τ_n can be given by:

$$\tau_n = \frac{B d_n}{v_{f,n}\,\sigma} \tag{5.6}$$

where $2Bd_n$ is the distance traveled by an electron in N between collisions with the S-N interface, B is a parameter related to the relative magnitudes of ℓ°_n and d_n and is expected to be approximately 2 for a clean layer, σ is the transmission probability across the S-N interface, and $v_{f,n}$ is the Fermi velocity in N. This form for τ_n is simply the average time an electron spends in N before tunneling back into S. Since Equation (5.6) predicted that Γ_n was proportional to $1/d_n$, KZ also assumed that Γ_s was proportional to $1/d_s$.

With these approximations, two new length scales, c_n and c_s, were defined which characterize the effect of superconductivity in the N and S materials:

$$c_i = \frac{\Gamma_i}{\Delta_b} d_i \tag{5.7}$$

where i represents the S or N material, and Δ_b is the bulk gap parameter in S. The ratio $c_n/c_s = N'_s(0)/N'_n(0)$, hence c_s and c_n are not independent parameters.

The final approximation was the inclusion of magnetic impurity effects within the N layer in terms of a magnetic coupling parameter Γ:

$$\Gamma = \frac{\pi}{2} y N'_n(0) J^2 S(S+1) \tag{5.8}$$

where J is the s-d exchange coupling constant, S is the spin of the magnetic ion, and y is the concentration of magnetic impurities. This form treats magnetic spins in the Born approximation and does not include effects due to impurity-impurity interactions or the Kondo state.

With all the terms defined and approximations clear, the equations used for calculating $T_c(d_s, d_n, y)$ are:

$$\ln\left(\frac{T_c^b}{T_c}\right) = \sum_{n=0}^{n_{max}} \left[\frac{1}{n+1/2} - \frac{1}{n+1/2+\varsigma_s}\right] \tag{5.9}$$

$$\varsigma_s = \frac{2c_s}{d_s} \frac{(2n+1)t^* + g}{2t^*\left((2n+1)t^* + g + \frac{2c_n}{d_n}\right)} \tag{5.10}$$

$$t^* = \frac{k_b T_c}{\Delta_b} \tag{5.11}$$

$$g = \frac{\Gamma}{\Delta_b} \tag{5.12}$$

where k_b is Boltzmann's constant, T_c is the superconducting transition temperature of the multilayer, and T_c^b is the superconducting transition temperature in bulk S. In most superconductors, the bulk gap parameter Δ_b is related to T_c^b by $\Delta_b = \beta k_b T_c^b$ with β approximately equal to 1.67 (in Nb, $\beta = 1.90$).[47] The uppermost integer n_{max} contained in the sum is set by including only energies below the Debye energy of S and hence $(2n_{max}+1)T_c < \Theta_D$ where Θ_D is the Debye temperature. This typically results in an $n_{max} > 20$.

Due to the complexity of these equations, it is difficult to get a qualitative understanding of how T_c^b behaves for varying d_s, d_n, and y. Therefore, they have been simplified in two limits: very large magnetic impurity concentration, i.e., $g >> c_n/d_n$; and small d_n, i.e., $d_n/d_s << 1$ and $g << c_n/d_n$.

In the strongly magnetic limit, ς_s is given by

$$\varsigma_s \cong \frac{2c_s}{d_s}\frac{1}{2t^*} \tag{5.13}$$

Since ς_s is no longer dependent on n, and assuming that n_{max} is large, the summations were approximated by a digamma function $\Psi(x)$.

$$\sum_{n=0}^{\infty}\left[\frac{1}{n+1/2}-\frac{1}{n+1/2+\varsigma_s}\right]=\Psi\left(\frac{1}{2}+\varsigma_s\right)-\Psi\left(\frac{1}{2}\right) \tag{5.14}$$

One can further simplify the digamma functions using:

$$\Psi\left(\frac{1}{2}+\varsigma_s\right)-\Psi\left(\frac{1}{2}\right)\cong \ln\left(1+\frac{\pi^2}{2}\varsigma_s\right) \tag{5.15}$$

which is valid for $\varsigma_s < 6$.[47] Unfortunately, this approximation cannot be checked since there is no good way to determine the magnitude of c_s. Without this assumption, however, Equation (5.14) cannot be simplified. Justification for use of Equation (5.15) here will be addressed when the resulting equation for T_c is compared to the experimental data. Combining Equations (5.13), (5.14), and (5.15) lead to a single equation for T_c:

$$\frac{T_c^b}{T_c}\cong 1+\frac{\pi^2}{2}\frac{2c_s}{d_s}\frac{1}{2t^*}\cong 1+\frac{\pi^2}{2}\frac{c_s}{d_s}\frac{T_c^b}{T_c}\beta \tag{5.16}$$

where $\beta = \Delta_b/k_b T_c^b$. This was further simplified to

$$t = \frac{T_c^b - T_c}{T_c^b} \cong \frac{\pi^2}{2}\beta\frac{c_s}{d_s} \tag{5.17}$$

Note here that **all** effects of the N layer are removed. This may seem counter-intuitive, but is markedly similar to the behavior observed in Nb/CuMn multilayers in the limit of thick CuMn layers (see Figure 5.2).

The other limit of interest is that of very small d_n. In this case:

$$\varsigma_s \cong \frac{1}{2t^*}\left((2n+1)t^* + g\right)\frac{c_s}{d_s}\frac{d_n}{c_n} << 1 \tag{5.18}$$

Unlike the large g case, the resulting ς_s is dependent on n. To obtain summations in the form of a digamma function requires a shuffling of the various terms appearing within the sum. After some lengthy algebra one obtains:

$$\ln\left(\frac{T_c}{T_c^b}\right) \cong \sum_{n=0}^{\infty}\left[\frac{1 \pm {c_s d_n}/{c_n d_s}}{n+1/2} - \frac{1 - {c_s d_n}/{c_n d_s}}{n+1/2+\frac{g}{2t^*}\frac{c_s d_n}{c_n d_s}}\right] \tag{5.19}$$

$$\cong \left(1-\frac{c_s d_n}{c_n d_s}\right)\left[\Psi\left(\frac{1}{2}\right) - \Psi\left(\frac{1}{2}+\frac{g}{2t^*}\frac{c_s d_n}{c_n d_s}\right)\right] + \frac{c_s d_n}{c_n d_s}\zeta \tag{5.20}$$

where ζ is defined by

$$\zeta = \sum_{n=0}^{n_{max}}\frac{1}{n+1/2} \tag{5.21}$$

For typical values of T_c, and Θ_D, $n_{max} \cong 20$ and $\zeta \cong 2.5$. Hence, for $d_n/c_n << 1$, one also finds that $\zeta d_n / c_n << 1$. Equation (5.15) is again used to simplify the digamma functions yielding:

$$\frac{T_c^b}{T_c} \cong e^{\left(\zeta \frac{c_s d_n}{c_n d_s}\right)} \left[1 + \frac{\pi^2}{4} \frac{g}{t^*} \frac{c_s d_n}{c_n d_s}\right]^{\left(1 - \frac{c_s d_n}{c_n d_s}\right)} \tag{5.22}$$

which simplifies to:

$$t = \frac{T_c^b - T_c}{T_c^b} \cong \left(\frac{\pi^2}{4} g\beta + \zeta\right) \frac{c_s}{c_n} \frac{d_n}{d_s} \tag{5.23}$$

Making use of the relation between the c_i's results in:

$$t \cong A d_s^{-1} \tag{5.24a}$$

where

$$A = \begin{cases} \dfrac{\pi^2}{4} \beta c_s & \text{for } g >> \dfrac{c_n}{d_n} \\ \left(\dfrac{\pi^2}{4} g\beta + \zeta\right) \dfrac{N_n(0)}{N_s(0)} d_n & \text{for } \dfrac{d_n}{c_n} << 1 \text{ and } g << \dfrac{c_n}{d_n} \end{cases} \tag{5.24b}$$

for the two limits of the model. Numerical analysis utilizing the full equations for values of g and d_n between these limits shows that this model can always be approximated by $t \propto d_s^{-1}$.

5.2.2 The HTW Model

A more complete theoretical model than McMillan's was developed by de Gennes and Guyon,[43] and refined to include magnetic effects by Hauser, Theuerer, and Werthamer (HTW).[14,46,47] This model treats the explicit position dependent pair function F(z) within the S and N layers. Although HTW also assumes the dirty superconducting limit approximation and that a multilayer can be approximated by a half-thickness bilayer, they place no limitations on d_n or d_s. In addition, rather than describing the S-N interfacial boundary conditions by a tunneling barrier as done by McMillan and KZ, HTW have developed more precise microscopic continuity conditions for the interface.

They approximate F(z) by

$$F(z) \propto \begin{cases} \dfrac{\cos(k_s(z-d_s/2))}{\cos(k_s d_s/2)} & 0 \le z \le d_s/2 \\ \dfrac{\cosh(k_n(z+d_n/2))}{\cosh(k_n d_n/2)} & -d_n/2 \le z \le 0 \end{cases} \qquad (5.25)$$

where k_n and k_s are inverse length scales to be defined below. The boundary conditions on F at the S-N interface are that both

$$\frac{F(z)}{N'(z)} \qquad \text{and} \qquad \frac{d}{dz}\ln(F(z))$$

are continuous across the N-S interface where N'(z) is the position dependent density of states in the bilayer. When these boundary conditions are combined with the assumption that N'(z) is given by N'_n in N and N'_s in S one finds:

$$k_s N'_s \eta_s^2 \tan(k_s d_s/2) = k_n N'_n \eta_n^2 \tanh(k_n d_n/2) \qquad (5.26)$$

where η_i is the effective superconducting coherence length in the S and N materials. Here η is used for the coherence length to avoid confusion in the upper critical field chapter where there will be two quite different forms for the coherence length. In the HTW model, η_i is defined as

$$\eta_i^2 = \frac{\hbar v_{f,i} \ell_i}{6\pi k_b T_c} \cong \frac{\pi \hbar k_b}{6e^2 T_c} \frac{1}{\gamma_i \rho_i} \qquad (5.27)$$

where $v_{f,i}$ is the Fermi velocity, e is the electron charge, γ_i is the coefficient of the linear term in the low temperature specific heat, ρ_i is the resistivity and i represents either the N or S material. The approximate term in Equation (5.27) was derived by HTW and is based on use of Pippard's expressions relating $v_{f,i}$ and ℓ_i to the measurable quantities γ_i and ρ_i.[48]

Utilizing these expressions, the final equations for T_c in a superconducting multi-layer are:

$$k_s N'_s \eta_s^2 \tan(k_s d_s/2) = k_n N'_n \eta_n^2 \tanh(k_n d_n/2) \qquad (5.28)$$

$$\ln\left(\frac{T_c^b}{T_c}\right) = X(\eta_s^2 k_s^2) \qquad (5.29)$$

where,

$$k_n^2 = \frac{1}{\eta_n^2}\left(1 + \alpha \frac{T_c^b}{T_c}\right) \qquad \alpha = \frac{\hbar}{2\pi k_b T_c^b} \frac{1}{\tau_m}$$

$$\chi(x) = \Psi(1/2 + x/2) - \Psi(1/2) \tag{5.30}$$

and τ_m is the magnetic scattering time in the N material.

An additional simplification is made by noting that γ_i is linearly proportional to N'_i.[49] This allows the ratio N'_n/N'_s to be approximated by γ_n/γ_s. Equation (5.28) then becomes:

$$k_s \tan(k_s d_s/2) = k_n \frac{\rho_s}{\rho_n} \tanh(k_n d_n/2) \tag{5.31}$$

As with the KZ model, a visual inspection of the HTW model does not lead to an easy understanding of its underlying physics. To make a comparison of the similarities and differences between the two models, the HTW model will be examined in the same limits as the KZ model: strong magnetism ($\alpha >> 1$), and small d_n ($k_n d_n << 1$).

In the limit of large α :

$$k_n^2 = \frac{1}{\eta_n^2}\left(1 + \alpha \frac{T_c^b}{T_c}\right) >> \frac{1}{\eta_n^2} \tag{5.32}$$

and, therefore,

$$k_n d_n >> 1 \tag{5.33}$$

provided that d_n is not very small. This implies that $\tanh(k_n d_n/2) \cong 1$, and that,

$$\tan(k_s d_s/2) \cong \frac{k_n}{k_s}\frac{\rho_s}{\rho_n} >> 1 \tag{5.34}$$

and, hence, that,

$$k_s d_s / 2 \cong \frac{\pi}{2} \tag{5.35}$$

Substituting this into Equation (5.29) and using Equation (5.15) for the digamma function, one arrives at a single equation for T_c:

$$\frac{T_c^b - T_c}{T_c^b} \cong \frac{\pi^4}{4} \eta_{so}^2 d_s^{-2} \tag{5.36}$$

where η_{so} is η_s evaluated at $T_c = T_c^b$. This form is similar to that derived from KZ's model, but it contains a different scaling exponent.

The limit of small d_n follows similar lines:

$$k_n d_n << 1$$

therefore,

$$k_s \tan(k_s d_s / 2) \cong k_n^2 \frac{\rho_s}{\rho_n} \frac{d_n}{2} << 1 \tag{5.37}$$

and,

$$\frac{k_s^2 d_s}{2} \cong k_n^2 \frac{\rho_s}{\rho_n} \frac{d_n}{2} \tag{5.38}$$

Since k_s is small, Equation (5.15) is valid leading to

$$\frac{T_c^b}{T_c} \cong 1 + \frac{\pi^2}{4}\frac{\rho_s}{\rho_n}\frac{\eta_s^2}{\eta_n^2}\left(1 + \alpha\frac{T_c^b}{T_c}\right) \tag{5.39}$$

and

$$\frac{T_c^b - T_c}{T_c^b} \cong \frac{\pi^2}{4}\frac{\gamma_n}{\gamma_s}(1+\alpha)\frac{d_n}{d_s} \tag{5.40}$$

which has the same functional form as that derived from the KZ model in the thin N limit.

Therefore, the HTW model predicts that T_c is given approximately by:

$$t \cong \begin{cases} \dfrac{\pi^4}{4}\eta_{so}^2 d_s^{-2} & \text{for} \quad \alpha >> 1 \\ \dfrac{\pi^2}{4}\dfrac{N'_n(0)}{N'_s(0)}(1+\alpha)d_n d_s^{-1} & \text{for} \quad k_n d_n << 1 \end{cases} \tag{5.41}$$

where $N'_n(0)/N'_s(0) \cong \gamma_n/\gamma_s$.

5.3 Model Applications

Before comparing these models to the experimental data, the validity of the assumptions should be verified for both the S and N materials. The primary constraint common to both models was the dirty superconducting limit approximation: $\ell_i^\circ << \xi_i^\circ$. ξ_{Nb}° was determined from the temperature dependence of the superconducting upper critical field measured in a thin Nb film and is listed in Table 5.2.

The normal metal coherence length cannot be directly measured. Instead, it was estimated using a form similar to HTW's expression for η_s:[50]

$$\xi_n^\circ \cong \frac{\pi\hbar k_b}{2e^2 T}\frac{1}{\gamma_n(\rho\ell)_n} \tag{5.42}$$

where the temperature T used in estimating ξ_n° was the highest temperature of physical interest, in the present case $T = T_c^b$ for Nb. $(\rho\ell)_n$ was assumed to be unchanged by the small concentrations of impurities used in the CuX alloys, and therefore was approximately $6.60\text{x}10^{-16}\ \Omega\text{m}^2$.[51] γ_n for Cu and CuGe have been measured,[52,53] and are listed in Table 5.2. For CuMn, γ_n can not be simply measured because magnetic contributions to the specific heat mask the electronic contribution. Therefore, γ_n for CuMn(y) was assumed to be the same as for CuGe(y), these values are also listed in Table 5.2. The resulting ξ_n°'s are listed in Table 5.2.

In any material, ℓ_i° is approximately given by:

$$\ell_i^\circ \cong \frac{(\rho\ell)_i}{\rho_i^\circ} \tag{5.43}$$

where ρ_n° is the bulk resistivity of N, and $(\rho\ell)_n$ is the finite-size correction to the resistivity. For Nb $(\rho\ell) = 3.2\text{x}10^{-16}\ \Omega\text{m}^2$.[51] The measured ρ_n°'s and the resulting ℓ_i°'s are also listed in Table 5.2.

Thus, the dirty limit approximation ($\ell_i^\circ << \xi_i^\circ$) is valid for all the CuX materials used, with the exception of pure Cu. For Cu, as d_{Cu} is decreased, ℓ_{Cu} also decreases according to:

Table 5.2: Nb and CuX length scales.

	Nb	Cu	CuMn(0.3%)	CuMn(2.2%)	CuGe(5%)	Units
γ_i	709.4	96.8	98.4	102.1	108.8	J/m^3K^2
ρ_i°	7.2	0.5	3.4	9.4	19.4	$10^{-8}\Omega\cdot m$
ℓ_i°	4.4	130	19	7.0	3.4	nm
ξ_i°	33	160	160	150	140	nm

$$\frac{1}{\ell_n} \cong \frac{1}{\beta \ell^{\circ}_n} + \frac{1}{d_n} \tag{5.44}$$

where β is a constant of order 3/8 for thin films.[51] Therefore, sufficiently thin Cu layers should also be described by the dirty limit approximation.

The agreement between the KZ and HTW models in the small d_n limit implies that they are approaching a functional form that is independent of the approximations used in the derivation of each model. Although the two models agree on the form of the equation, they predict significantly smaller values for d_o than were found experimentally (d_o^{KZ} = 0.93, d_o^{HTW} = 1.17, while d_o^{CuGe} = 1.70±.03).[54] One possible explanation for this discrepancy is that the superconducting properties of the Nb layers change with d_s resulting in an effective T_c^b which decreases with decreasing d_s. Since these changes are related to changes in the thin Nb layers, we assume that T_c in the limit that $d_n \sim 0$ is given by T_c^f, where T_c^f was defined in Equation (5.1). Replacing T_c^b in Equation (5.2) with T_c^f given by Equation (5.1) and recollecting terms, one finds:

$$\frac{\left(T_c^b - T_c\right)}{T_c^b} \cong \left(\frac{d_o + d_o^f}{d_s}\right)^1 \tag{5.45}$$

Therefore, the dependence of T_c^f on d_s changes only the length scaling factor d_o, and does not significantly change the scaling exponent *p*. This increase in the effective d_o provides a good rationalization of the discrepancy between the HTW and KZ predictions and the experimental values of d_o.

For other limits KZ always predicts $t \propto d_s^{-1}$ which may simply indicate that the KZ model is always dominated by the thin layer limit. HTW's model, on the other hand, shows a significant change in *p* with increased magnetic impurity concentration. In

particular the HTW results imply that as α increases from 1 toward ∞, p should change from 1 to 2. This was the trend observed in Nb/CuMn and V/Fe multilayers as either the magnetic ion concentration or magnetic layer thickness was increased. The finding that the experiments do not show $p = 2$ may indicate that the strongly magnetic limit of the theoretical models is not a limit accessible by experiment, or simply that data have not been taken for sufficiently large α.

To summarize, in S/N multilayers T_c displays a power-law dependence on the S layer thickness. This form [Equation (5.2)] holds for all N layer thicknesses, mean-free-paths, and magnetic ion concentrations studied. In addition, the observed scaling law is predicted by the limiting forms of the HTW and KZ models. While these models appropriately predicted the observed increase of the scaling exponent p with increasing magnetic concentration, an effective depression of T_c^b with decreasing Nb thickness (consistent with behavior observed in single Nb films) was required for the models to adequately predict values for the scale factor d_o.

CHAPTER 6
THE SUPERCONDUCTING UPPER CRITICAL FIELD

6.1 Introduction

In this chapter, the superconducting upper critical field H_{c2} will be used to gain insight into the importance of proximity effect coupling and pair penetration in a superconducting/normal metal (S/N) multilayer. As was noted in the previous chapter, T_c experiments alone could not determine whether the observed behavior of T_c was related to the coupling strength between S layers or more simply to the penetration, and further loss, of superconducting pairs into N.

In a bulk superconductor, anisotropy of $H_{c2}(T)$ is related to the inherent anisotropy of the superconductor. In a S/N multilayer, the physical layering can induce a periodicity, and hence an anisotropy, in the superconducting properties. In such a layered anisotropic superconductor one can define two limiting values of H_{c2}: $H_{c2\perp}$ for external magnetic fields directed perpendicular to the layers, and $H_{c2\parallel}$ for external magnetic fields directed parallel to the layers. The physical processes which determine the magnitude of the anisotropy of H_{c2} are the pair penetration of superconductivity into N, proximity effect coupling between S layers, how the magnetic fields penetrate into the S and N layers, the vortex structure of the resulting flux-penetrated state, and how the superconductivity induced in N is destroyed as H and T are varied.

When a weak magnetic field is applied to a superconducting sample, surface currents spontaneously form to shield the sample's interior from the applied field. At large field densities, superconductivity will be destroyed and the sample will behave like a normal metal in a magnetic field. In type II superconductors, there exists an intermediate state in which the external field penetrates the interior of the superconductor without totally destroying the superconducting state. This intermediate state is then characterized

by two magnetic field strengths, H_{c1} the lower critical field, where magnetic flux first penetrates the sample, and H_{c2}, the upper critical field, where the superconducting state is finally destroyed.

Magnetic flux penetrates a superconductor in the form of thin flux filaments, or fluxoids, each of which is surrounded by a circulating superconducting current vortex. The electrons in a superconductor are quantum mechanically phase coherent. Therefore, the angular momentum of each electron must be quantized. This leads to quantization of the magnetic flux enclosed within each vortex. The flux quantum Φ_o is defined as $\hbar/2e$ where $\hbar$ is plank's constant and e is the electron charge.

At the center of each vortex, the superconducting pair density ρ_{pair} is nearly zero. It grows back toward its bulk value over a length scale ξ known as the superconducting coherence length. Therefore, the core of a vortex is typically regarded as having a radius of ξ.

The vortices, which repel one another, crystallize into an ordered array. In most cases the array is triangular with a vortex-vortex spacing d_H given by

$$d_H = \left(\frac{\Phi_o}{2\pi H}\right)^{1/2} \qquad (6.1)$$

where H is the applied magnetic field strength. As H is increased, d_H decreases until $d_H \sim \xi$. For larger H, the superconducting state is destroyed. This defines the upper critical field H_{c2} as

$$H_{c2} = \frac{\Phi_o}{2\pi\xi^2} \qquad (6.2)$$

Hence, a measurement of H_{c2} allows one to determine ξ.

The superconducting theory of Bardeen, Cooper, and Schriefer[55] shows that ξ is related to the superconducting gap parameter Δ by

$$\xi = \frac{\hbar v_f}{\pi \Delta} \tag{6.3}$$

where v_f is the Fermi velocity of the superconductor. The temperature dependence of ξ is then primarily due to the temperature dependence of $\Delta(T)$. The superconducting order parameter is defined as $\Delta(T)/\Delta(0)$, where $\Delta(0)$ is the bulk gap parameter at $T = 0$. Mean field theory predicts that below any second order phase transition (like superconductivity) the order parameter varies with temperature as[56]

$$\frac{\Delta(T)}{\Delta(0)} = \left(\frac{T_c - T}{T_c}\right)^{1/2} \tag{6.4}$$

This implies that near T_c, ξ is given by

$$\xi(T) = \xi(0)\left(\frac{T_c - T}{T_c}\right)^{-1/2} \tag{6.5}$$

and $H_{c2}(T)$ by

$$H_{c2}(T) = H_{c2}(0)\left(\frac{T_c - T}{T_c}\right) \tag{6.6}$$

where $\xi(0)$ and $H_{c2}(0)$ are the zero temperature values of ξ and H_{c2}. As shown in Figure 6.1, this is the behavior observed for $H_{c2}(T)$ near T_c in a 500 nm thick Nb film.

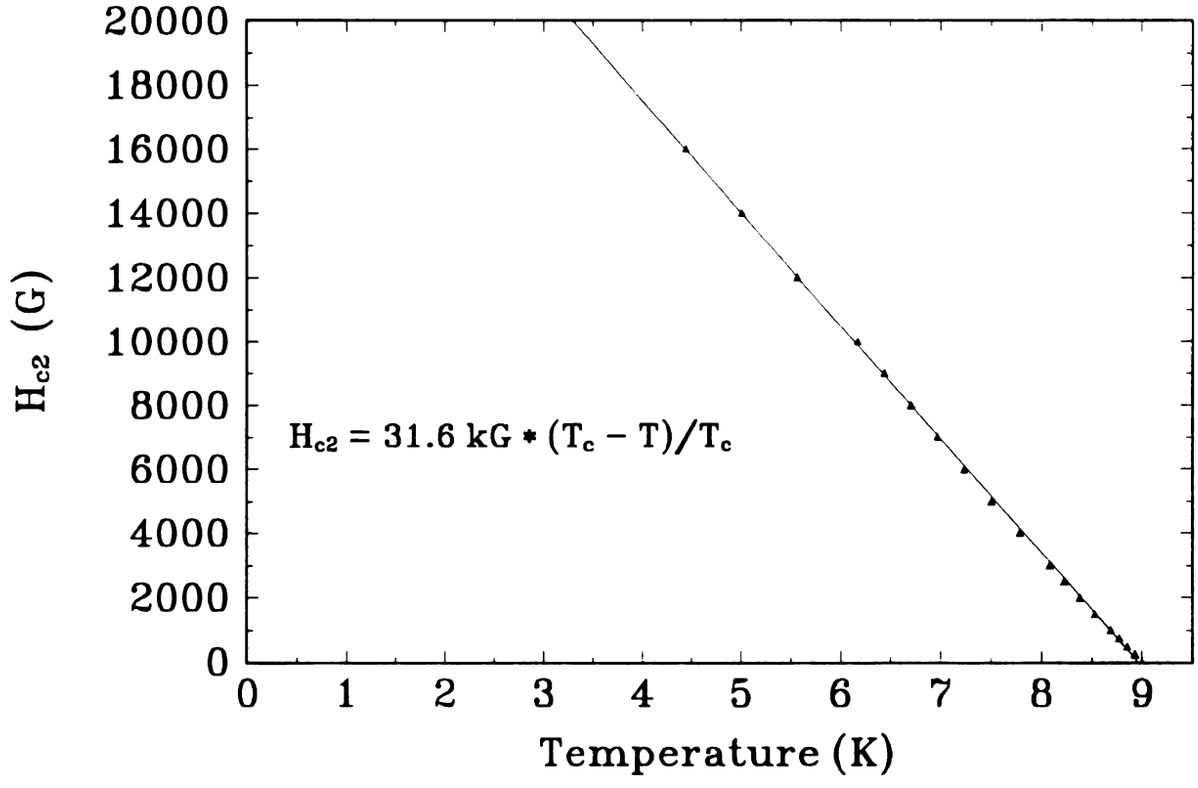

Figure 6.1: $H_{c2}(T)$ for a 500 nm thick Nb film. The line is a linear fit to the data.

In a multilayered superconductor, ξ is no longer isotropic, rather it takes on two primary values, $\xi_{\|}$ or ξ_{xy} for ξ lying in the plane of the layers and ξ_z for ξ directed perpendicular to the layers. This deconvolution of ξ leads to a similar deconvolution of H_{c2} for two different field orientations. Figure 6.2 shows the approximate vortex cores, and definitions of $\xi_{\|}$, ξ_{xy}, and ξ_z for H parallel and perpendicular to the layers. As will be seen later, $\xi_{\|}$ is not necessarily equal to ξ_{xy}.

In a strongly coupled multilayer ($d_n \sim 0$) $H_{c2\|}$ and $H_{c2\perp}$ should vary with temperature similar to the behavior found for an anisotropic bulk superconductor with

$$H_{c2\|} \cong \frac{\Phi_o}{2\pi\xi_{xy}(0)\xi_z(0)}\left(\frac{T_c - T}{T_c}\right) \tag{6.7}$$

and

$$H_{c2\perp} \cong \frac{\Phi_o}{2\pi\xi_{\|}^2(0)}\left(\frac{T_c - T}{T_c}\right) \tag{6.8}$$

Figure 6.3 shows that this behavior was found in strongly coupled multilayers such as Nb/CuGe(5%) 10 nm/10 nm. Since, $H_{c2\|} > H_{c2\perp}$, $\xi_{\|}^2 > \xi_{xy}\xi_z$.

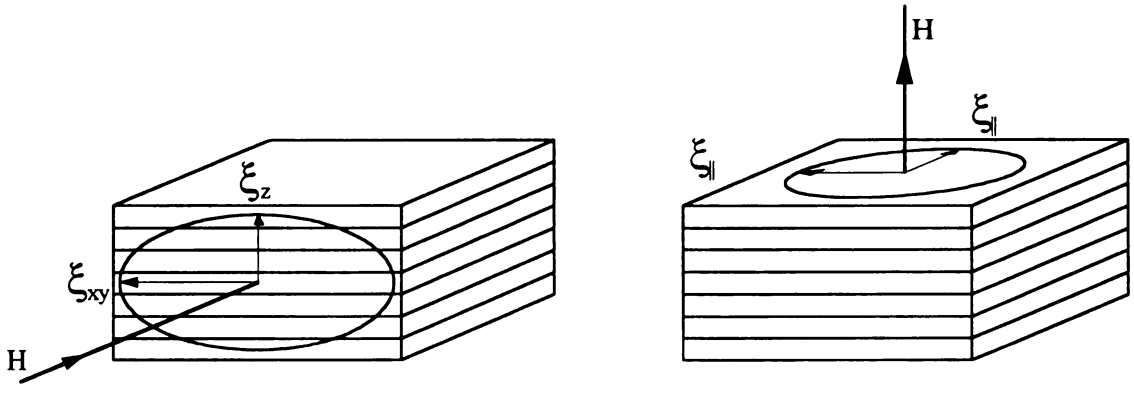

Figure 6.2: A schematic diagram of the vortices in a multilayer showing how ξ_{xy}, $\xi_{\|}$, and ξ_z are defined.

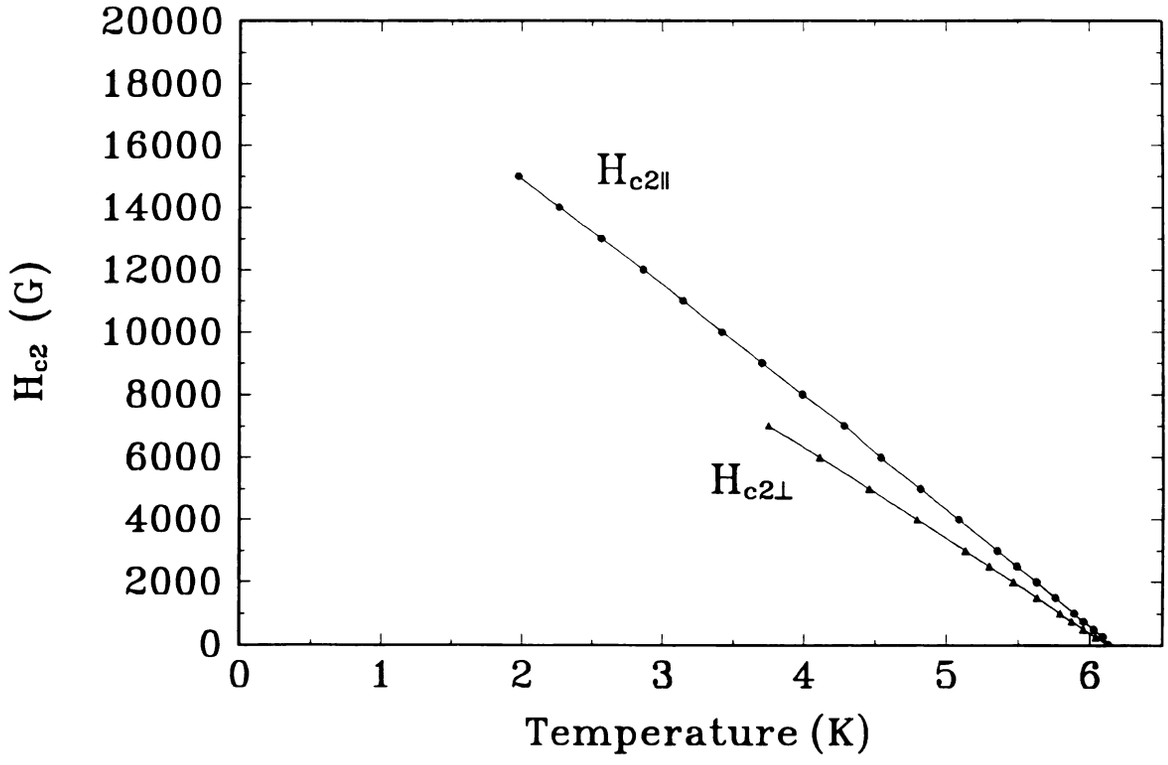

Figure 6.3: $H_{c2\parallel}$ and $H_{c2\perp}$ for Nb/CuGe(5%) 10 nm/10 nm.

In an isolated superconducting film with a thickness $d_s >> \xi_z$, $H_{c2\parallel}$ is approximately equal to $H_{c2}^b(T)$ the upper critical field for bulk S. Therefore, for such a film at low temperatures $\xi_{xy} \cong \xi_z \cong \xi_b$ where $\xi_b(T)$ is ξ in bulk S. As T increases, $\xi_b(T)$ diverges proportional to $(T_c^b - T)^{-1/2}$ until it becomes approximately equal to d_s at a temperature T_{2D}. Since the superconductivity cannot extend beyond the edges of the film, above this temperature ξ_z saturates to the value $d_s/\sqrt{12}$.[56] In addition, at $T > T_{2D}$, the scaling temperature for ξ_{xy} becomes T_c rather than T_c^b.

Therefore, for an isolated superconducting film

$$H_{c2\perp} \cong \frac{\Phi_o}{2\pi\xi_\parallel^2(0)}\left(\frac{T_c - T}{T_c}\right) \tag{6.9}$$

and

$$H_{c2\parallel} \cong \begin{cases} \dfrac{\Phi_o}{2\pi\xi_b^2(0)}\left(\dfrac{T_c^b - T}{T_c^b}\right) & \text{for} \quad T < T_{2D} \\ \dfrac{\Phi_o}{2\pi\xi_{xy}(0)\,d_s/\sqrt{12}}\left(\dfrac{T_c - T}{T_c}\right)^{1/2} & \text{for} \quad T > T_{2D} \end{cases} \tag{6.10}$$

As shown in Figure 6.4, multilayered samples having decoupled S layers show qualitatively similar behavior. Here, however, the penetration of superconductivity into N allows superconductivity to extend beyond d_s which implies that d_s in Equation 6.10 should be replaced by an effective superconductor layer thickness d_s^*.

All of the above variations in $H_{c2\parallel}(T)$ can be observed in a multilayer having intermediate coupling strength, as shown in Figure 6.5 for a Nb/CuMn(0.3%) 40 nm/20 nm multilayer. Near T_c, $H_{c2\parallel}$ is proportional to $(T_c\text{-}T)$ as was expected for a strongly coupled multilayer. Then below a temperature T^*, $H_{c2\parallel}$ varies proportional to $(T_c^*\text{-}T)^{1/2}$ as expected for isolated superconducting layers, where T_c^* is the effective zero field superconducting transition temperature for the 2D state. Finally, at temperatures below T_{2D}, $H_{c2\parallel}(T)$ became approximately equal to $H_{c2}^b(T)$. The transition from 3D (coupled)

behavior to 2D (decoupled) behavior is called dimensional crossover and is related to the temperature and field dependence of superconducting coupling between S layers.

To best describe the differences between $H_{c2\perp}$ and $H_{c2\parallel}$, these data will be analyzed separately. $H_{c2\perp}(T)$ will be considered first because it shows no effect due to dimensional crossover, and is also easier to model theoretically. The analysis of $H_{c2\parallel}$, which follows will focus on two possible mechanisms for dimensional crossover. Finally both $H_{c2\parallel}$ and $H_{c2\perp}$ will be discussed to help discern which of the proposed dimensional crossover models provides a more consistent explanation of the observations.

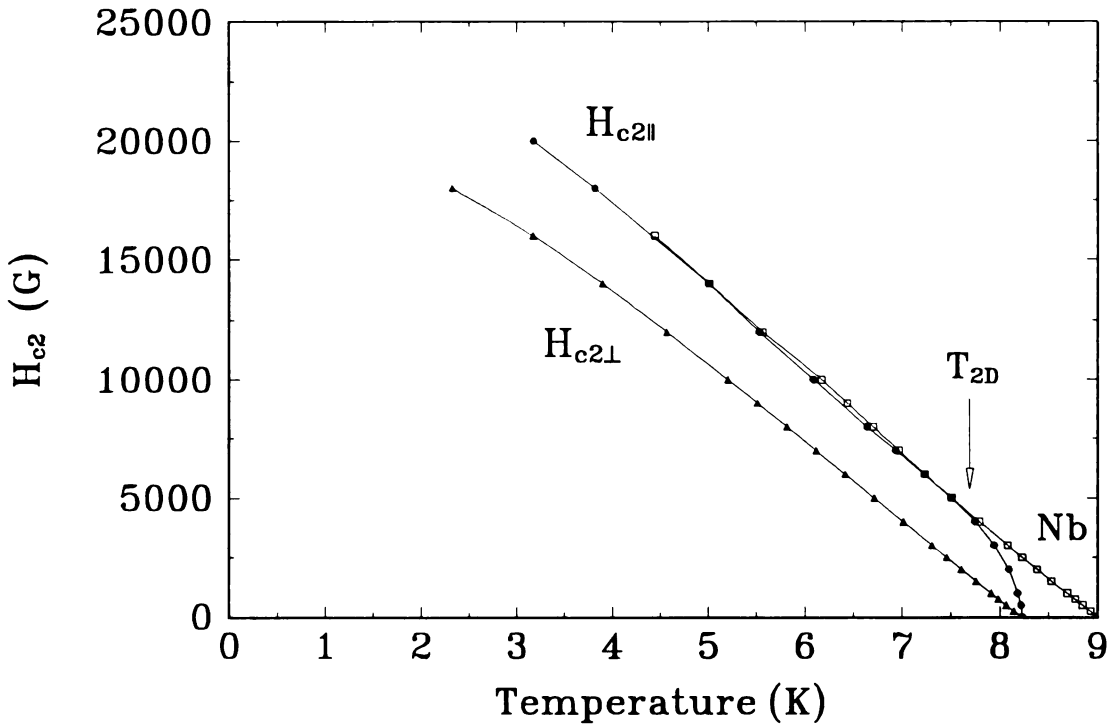

Figure 6.4: $H_{c2\parallel}$ and $H_{c2\perp}$ for Nb/CuGe(5%) 70 nm/300 nm multilayer (filled symbols), and a bulk Nb sample (open symbol).

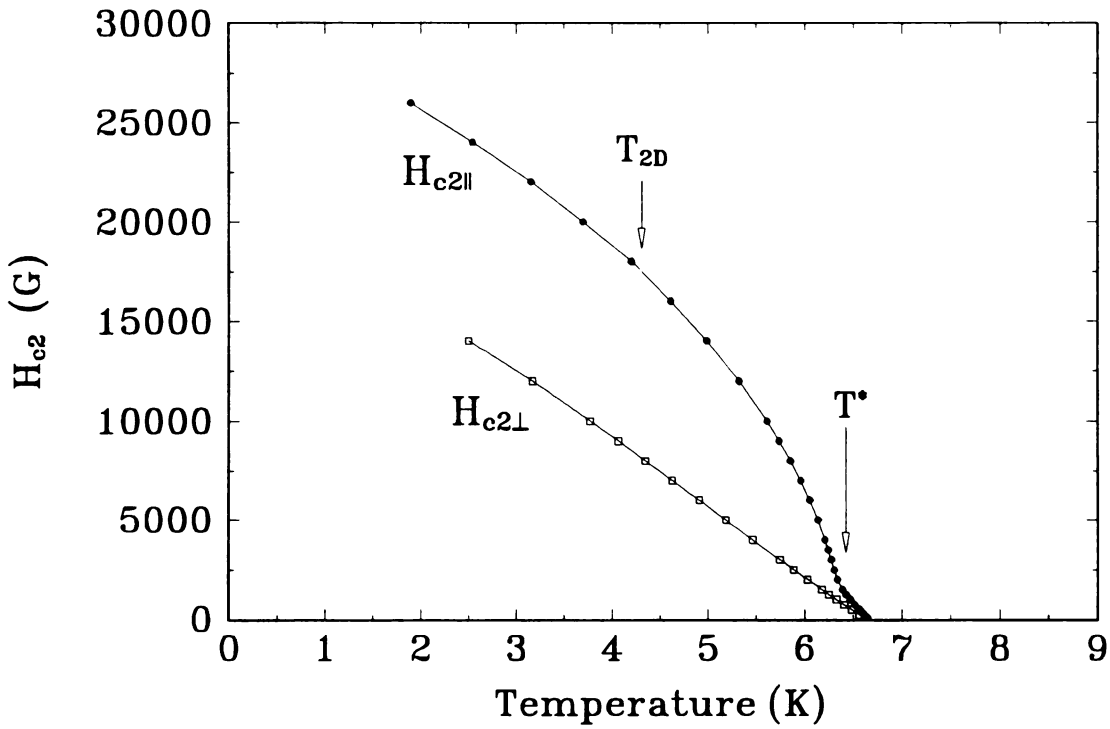

Figure 6.5: $H_{c2\|}$ and $H_{c2\perp}$ in a Nb/CuMn(0.3%) 40 nm/20 nm multilayer.

6.2 The Perpendicular Upper Critical Field

In a layered system with a magnetic field applied perpendicular to the layers, each fluxoid passes through every layer, so $H_{c2\perp}(T)$ should be related to the superconducting properties of the multilayer averaged through the entire thickness of the sample. The superconducting transition temperature T_c, also provided a measure of the average superconducting properties of a superconductor. Therefore, $H_{c2\perp}(T)$ may display some of the same effects which were observed in the studies of T_c.

As discussed in the previous chapter, T_c decreased with increasing d_n, Mn concentration y, and electron mean-free-path ℓ_n, as well as for decreasing d_s. For d_n greater than a critical scale length d^*_{nc}, T_c was found to be independent of d_n, signifying that superconducting pairs penetrate into N roughly a distance d^*_{nc}. d^*_{nc} decreased as either magnetic or non-magnetic impurities were added to N, although the decrease was much more rapid for magnetic impurities. With varying d_s, T_c was found to scale according to

$$\frac{T_c^b - T_c}{T_c^b} \cong \left(\frac{d_s}{d_o}\right)^{-p} \qquad (6.11)$$

where p was observed to increase with increased d_n or y.

By analogy with these T_c trends, $H_{c2\perp}$ should decrease with: increasing y; decreasing d_s; decreasing ℓ_n; and increasing d_n until $d_n > d^*_{n\perp}$ beyond which it should be independent of d_n. Pushing the analogy, one may expect that $H_{c2\perp}$ scales with the S layer thickness as $(H^b_{c2} - H_{c2\perp}) \propto d_s^{-w}$, where w depends on d_n and y similar to the behavior of p.

6.2.1 $H_{c2\perp}$ Experiments

As shown in Figures 6.6-6.10, $H_{c2\perp}(T)$ was found to be proportional to $(T_c - T)$ for most of the CuX material studied. Figures 6.6 and 6.7 show data for Nb/CuGe(5%) samples, while Figures 6.8 and 6.9 present it for Nb/CuMn(0.3%) samples, and Figure 6.10 for Nb/CuMn(2.2%) multilayers. In Nb/Cu multilayers, however, $H_{c2\perp}$ displays a strong positive curvature near T_c. This behavior (Figures 6.11 and 6.12) held for all Nb/Cu multilayers studied and was more noticeable in samples having thick Nb or Cu layers. A close inspection of the data for Nb/CuMn(0.3%) and Nb/CuMn(2.2%) multilayers reveals that very near T_c, these curves also show positive curvature. Nb/CuGe(5%) multilayers are the only samples which show no signs of positive curvature.

The remainder of this section will focus on how $H_{c2\perp}$ varies as d_n, d_s, y, and ℓ_n are varied. The existence of positive curvature will be discussed first, then the discussion of the dependence on d_n will follow, and finally, the dependence on d_s will be discussed.

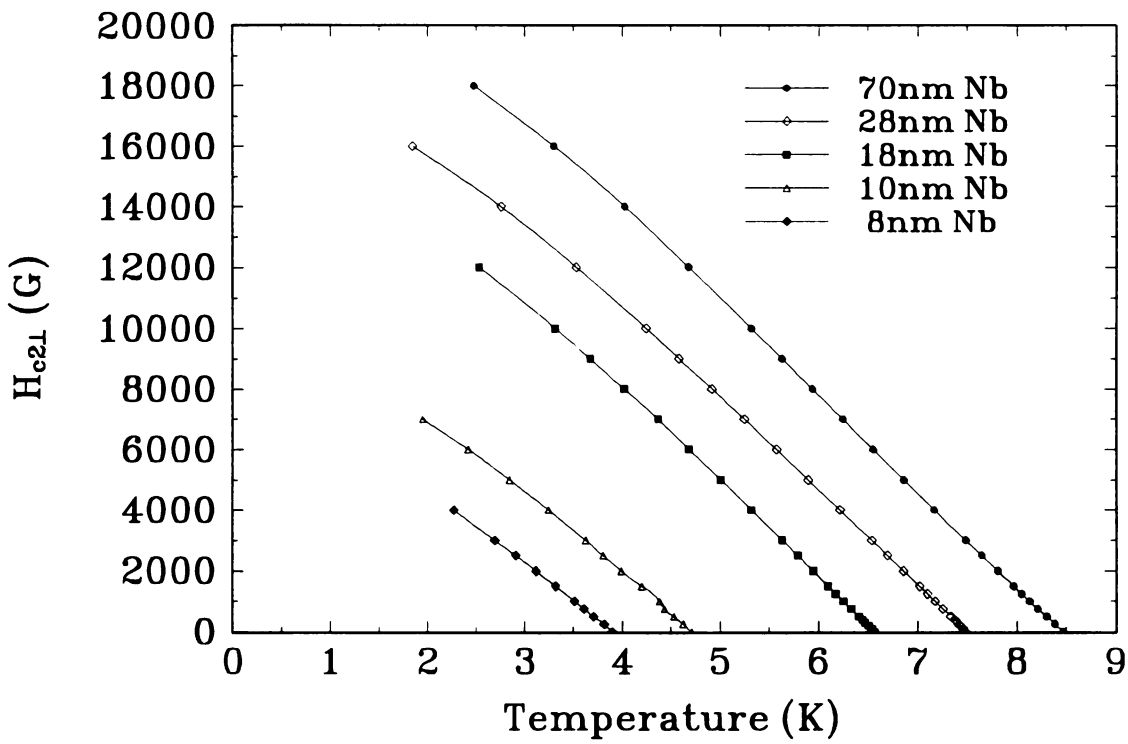

Figure 6.6: $H_{c2\perp}(T)$ for Nb/CuGe(5%) multilayers with d_n = 20 nm.

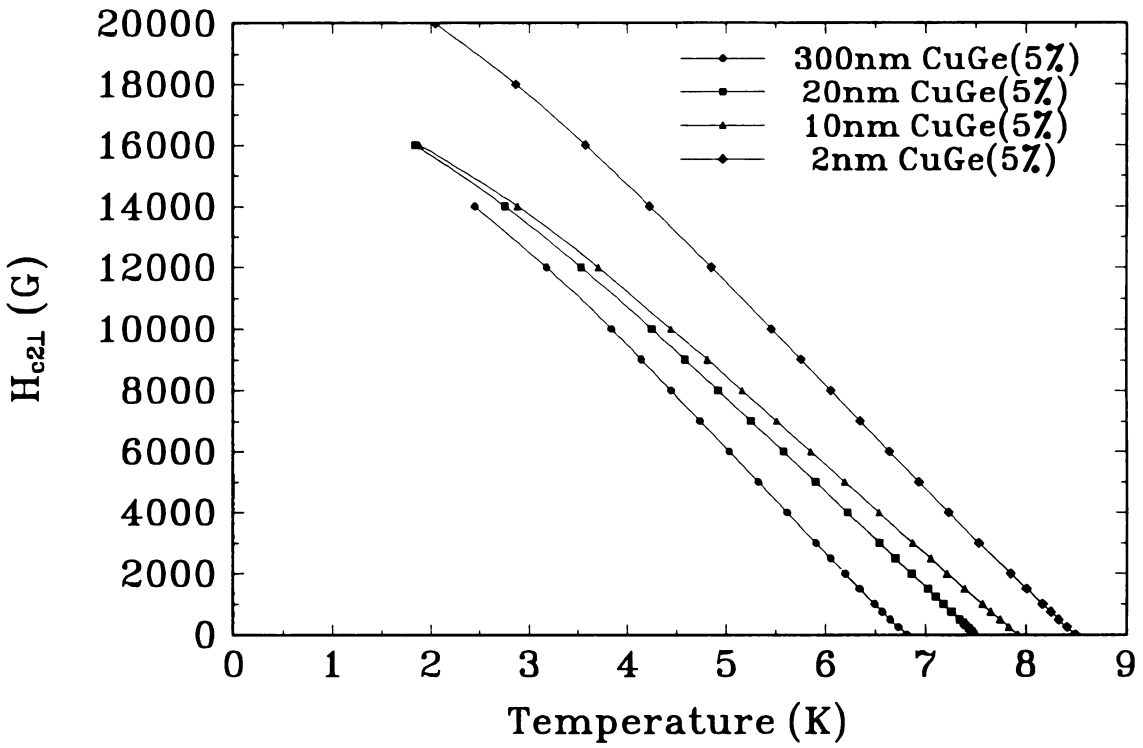

Figure 6.7: $H_{c2\perp}(T)$ for Nb/CuGe(5%) multilayers with d_s = 28 nm.

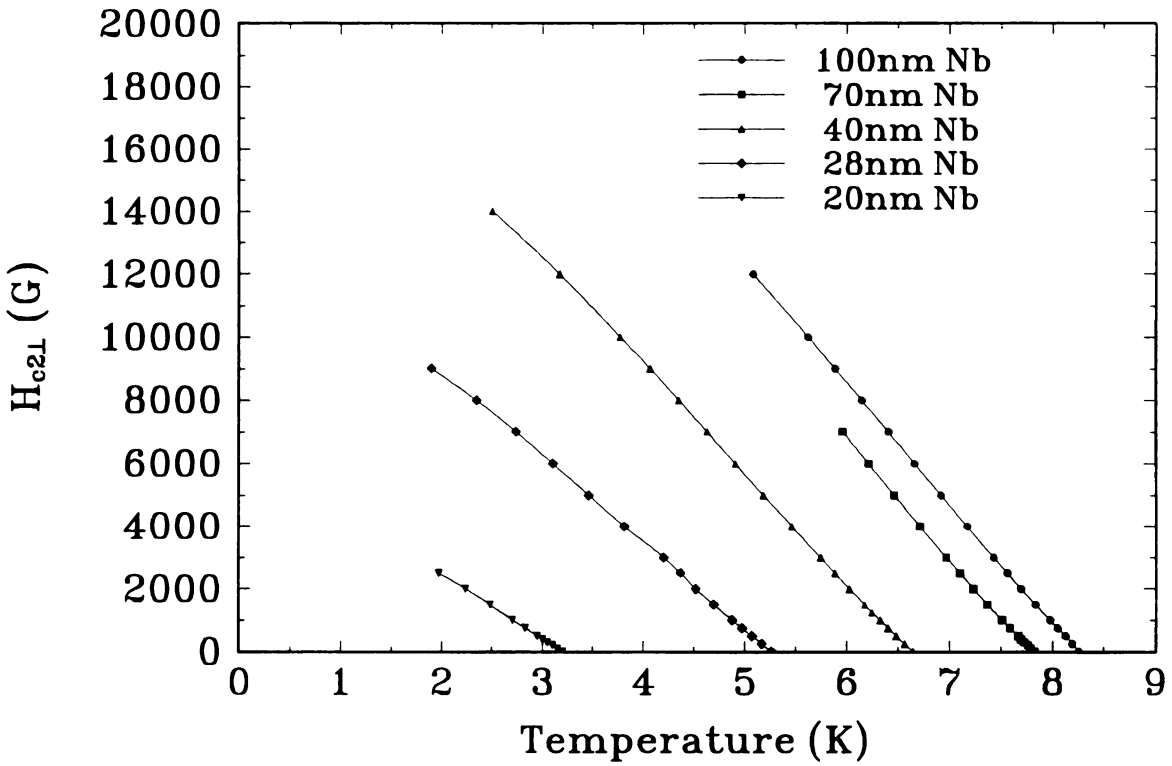

Figure 6.8: $H_{c2\perp}(T)$ for Nb/CuMn(0.3%) multilayers having d_n = 20 nm.

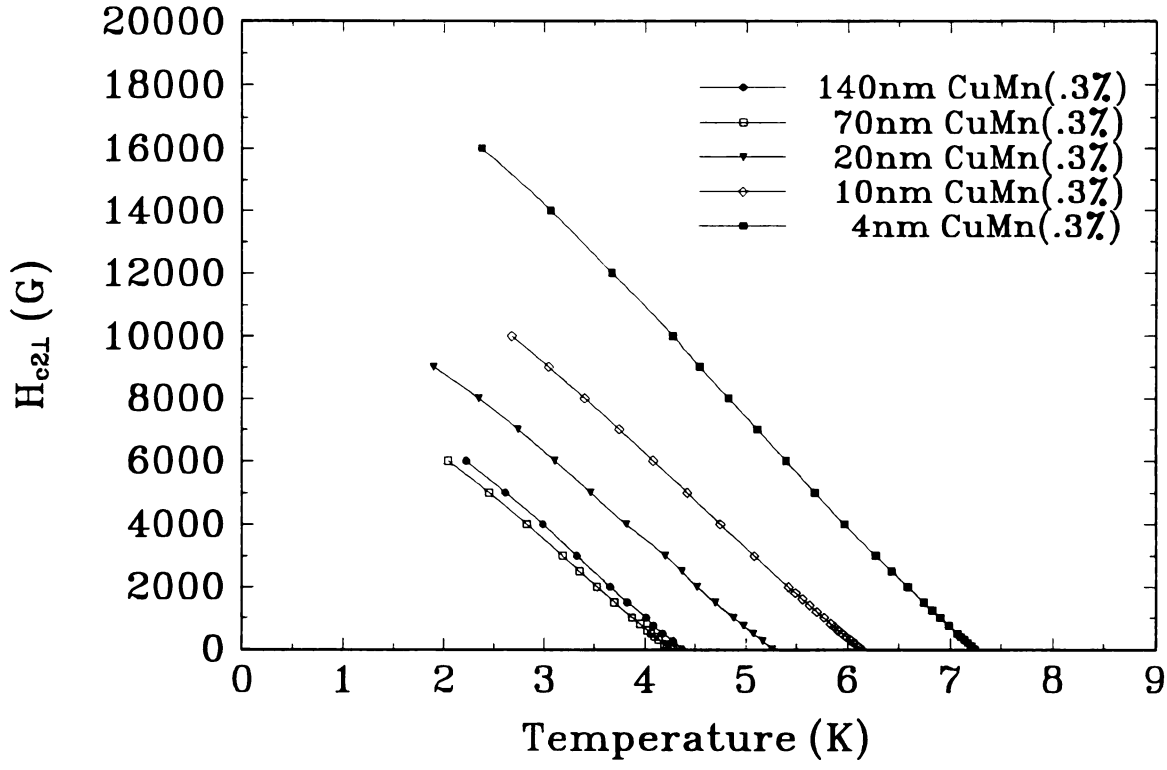

Figure 6.9: $H_{c2\perp}(T)$ for Nb/CuMn(0.3%) multilayers with d_s = 28 nm.

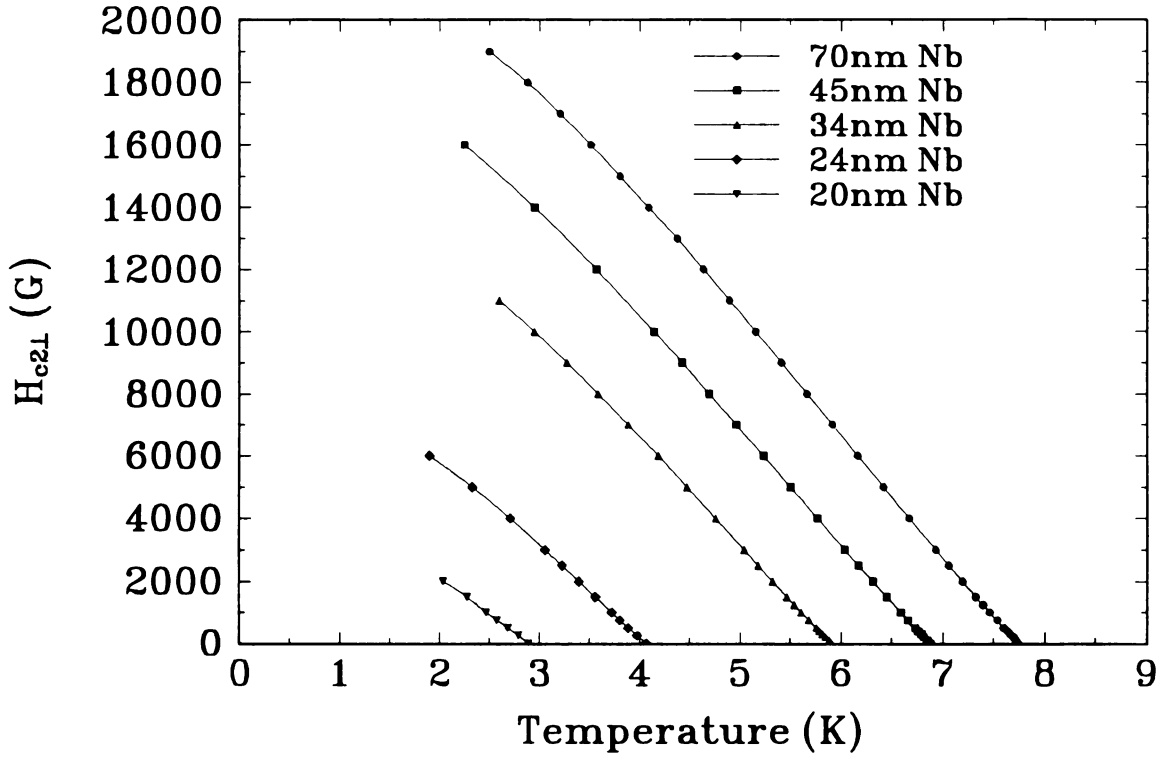

Figure 6.10: $H_{c2\perp}(T)$ for Nb/CuMn(2.2%) multilayers with d_n = 6.0 nm.

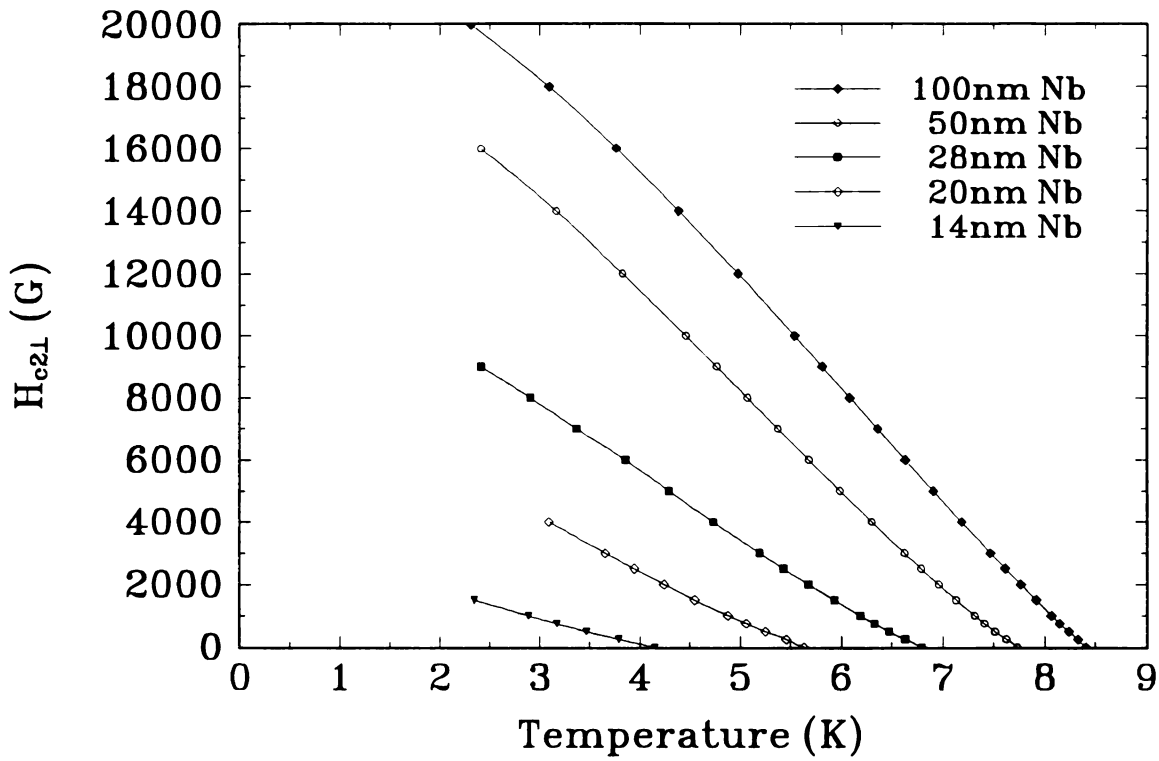

Figure 6.11: $H_{c2\perp}(T)$ for Nb/Cu multilayers with d_n = 40 nm.

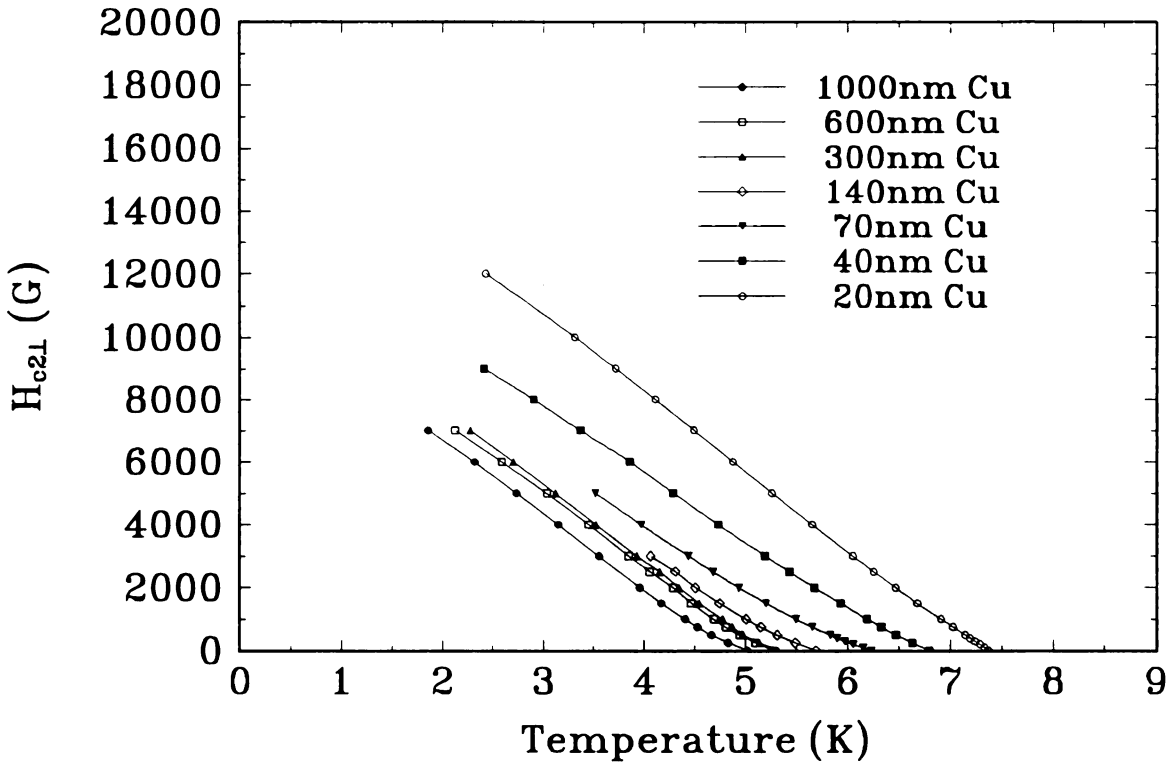

Figure 6.12: $H_{c2\perp}(T)$ for Nb/Cu multilayers with d_s = 28 nm.

6.2.1.1 Positive Curvature

For the purposes of analyses, the curvature of $H_{c2\perp}(T)$ was defined as the second derivative of $H_{c2\perp}$ with respect to T ($H_\perp$"). The measured data were not accurate enough for a direct determination of $H_\perp$", therefore the first derivative of $H_{c2\perp}$ ($H_\perp$') was extracted from the data sets and $H_\perp$" was defined as the slope of these data sets. $H_\perp$' was determined by doing a three point fit of $H_{c2\perp}$ to a second order polynomial, and then taking the first derivative of the fit as shown in Figure 6.13. $H_\perp$' was then defined as the slope of this fit at the desired temperature. The resulting values for $H_\perp'(T)$ for the Nb/Cu series are shown in Figures 6.14 and 6.15.

Four general trends were observed for the curvature as T, d_n, d_s, y, and ℓ_n were varied:

First, $H_\perp$"(T) increased as T increased toward T_c, reaching a maximum at $T = T_c$. This behavior was observed to occur in all samples showing signs of positive curvature. In most data sets there appears a sharp negative curvature right at T_c. While this feature shows up in many data sets it is typically contained within the expected uncertainty of the data, and therefore, is not significant.

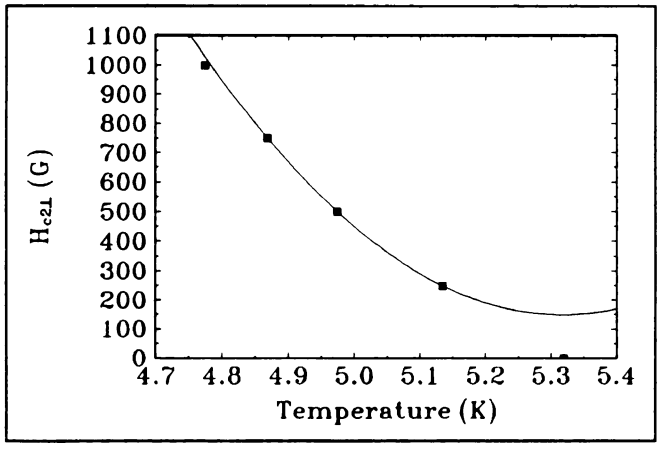

Figure 6.13: $H_{c2\perp}(T)$ fit used to extract $H_\perp'(T)$.

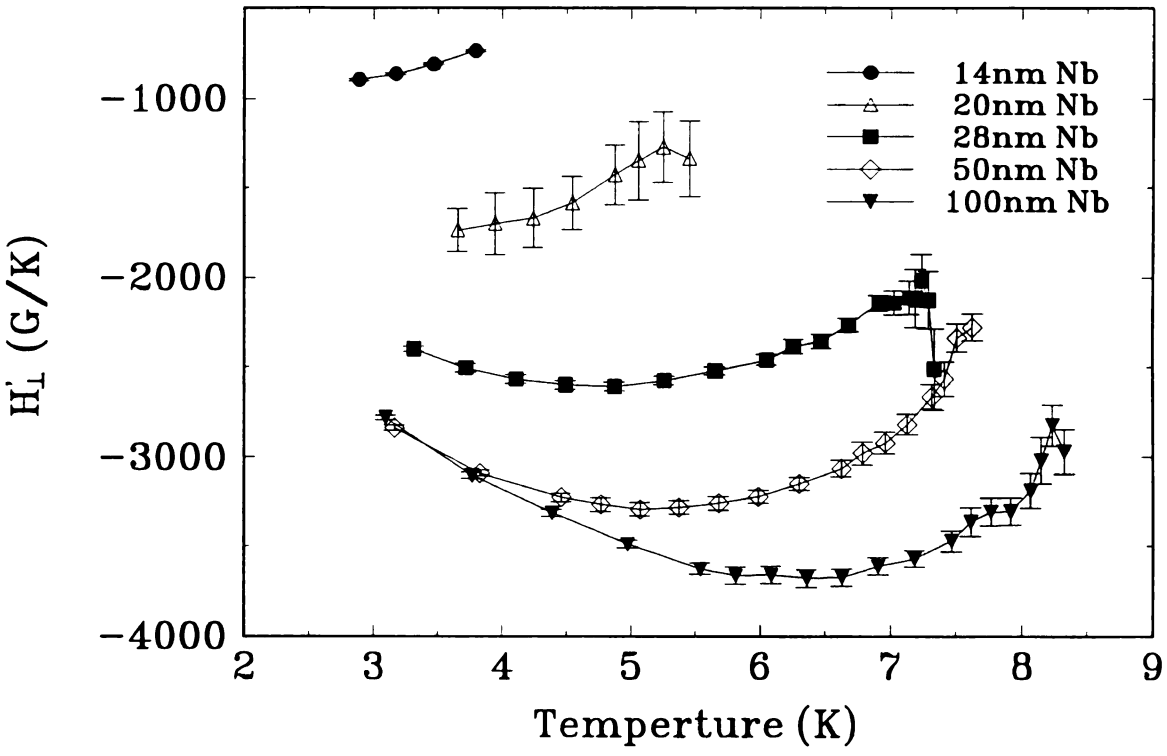

Figure 6.14: $H_{\perp}'(T)$ for Nb/Cu multilayers with d_n = 40 nm. $H_{\perp}''$ is defined as the slope of these data.

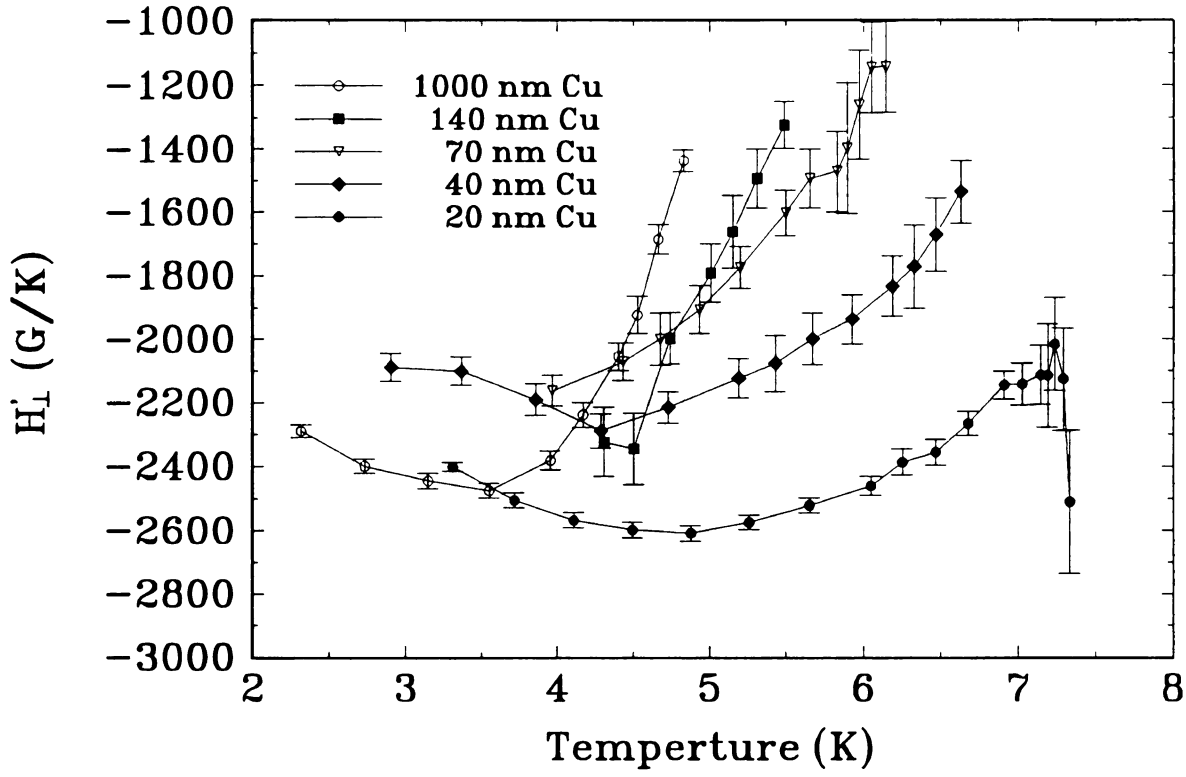

Figure 6.15: $H_{\perp}'(T)$ for Nb/Cu multilayers with d_s = 28 nm. H" is defined as the slope of these data.

Second, $H_{\perp}''(T_c)$ increased as d_n increased in Nb/Cu and Nb/CuMn(0.3%) multi-layers. Note that in Figure 6.15 the slopes of $H_{\perp}'$ are nearly equal for d_n = 140 nm and 1000 nm. This implies that the curvature saturated to a large value when d_n became larger than d_{nc}^*, the length scale needed to decouple the S layers. Curvature, therefore, decreased as the coupling strength between S layer increased.

Third, $H_{\perp}''(T_c)$ increased as d_s increased. This trend was clear in the Nb/Cu data (Figure 6.14) and Nb/CuMn(0.3%) data, but may not occur in the Nb/CuMn(2.2%) samples. As d_s increases, the pair density in S should increases toward its bulk value.

Fourth, $H_{\perp}''(T_c)$ was large for Nb/Cu samples, smaller for Nb/CuMn(0.3%) and Nb/CuMn(2.2%) samples, and zero for Nb/CuGe(5%) samples. d_{nc}^* for CuMn(0.3%) and CuGe(5%) interlayers are nearly equal, however, CuMn shows strong positive curvature while CuGe does not.

These data indicate that an odd paradox appears when analyzing the curvature. Curvature increases in magnitude as the layers become more decoupled by increased d_n, but, curvature decreases as the layer become more decoupled by increasing ℓ_n. In addition, curvature is not simply related to the pair penetration depth in N, since CuMn(0.3%) and CuGe(5%) layers have the same d_{nc}^*, but CuMn(0.3%) samples show curvature while CuGe(5%) samples do not. Takahashi and Tachiki predict curvature to depend on how strongly the superconductivity is localized within the S layers, but they provide no physical mechanism for the occurence of curvature.[28] Another proximity effect model,[27] which is slightly more tractable than the model of Takahashi and Tachiki will be discussed in the theory section.

6.2.1.2 The Dependence of $H_{c2\perp}$ on d_n

To systematize the data sets for $H_{c2\perp}(T)$ for the various N layer materials and S and N layer thicknesses, it has been evaluated for each sample at T = $0.5T_c$. This

temperature is low enough to be below any region of positive curvature. Therefore, the behavior of $H_{c2\perp}(0.5)$ should characterize the entire data set. $H_{c2\perp}$ at T = 0 was not used to systematize the data sets because $H_{c2\perp}$ could not be reliably extrapolated to zero temperature for all data sets.

The dependence of $H_{c2\perp}(0.5)$ on d_n for d_s = 28 nm is shown in Figure 6.16. $H_{c2\perp}$ was observed to decrease with increasing d_n and to become independent of d_n for $d_n > d^*_{n\perp}$. The estimated values for $d^*_{n\perp}$, however, were much smaller that the d^*_{nc} estimated from the T_c experiments. Approximate values for both d^*_{nc} and $d^*_{n\perp}$ are listed in Table 6.1. The difference in these lengths was not due to sample variability since the same samples were used for both the T_c and the $H_{c2\perp}(T)$ studies.

The difference between $d^*_{n\perp}$ and d^*_{nc} appears to be related to changes in the inherent spin-scattering rate of N. d^*_{nc} is approximately equal for Nb/CuMn(0.3%) and Nb/CuGe(5%) samples whereas, $d^*_{n\perp}$ for these two systems appear to be different. However, the data are not precise enough to determine why $d^*_{n\perp}$ and d^*_{nc} are different.

Table 6.1: d^*_{nc} and $d^*_{n\perp}$ for various CuX materials

CuX	d^*_{nc} / nm	$d^*_{n\perp}$ / nm
Cu	300	70
CuGe(5%)	100	10
CuMn(0.3%)	70	70

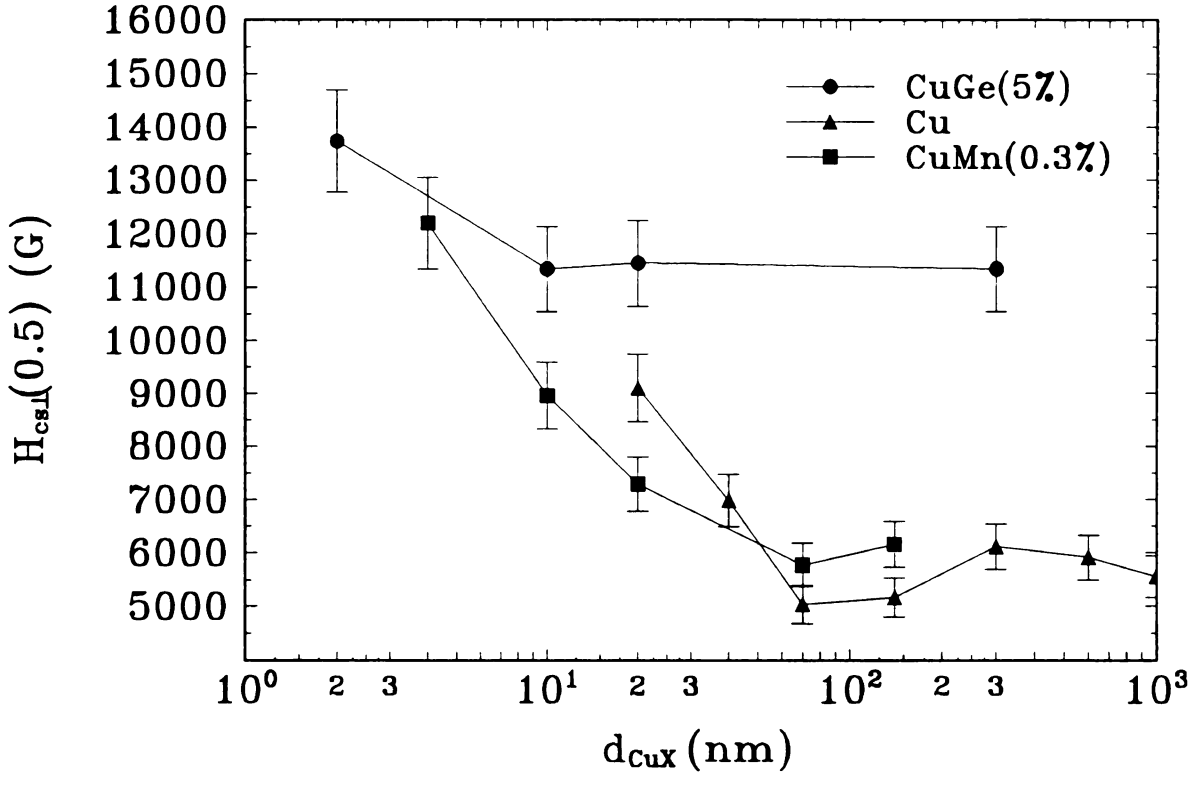

Figure 6.16: $H_{c2\perp}(0.5)$ for d_s = 28 nm and various CuX materials and layer thicknesses.

6.2.1.3 The Dependence of $H_{c2\perp}$ on d_s

Figure 6.17 shows the data for $H_{c2\perp}(0.5)$ as a function of Nb layer thickness. These curves appear very similar to the raw data for T_c as a function of Nb layer thickness (Figure (5.5)). Based on this similarity, one can postulate that $H_{c2\perp}$ may scale as

$$h_\perp = \frac{H_{c2}^b - H_{c2\perp}}{H_{c2}^b} \approx \left(\frac{d_s}{d_o}\right)^{-w} \qquad (6.12)$$

and w is a scaling exponent. In addition, $H_{c2\perp}(T=0)$ should go to zero only when T_c goes to zero, therefore, the scale factor d_o used above should be the same as that used for the scaling of T_c. $h_\perp$ is plotted in Figure 6.18 as a function of d_s for the same data as shown in Figure 6.17. The scatter is too large to definitively state whether or not scaling works.

Studies by Kanoda et al.[25] on V/Ag multilayers show that $H_{c2\perp}(0)$ is described by

$$H_{c2\perp}(0) \cong H_{c2}^b(0)\left(1+\varepsilon\frac{d_n}{d_s}\right)^{-1} \qquad (6.13)$$

where $\varepsilon \cong 0.2\,\ell_n/\ell_s$. In the limit that $\varepsilon d_n << d_s$, this form is equivalent to Equation (6.12). Hence, scaling of $H_{c2\perp}$ does exist for V/Ag samples.

While these results for the dependence of $H_{c2\perp}(0.5)$ on d_n, d_s, and N are in qualitative agreement with the T_c results, better data are needed to prove the existence of scaling in Nb/CuX multilayers. A better understanding of the positive curvature, however, requires a good theoretical model.

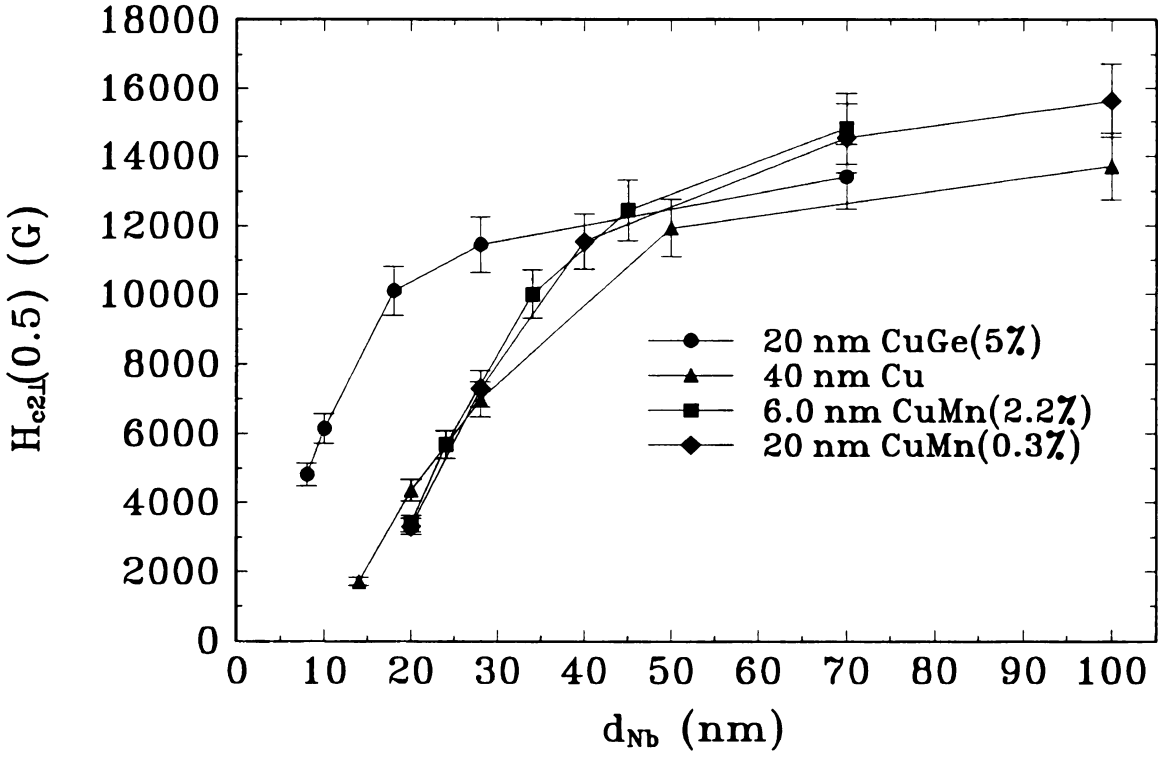

Figure 6.17: Dependence of $H_{c2\perp}(0.5)$ on d_s for various d_n and CuX.

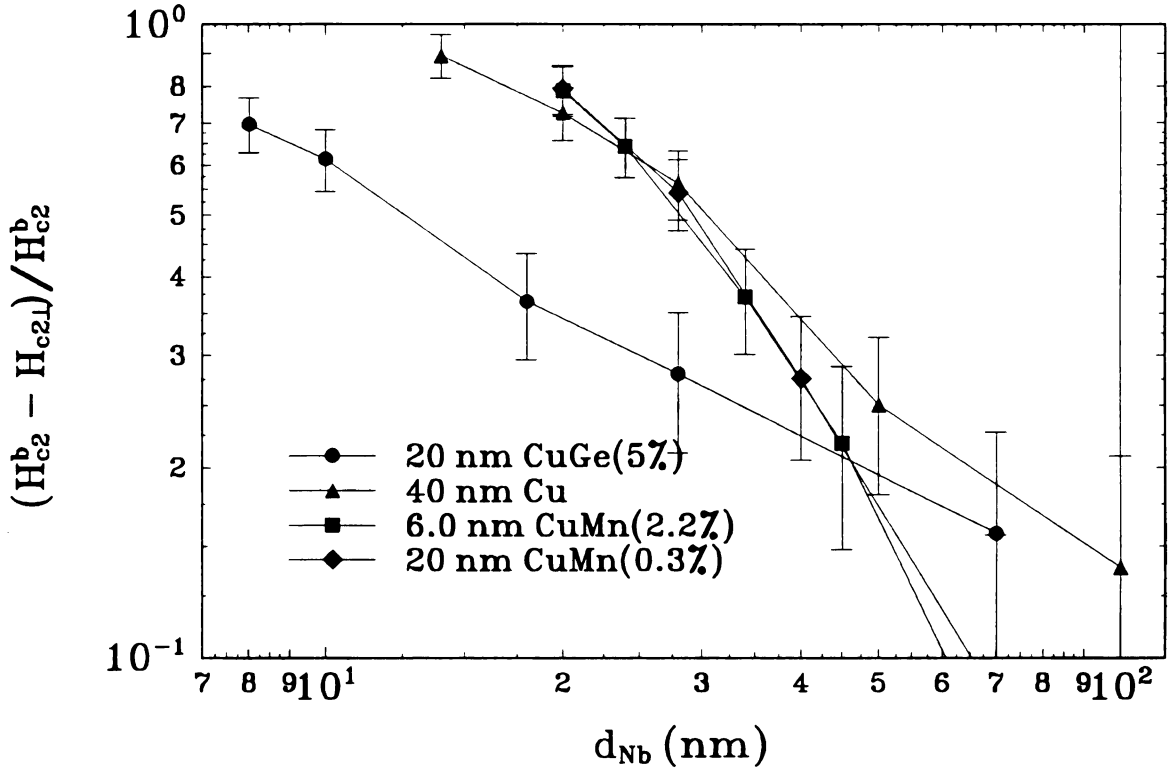

Figure 6.18: Dependence of $h_\perp(0.5)$ on d_s for various d_n and CuX.

6.2.3 $H_{c2\perp}(T)$ Theory

In a series of publications, V. Kogan and various collaborators have developed a model for superconductivity in S/N multilayers.[27,51,57,58] Of particular interest in this series is the paper by Biagi, Kogan and Clem (BKC)[27] where a model predicting the behavior of $H_{c2\perp}(T)$ in S/N multilayers was presented. One advantage of this model over previous models is that it places no limits on the values of the S and N layer thicknesses or on the electron mean-free-paths. Therefore the BKC model does not assume the dirty superconducting limit and hence unlike the earlier HTW and KZ models, it should be generally valid for Nb/Cu as well as Nb/CuGe(5%) multilayers. One serious drawback to the model is that it does not include magnetic scattering in the N layer, and so, cannot directly be applied to multilayers having CuMn layers.

With these stipulations, BKC formulated the following set of equations to predict the temperature dependence of $H_{c2\perp}$. For simplicity in the following discussions $H_{c2\perp}(T)$ has been replaced by $H_\perp$.

$$q_s \tan(q_s d_s / 2) = q_n \frac{\rho_s}{\rho_n} \tanh(q_n d_n / 2) \tag{6.14}$$

$$q_s^2 = k_s^2 - 2\pi \frac{H_\perp}{\Phi_o} \tag{6.15}$$

$$\ln\left(\frac{T}{T_c^b}\right) = \Psi(1/2) - \Psi\left(1/2 + k_s^2 \eta_s^2 / 2\right) \tag{6.16}$$

$$q_n^2 = \begin{cases} k_n^2 + 2\pi \dfrac{H_\perp}{\Phi_o} & \ell_n << \xi_n^o \\ k_n^2 \beta_n^2 + 2\pi \dfrac{H_\perp}{\Phi_o} - \dfrac{3}{5}\left[\dfrac{2\pi H_\perp}{\Phi_o} \dfrac{\ell_n}{\beta_n}\right] & \ell_n \le \xi_n^o \end{cases} \tag{6.17}$$

$$k_n^2 = \begin{cases} \dfrac{1}{\eta_n^2} & \ell_n << \xi_n^o \\ \dfrac{1}{\eta_n^2}\beta_n\left[1-\dfrac{H_\perp}{H_o}\right]^2 & \ell_n \le \xi_n^o \end{cases} \tag{6.18}$$

where,

$$\beta_n = 1 - 1/\lambda_n \tag{6.19}$$

$$\lambda_n = 3(\eta_n/\ell_n)^2 \tag{6.20}$$

$$H_o = \frac{\Phi_o}{2\pi}\frac{\beta_n^2}{\ell_n^2}\left(\frac{5}{\lambda_n}\right)^{1/2} \tag{6.21}$$

$$\eta_i^2 = \frac{\hbar v_{f,i}\ell_i}{6\pi k_b T} \cong \frac{\pi\hbar k_b}{6e^2 T}\frac{1}{\gamma_i\rho_i} \tag{6.22}$$

$$\xi_n^o = \frac{\hbar v_{f,n}}{2\pi k_b T_c^b} \cong \frac{\pi\hbar k_b}{2e^2 T_c^b}\frac{1}{\gamma_n(\rho\ell)_n} \tag{6.23}$$

and $\Psi(z)$ is the digamma function, $\hbar$ is Plank's constant divided by 2π, Φ_o is the flux quantum, k_b is Boltzmann's constant, e is the electron charge, $v_{f,i}$ is the Fermi velocity, ℓ_i is the electron mean free path, γ_i is the linear coefficient of the low temperature specific heat, ρ_i is the resistivity, i stands for the S or N material, $(\rho\ell)_n$ is the finite size correction to the resistivity in N, T_c^b is the bulk superconducting transition temperature of S, and ξ_n^o is the effective superconducting coherence length in N.

In the limit that $H_\perp = 0$ and $\ell_n << \xi_n^o$, these equations simplify exactly to the model derived by Hauser, Theuerer, and Werthamer [Equations (5.29) through (5.31)]. Since it was already shown that the HTW model does not quantitatively predict T_c, one may not

expect the BKC model to quantitatively predict $H_\perp$. Hence, only the general trends observed in the BKC model will be compared to the data. This model will first be examined in the limit of small d_n, and following this, the full model will be used to study the phenomena of positive curvature of $H_\perp$.

In the limit that d_n is small, $\tanh(q_n d_n/2) \cong q_n d_n/2 << 1$ and therefore, $\tan(q_s d_s/2) \cong q_s d_s/2 << 1$ also. Hence, Equation (6.14) can be simplified to

$$q_s^2 d_s \cong q_n^2 d_n \frac{\rho_s}{\rho_n} \tag{6.24}$$

This is then used to solve for q_s^2 and hence k_s^2:

$$k_s^2 \cong q_n^2 \frac{\rho_s}{\rho_n}\frac{d_n}{d_s} + \frac{2\pi H_\perp}{\Phi_o} \tag{6.25}$$

Approximating the right hand side of Equation (6.16) by[47]

$$\Psi(1/2+z/2) - \Psi(1/2) \cong \ln\left(1+\frac{\pi^2}{4}z\right) \tag{6.26}$$

and combining this with Equation (6.25) leads to the following equation for $H_\perp$:

$$\frac{T_c^b}{T} \cong 1 + \frac{\pi^2}{4} k_s^2 \eta_s^2 \tag{6.27}$$

Now, allowing the dirty limit to be applicable, as it should be for very thin N layers (see Chapter 5) Equation (6.27) becomes

$$\frac{T_c^b}{T} \cong 1+\frac{\pi^2}{4}\frac{2\pi\eta_{so}^2}{\Phi_o}H_\perp \frac{T_c^b}{T}\left[1+\frac{\rho_s}{\rho_n}\frac{d_n}{d_s}\right]+\frac{\pi^2}{4}\left(\frac{\eta_s}{\eta_n}\right)^2\frac{\rho_s}{\rho_n}\frac{d_n}{d_s} \tag{6.28}$$

where, $\eta_{so} = \eta_s\left(T_c^b\right)$. In addition, note that

$$\left(\frac{\eta_s}{\eta_n}\right)^2 \cong \frac{\gamma_n\rho_n}{\gamma_s\rho_s} \tag{6.29}$$

Therefore, the final equation relating T and $H_\perp$ in the limit that d_n is small is

$$T\left[1+\frac{\pi^2}{4}\frac{\gamma_n}{\gamma_s}\frac{d_n}{d_s}\right] \cong T_c^b\left[1-\frac{\pi^2}{4}\frac{2\pi\eta_{so}^2}{\Phi_o}H_\perp\left(1+\frac{\rho_s}{\rho_n}\frac{d_n}{d_s}\right)\right] \tag{6.30}$$

The primary difficulty in applying this equation is that it solves for T as a function of $H_\perp$ and T_c^b whereas most experiments examine how $H_\perp$ depends on $(T_c\text{-}T)$.

Note that when $T = T_c$, $H_\perp = 0$, and Equation (6.29) collapses to the thin d_n limit of the HTW model

$$T_c^b \cong T_c\left(1+\frac{\pi^2}{4}\frac{\gamma_n}{\gamma_s}\frac{d_n}{d_s}\right) \tag{6.31}$$

Using this to replace T_c^b with T_c in Equation (6.30) and reorganizing the terms, one finds:

$$H_{c2\perp}(T) \cong \frac{\Phi_o}{2\pi\eta_{so}^2}\frac{4}{\pi^2}\left(1-\frac{\rho_s}{\rho_n}\frac{d_n}{d_s}\right)\left(\frac{T_c-T}{T_c}\right) \tag{6.32}$$

In addition, in the limit that $d_s \to \infty$, $H_\perp \cong H_{c2}^b(T)$, or,

$$H_{c2}^{b}(T) \cong \frac{\Phi_o}{2\pi\eta_{so}^2}\frac{4}{\pi^2}\left(\frac{T_c^b - T}{T_c^b}\right) \tag{6.33}$$

This was then used to remove the explicit temperature dependence from Equation (6.32) resulting in

$$h_{\perp} = \frac{H_{c2}^{b} - H_{c2\perp}}{H_{c2}^{b}} \cong \frac{\rho_s}{\rho_n} d_n d_s^{-1} \tag{6.34}$$

for all temperatures below T_c. This form is in general agreement with Equation (6.12), with the data sets for $h_{\perp}$ as a function of d_s, and with the experimental results of Kanoda et al.[25] To accurately test the validity of $H_{c2\perp}$ scaling, however, requires data for sample series having much smaller N layer thicknesses than have been measured.

Analyzing the full numerical solutions to Equations 6.14-6.23, BKC were able to show that for large d_n and large d_s, $H_{\perp}$ displays positive curvature near T_c. In particular, BKC found that as either d_n or d_s increase $H_{\perp}"(T_c)$ increases, eventually passing through a maximum. These trends are qualitatively shown in Figure 6.19. In the limit of infinite d_s, $H_{\perp}"(T_c)$ tends toward zero while for large d_n, $H_{\perp}"(T_c)$ remains non-zero.

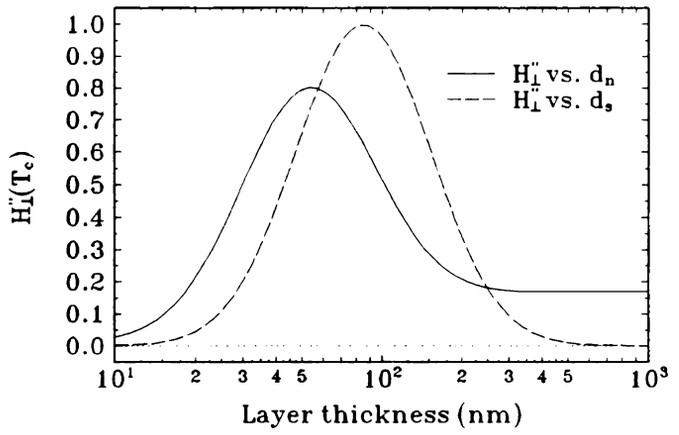

Figure 6.19: Sketch showing the dependence of $H_\perp''(T_c)$ on d_s and d_n.

These trends agree well with the behavior observed in Nb/Cu multilayers, however, the maximum in $H_\perp''$ was not observed. This may indicate that samples having sufficiently large d_n or d_s have not been studied, or that this feature of the theory does not apply to our data.

The BKC model also predicts that $H_\perp''(T_c)$ should increase as ℓ_n increases, as ℓ_s decreases and is greatest when $\ell_s << \ell_n$. This also agrees with the data where $H_\perp''$ decreased systematically as the normal state resistivity of N was increased.

At the level of accuracy which the data allow, comparisons of the BKC model to the experimental results indicate that both experiment and theory agree on how $H_{c2\perp}$ and $H_\perp''$ depend on T, although they disagree on the behavior of $H_\perp''$ in the limit of thick N and S. The model and the results of Kanoda et al. do support the scaling of $H_{c2\perp}$, however the accuracy of the Nb/CuX data are not high enough to test scaling.

6.3 The Parallel Upper Critical Field

6.3.1 $H_{c2\|}$ Experiments

As mentioned in the introduction to this chapter, and shown in Figure 6.5, the temperature dependence of $H_{c2\|}$ follows one of three trends:

$$T^* < T < T_c \qquad H_{c2\|} \propto (T_c - T) \tag{6.35}$$

$$T_{2D} < T < T^* \qquad H_{c2\|} \propto (T_c^* - T)^{\upsilon} \qquad \upsilon \cong 1/2 \tag{6.36}$$

$$T < T_{2D} \qquad H_{c2\|} \cong H_{c2}^b(T) \tag{6.37}$$

where T^* is the dimensional-crossover temperature, T_c^* is the effective T_c for the 2D regime, T_{2D} is the crossover temperature from 2D to bulk behavior, and $H_{c2}^b(T)$ is H_{c2} for bulk S. Since $H_{c2\|}(T)$ is proportional to $1/\xi_{xy}\xi_z$, the temperature dependence of these two coherence lengths in the same temperature regimes is given by:

$$\xi_{xy}(T) \cong \begin{cases} \xi_{xy}^{3D}(0)\left(\dfrac{T_c - T}{T_c}\right)^{-1/2} & T^* < T < T_c \\ \xi_{xy}^{2D}(0)\left(\dfrac{T_c^* - T}{T_c^*}\right)^{-1/2} & T_{2D} < T < T^* \\ \xi_s^b(0)\left(\dfrac{T_c^b - T}{T_c^b}\right)^{-1/2} & T < T_{2D} \end{cases}$$

$$\xi_z(T) \cong \begin{cases} \xi_z(0)\left(\dfrac{T_c - T}{T_c}\right)^{-1/2} & T^* < T < T_c \\ \xi^* & T_{2D} < T < T^* \\ \xi_s^b(0)\left(\dfrac{T_c^b - T}{T_c^b}\right)^{-1/2} & T < T_{2D} \end{cases}$$

In an ideal case, the behaviors for ξ_{xy} and ξ_z are shown in Figures 6.20 and 6.21, and the resulting $H_{c2\|}$ curve based on these simulated data is shown in Figure 6.22. Most samples studied having $d_n < d_{nc}^*$ do show evidence for a dimensional crossover near T_c, but only samples having $d_s > 30$ nm show the low temperature bulk behavior.

The data for $H_{c2\|}(T)$ in Nb/Cu multilayers are shown in Figures 6.23 and 6.24. The Nb/CuGe(5%) data are displayed in Figures 6.25, 6.26 and 6.27, and Figures 6.28 and 6.29 present it for Nb/CuMn(0.3%) multilayers, while Figure 6.30 shows the data for Nb/CuMn(2.2%) multilayers.

For large d_s, all S/N multilayers studied showed evidence of bulk behavior below T_{2D}. In Nb/Cu, Nb/CuMn(0.3%) and Nb/CuMn(2.2%) multilayers, bulk behavior was observed for all d_s greater than approximately 30 nm. Nb/CuGe(5%) multilayers, however, only displayed bulk behavior for d_s equal to 70 nm, as shown in Figure 6.26. The 2D superconducting state of the isolated Nb layers was more strongly affected by CuGe than by any other N material. The T_c experiments however, indicated that CuGe layers affected the superconductivity of the S layers the least of any of the interlayers (i.e. they lead to the highest T_c's). Hence, it was expected that bulk behavior would be observed at lower d_s for CuGe interlayers than for other interlayers. This trend is still not understood.

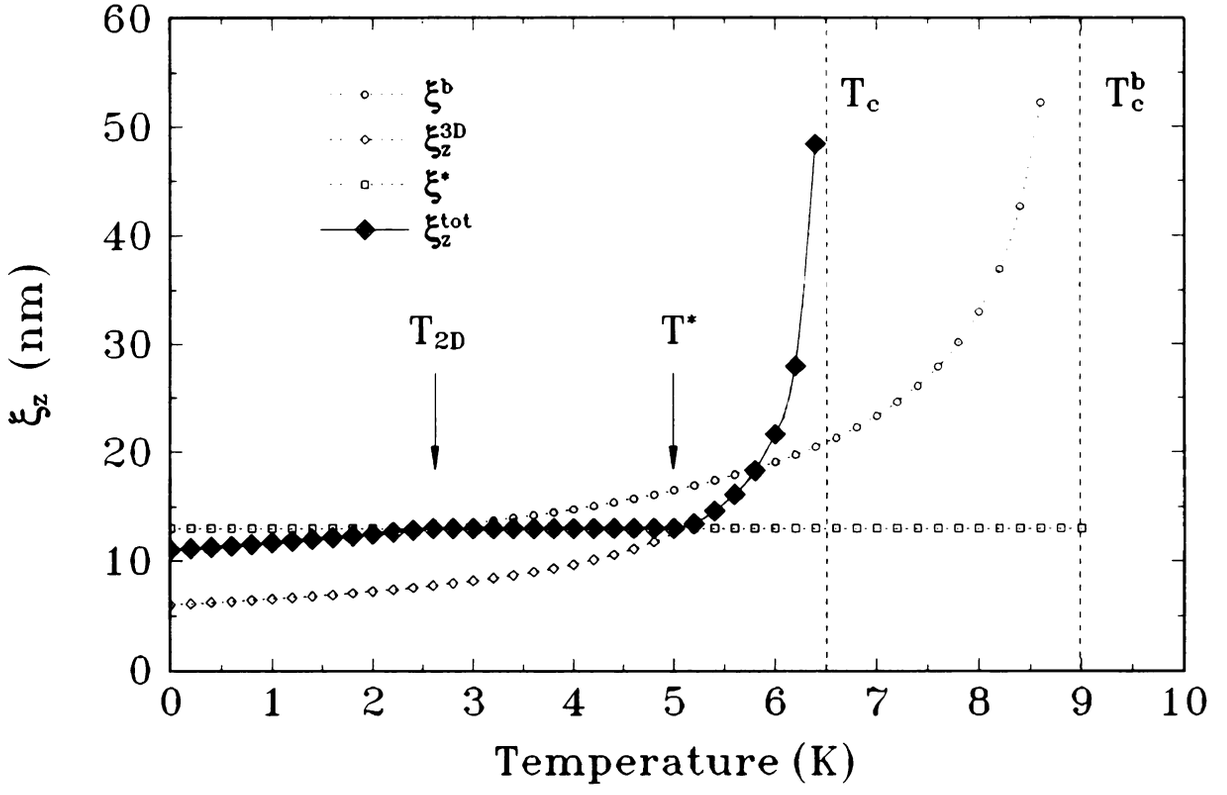

Figure 6.20: Qualitative dependence of $\xi_z(T)$ showing how T_{2D} and T^* are defined.

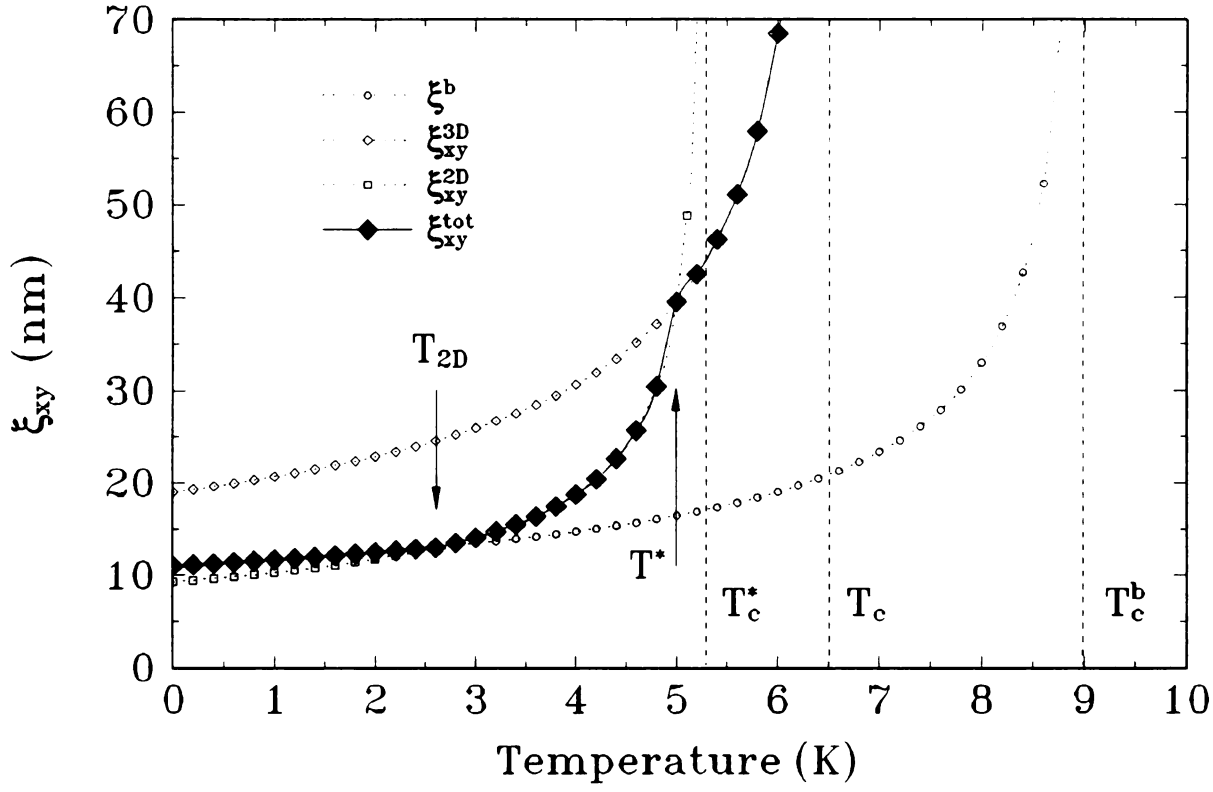

Figure 6.21: Qualitative dependence of $\xi_{xy}(T)$ showing how T_{2D}, T^*, and T_c^* are defined.

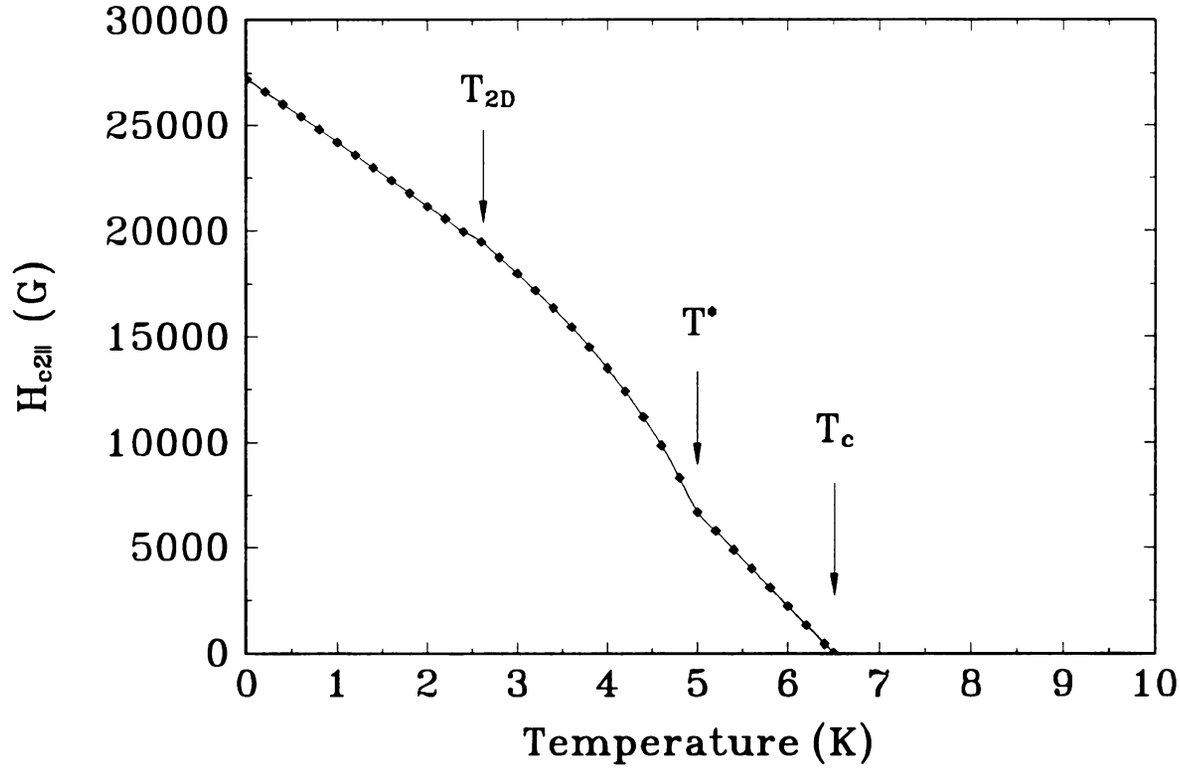

Figure 6.22: $H_{c2\|}(T)$ resulting from the $\xi_z(T)$ and $\xi_{xy}(T)$ data sets shown above.

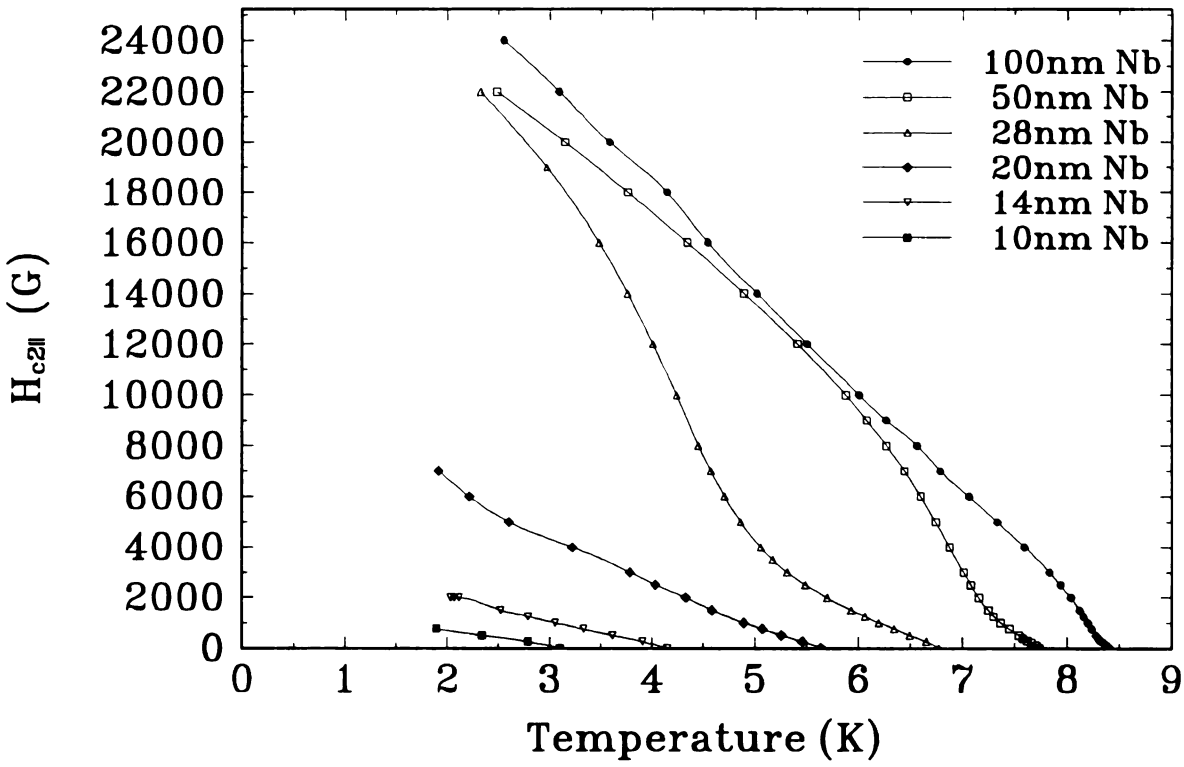

Figure 6.23: $H_{c2\|}(T)$ in Nb/Cu multilayers with d_n = 40 nm.

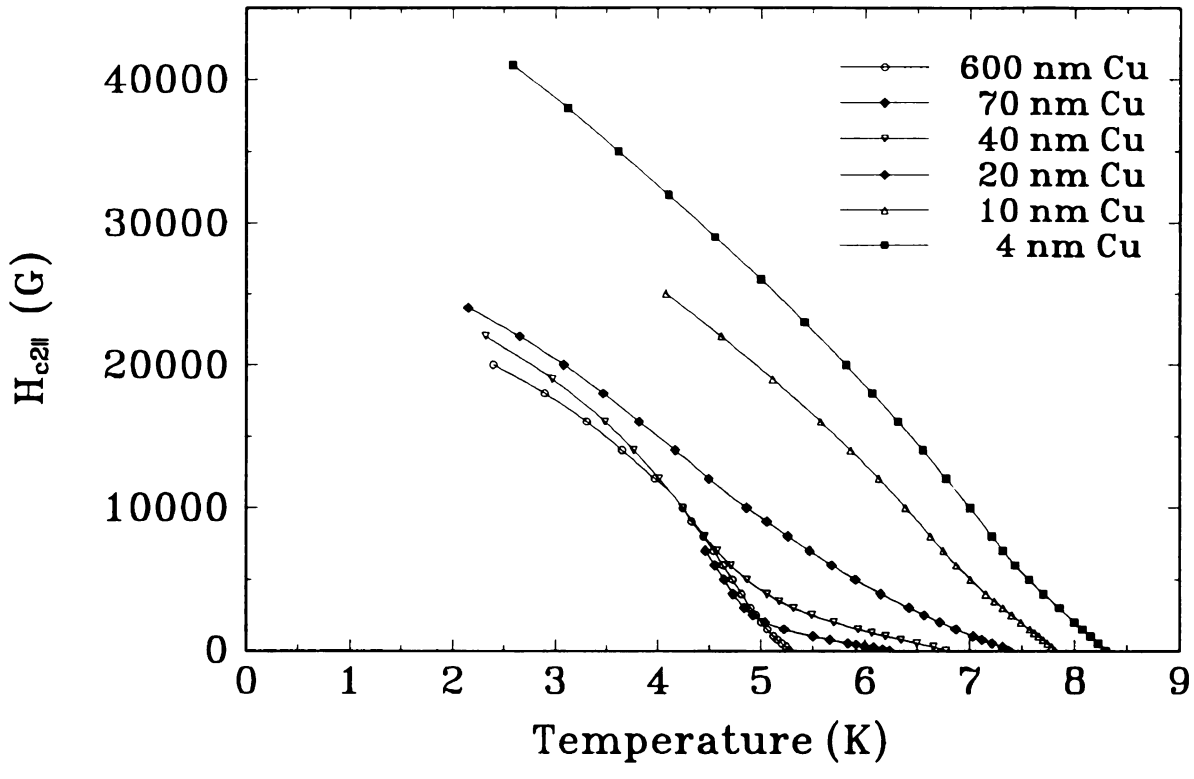

Figure 6.24: $H_{c2\|}(T)$ in Nb/Cu multilayers with d_s = 28 nm.

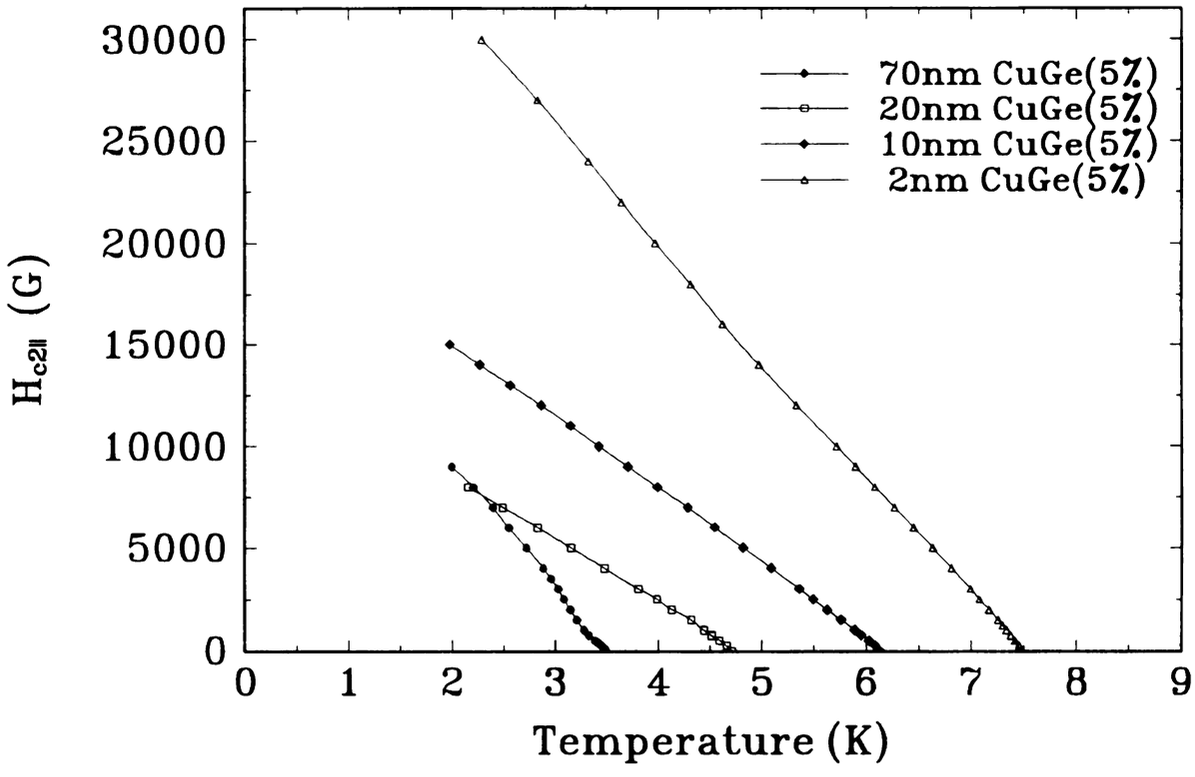

Figure 6.25: $H_{c2\parallel}(T)$ in Nb/CuGe(5%) multilayers with d_s = 10 nm.

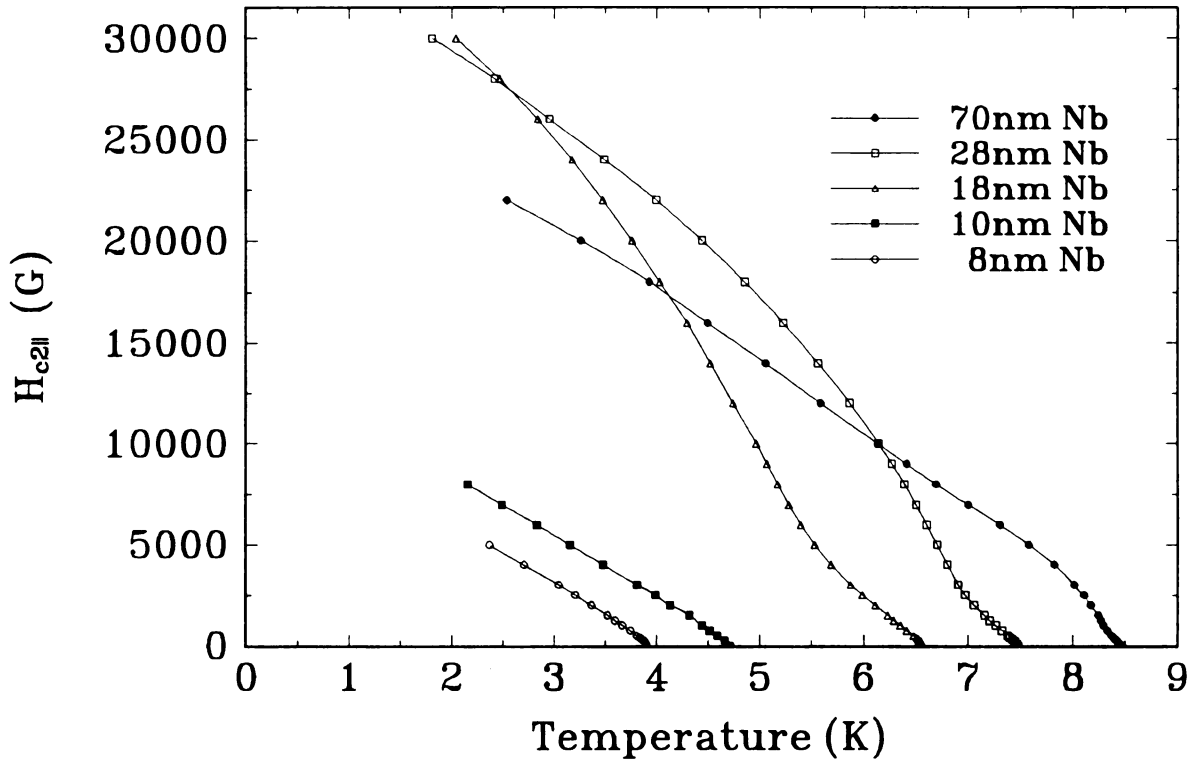

Figure 6.26: $H_{c2\|}(T)$ in Nb/CuGe(5%) multilayers with d_n = 20 nm.

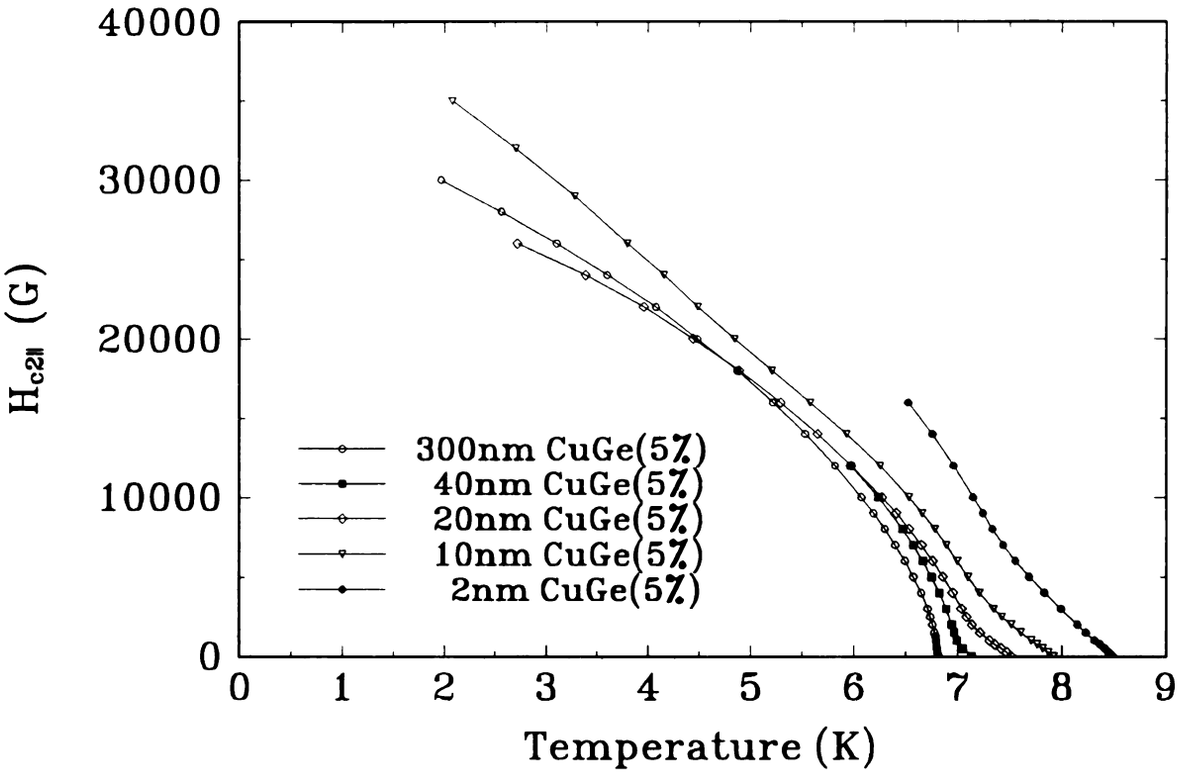

Figure 6.27: $H_{c2\parallel}(T)$ for Nb/CuGe(5%) multilayers with d_s = 28 nm.

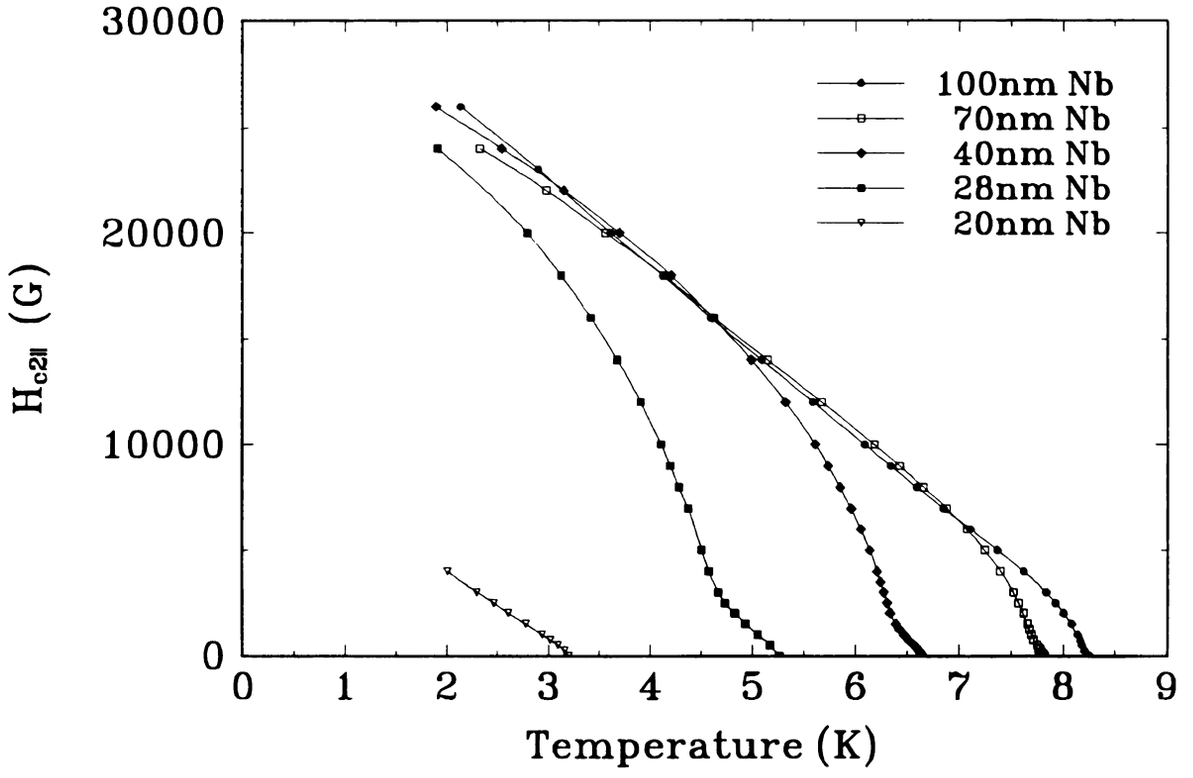

Figure 6.28: $H_{c2\|}(T)$ in Nb/CuMn(0.3%) multilayers with d_n = 20 nm.

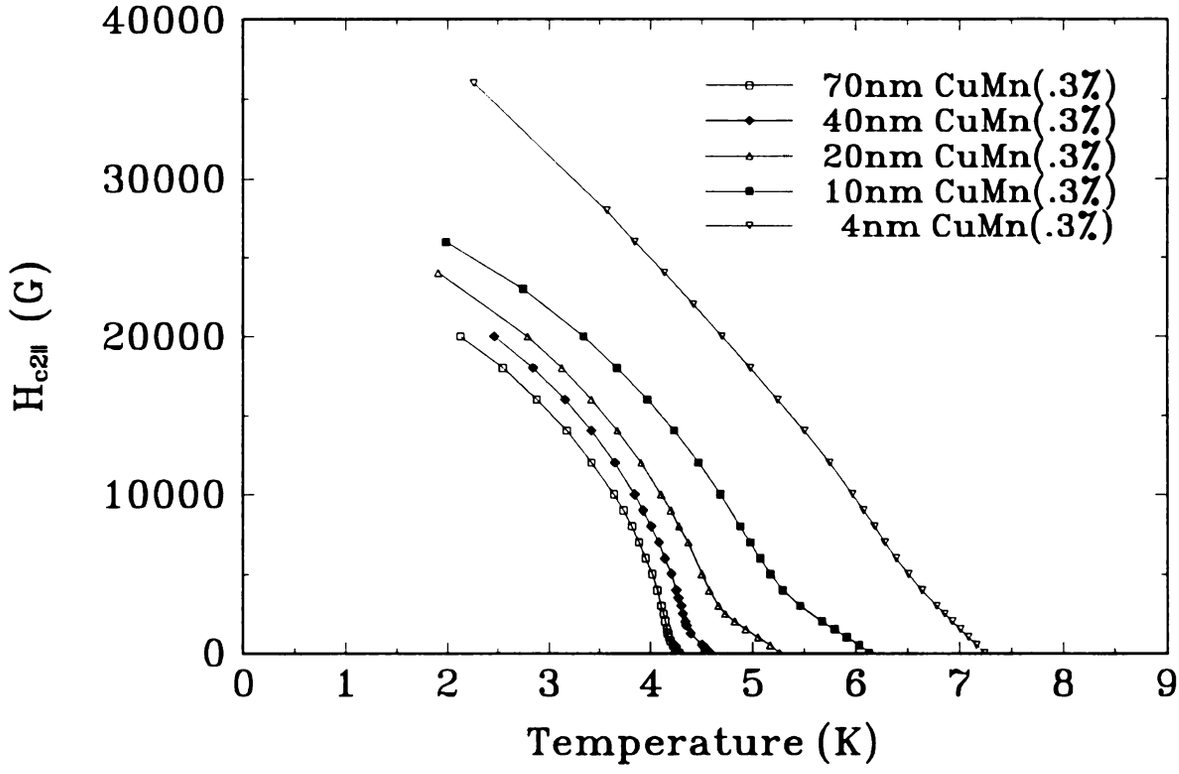

Figure 6.29: $H_{c2\|}(T)$ in Nb/CuMn(0.3%) multilayers with d_s = 28 nm.

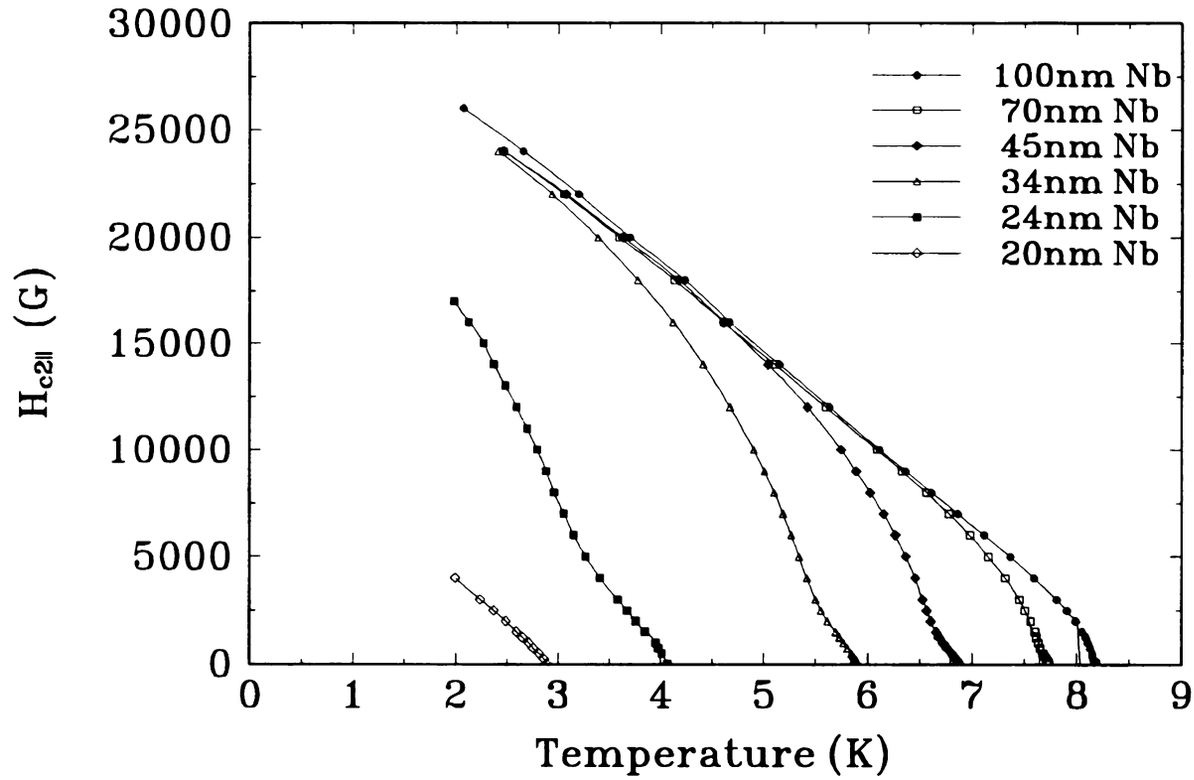

Figure 6.30: $H_{c2\|}(T)$ in Nb/CuMn(2.2%) multilayers with d_n =6.0 nm.

For d_s less than the above values, only the 3D-coupled and 2D-decoupled states were observed. Here, as d_s was reduced, the 3D regime expanded rapidly with T^* decreasing toward zero temperature much more rapidly than T_c. Hence, the 3D coupled state appears to dominate the superconductivity of multilayers having small d_s. This may indicate that for small d_s, there is a larger energy penalty for isolating the superconductivity within S than is found for larger d_s.

Figure 6.31 presents data for $H_{c2\|}(T)$ at various Nb layer thicknesses in Nb/Cu multilayers with d_n = 40 nm and Cu/Nb/Cu sandwiches with d_n = 300 nm. Dimensional crossover was observed to occur when $H_{c2\|}(T)$ for a multilayered sample became approximately equal to $H_{c2\|}(T)$ for a sandwich having the same Nb layer thickness. Below T^*, $H_{c2\|}(T)$ for the multilayer and sandwich samples did not coincide. This shift was related to a shift in T_c, since T_c in the sandwich films was observed to be slightly less than T_c observed in Nb/Cu multilayers having the same Cu layer thickness (300 nm). Therefore, this shift in $H_{c2\|}(T)$ was not related to dimensional crossover.

$H_{c2\|}(T)$ for the sandwiches also showed strong positive curvature near T_c. This trend was reminiscent of the positive curvature observed in $H_{c2\perp}(T)$ (Figure 6.11). Since there was only a single Nb layer in the sandwich films, the curvature of $H_{c2\|}$ must be related to the penetration of superconductivity into the N layer. It is intriguing, though, that in the current case curvature became more pronounced as d_s was decreased, whereas the curvature of $H_{c2\perp}(T)$ became more pronounced as d_s was increased. This effect is not understood at any level.

For fixed d_s (28.0 nm) $H_{c2\|}(T)$ showed a kink at T^* for all d_n and N layer materials studied, provided $d_n < d_{nc}^*$, as was shown in Figures 6.24, 6.27, 6.29, and 6.30. For small d_n, the kink was barely discerned. As d_n was increased, the kink at T^* became more pronounced and $H_{c2\|}(0)$ was observed to decrease.

$H_{c2\|}(T)$ in the 2D state for non-magnetic interlayered samples was roughly independent of d_n for $d_n \geq 40$ nm for Cu (Figure 6.32), and 20 nm for CuGe (Figure 6.27)

interlayers. This implied that, in these systems the S layers are fully isolated from one another below T^*. $H_{c2\|}$ in the 2D state for Nb/CuMn multilayers, however, changes with increasing d_n until $d_n > d_{nc}^*$ (Figure 6.29). In addition, in Nb/CuGe multilayers having d_s = 10 nm, $H_{c2\|}(T)$ within the 2D state is dependent on d_n for d_n up to 70 nm (Figure 6.25). This implies that the 2D state may not always be indicative of a total decoupling of the S layers.

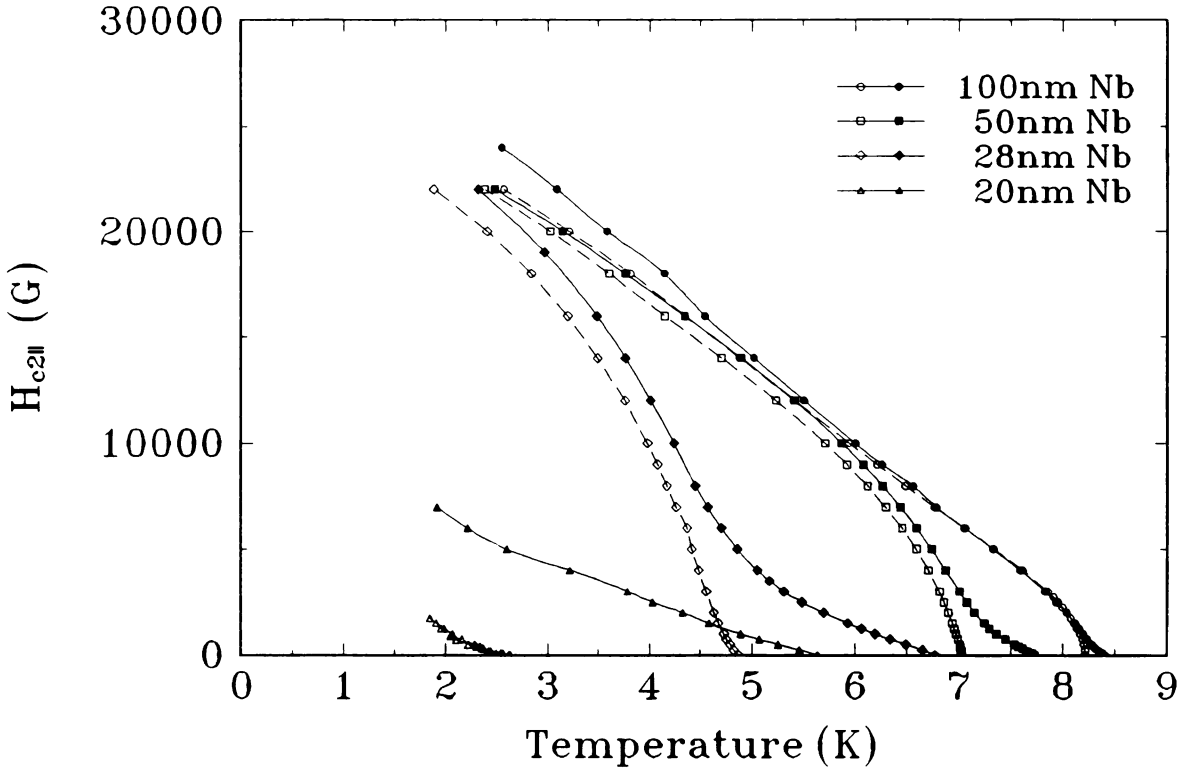

Figure 6.31: $H_{c2\|}(T)$ for Nb/Cu multilayers with d_n = 40 nm (filled symbols) and Cu/Nb/Cu sandwiches with d_n = 300 nm (open symbols).

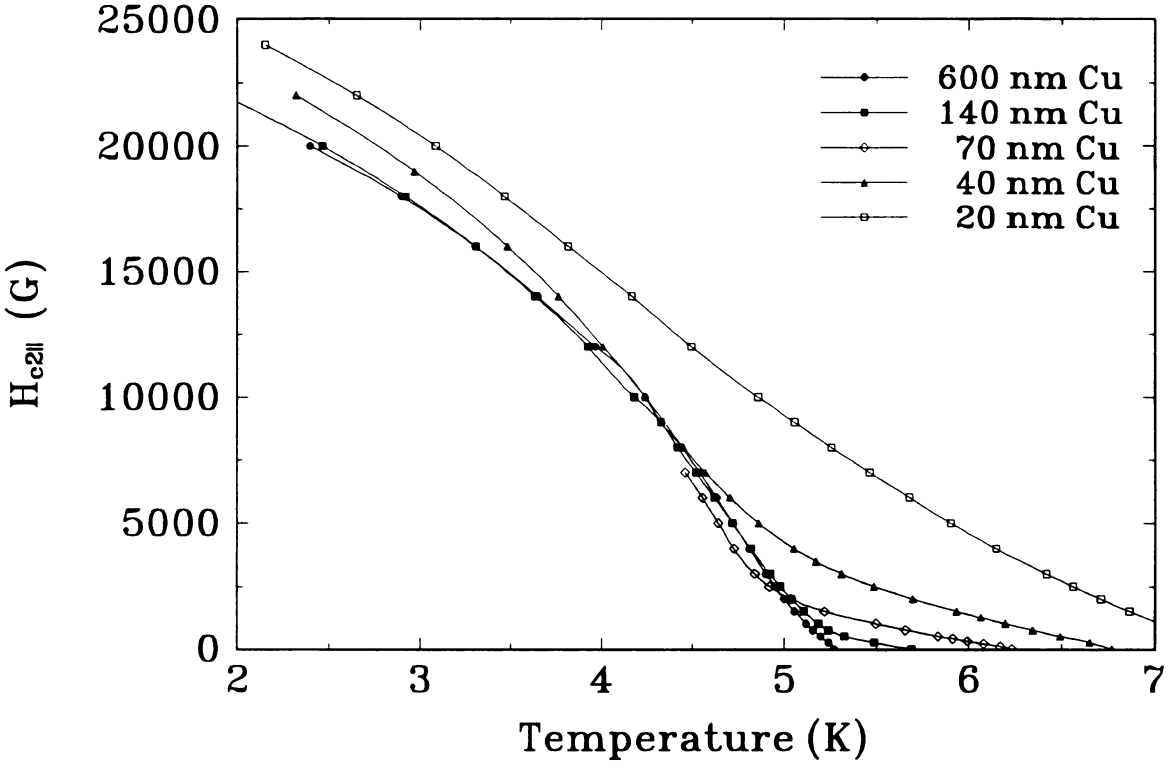

Figure 6.32: Expanded view of $H_{c2\|}(T)$ for Nb/Cu multilayers with d_s = 28 nm.

6.3.2 $H_{c2\|}(T)$ Models

Two qualitative models have been developed to model the occurrence of dimensional crossover. The temperature quenched (TQ) model, introduced by Chun et al.,[24] was based on theoretical studies of S/I multilayers where coupling is due to pair tunneling through the insulating I layer. This S/I model was the only theory available at the time which predicted dimensional crossover in any superconducting multilayered system. The field quenched (FQ) model will be developed below to solve some of the problems encountered when the TQ model was applied to our $H_{c2\|}(T)$ data. The TQ model will be discussed first, followed by an analysis of the experimental data for Nb/CuX multilayers. Then, the FQ model will be introduced and its predictions will also be compared to the same data. Following this section, both models will be compared to recent data taken by Koorevaar et al. on Nb/NbZr multilayers[59] in an effort to establish which model more appropriately describes the mechanism behind dimensional crossover in superconducting multilayers.

6.3.2.1 The TQ Model

This model relates the occurrence of dimensional crossover to the temperature dependence of ξ_z. Chun et al. argued that when ξ_z became approximately equal to d_n, superconductivity was no longer coherent across the N layer, hence leading to a decoupling the S layers.[24] Recent experimental studies by Kanoda et al.,[25] however, indicate that crossover occurs when ξ_z is approximately equal to the bilayer repeat distance $\Lambda = d_s + d_n$.

Chun et al. originally proposed this model to describe their observed dependence of dimensional crossover on the S and N layer thicknesses in Nb/Cu multilayers[24] while Kanoda et al. studied V/Ag multilayers.[25] Both groups assumed that dimensional

crossover behavior in S/N multilayers is similar to that found in S/I multilayers. Klemm, Luther, and Beasley had previously developed a theoretical model for evaluating $H_{c2\|}(T)$ in S/I multilayers.[60] The KLB model shows that near T_c, $\xi_z^{3D}(T)$ varies as $(T_c - T)^{-1/2}$ until $\xi_z^{3D}(T)$ becomes approximately equal to $\Lambda/\sqrt{2}$, T^* was then defined as the temperature at which $\xi_z^{3D}(T) = \Lambda/\sqrt{2}$. As T decreases below T^*, ξ_z approaches $d_s/\sqrt{12}$, indicative of an isolated 2D S layer. Since the TQ model links crossover to the temperature dependence of ξ_z, it predicts that the 2D state extends down to zero applied magnetic field as shown in Figure 6.33.

This model also predicts that $\xi_{\|} \cong \xi_{xy}$ and hence that there is no change in the behavior of ξ_{xy} below the crossover point. This assumption provides a means to extract the value of ξ at the crossover temperature ξ^* from the $H_{c2\|}(T)$ and $H_{c2\perp}(T)$ data. Chun et al. performed this extraction and found that for d_s and d_n greater than ~15 nm, the data were roughly consistent with the TQ model. One drawback of their experiment was that they typically studied multilayers having $d_s = d_n$. This made it difficult to determine whether ξ^* was dependent only on Λ, independently on d_s and d_n. In addition, for small Λ they found that ξ^* was not simply related to Λ, however, they did not speculate on a reason for this discrepancy.

Using this model, ξ^* was extracted from our data for H_{c2} in Nb/CuX multilayers with the results shown in Figure 6.34. Note here that, although ξ^* does depend on Λ, it is usually less than $\Lambda/\sqrt{2}$ and for the Nb/CuMn(0.3%) series with fixed d_s, ξ^* appears to be nearly independent of Λ.

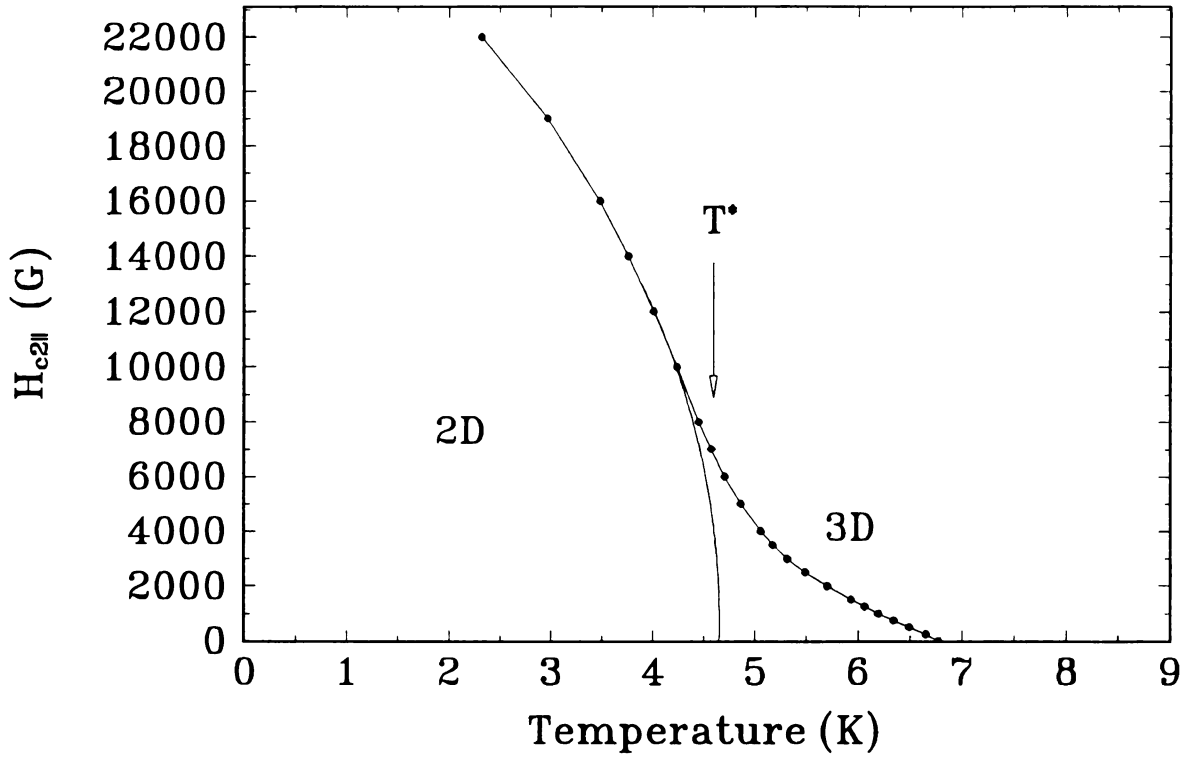

Figure 6.33: $H_{c2\|}(T)$ for Nb/Cu 28 nm/40 nm and the extension of the 2D state predicted by the FQ model.

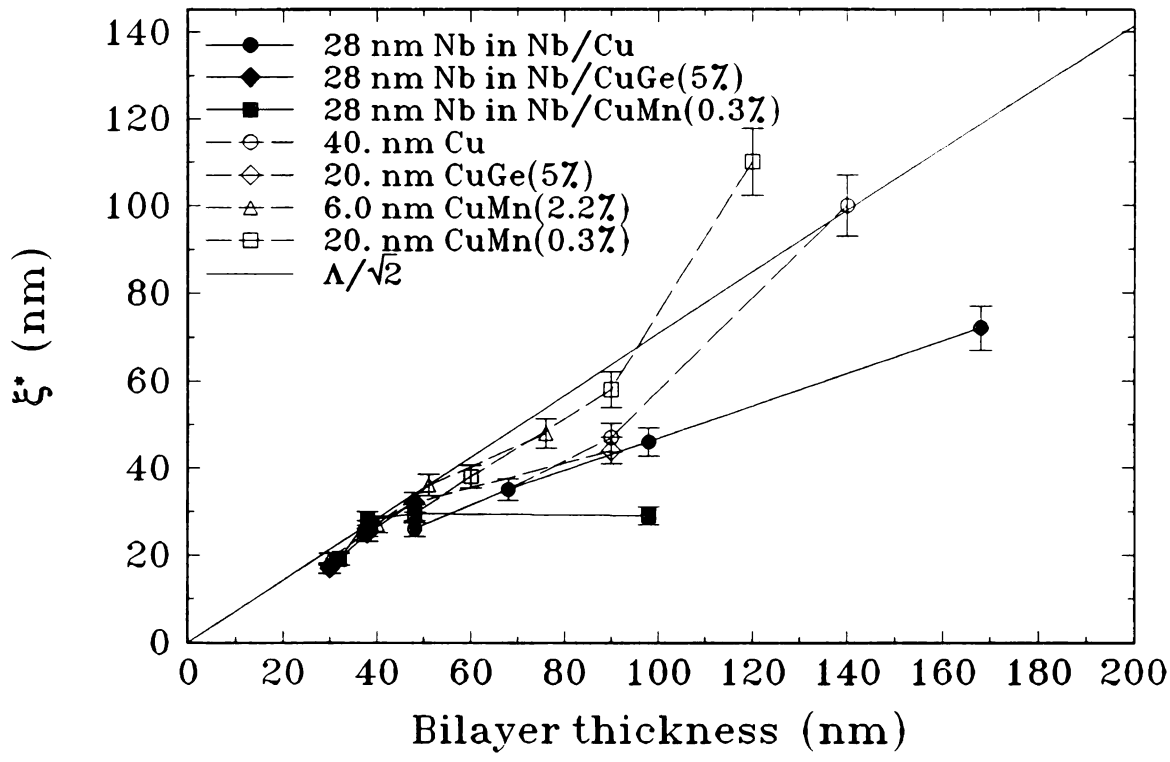

Figure 6.34: ξ^* as a function of Λ for various CuX layers and Nb and CuX layer thicknesses.

6.3.2.2 The FQ Model

Another possible decoupling mechanism relates the application of a field parallel to the layers to the decoupling of the layers. In this model a magnetic field parallel to the layers will be shown to selectively quench superconductivity in one of the materials in a superconducting multilayer. To properly develop a mechanism for field induced decoupling, the definition of the superconducting coherence length will first be reexamined. Then the averaging processes leading to ξ_z, ξ_{xy}, and $\xi_{\|}$ will be examined. Finally, it will be shown that a steadily increasing magnetic field density can destroy the induced superconductivity in N without destroying the superconductivity in S.

There are two general ways to estimate ξ within the S and N layers. In the first, ξ_s and ξ_n can be directly calculated using the equation:

$$\xi_i^2 \cong \frac{\pi\hbar k_b}{6e^2 T}\frac{1}{\gamma_i \rho_i} \tag{6.38}$$

where i stands for the S or N material and the other terms are defined in the $H_{c2\perp}(T)$ section. T in Equation (6.38) is defined as T_c^b for Nb, while for CuX, T is a free variable. Typically, one uses the highest temperature of interest to provide the smallest possible estimate of ξ_n, here T_c^b was used. Using values for γ_i and ρ_i given in the Table 5.2, ξ_s is approximately 11 nm and ξ_n varies from 85 nm to 14 nm as the N layer is changed from Cu to CuGe(5%). Hence, in all cases ξ_n is greater than ξ_s.

Another way to estimate ξ in the S and N layers is to use Equation (6.3).

$$\xi = \frac{\hbar v_f}{\pi\Delta} \tag{6.3}$$

In a non-superconducting material $\Delta = 0$, while the superconducting pair function F ($F \equiv \Delta /V$, where V is the electron phonon coupling parameter) is non-zero. Therefore, proximity effect models, typically replace Δ by F which implies that $\xi \propto 1/F$. F is proportional to the phase coherent electron density in the S and N layers and varies with position roughly as shown in Figure 6.35. Again, ξ should always be larger in N than in S independent of the thickness of the S and N layers.

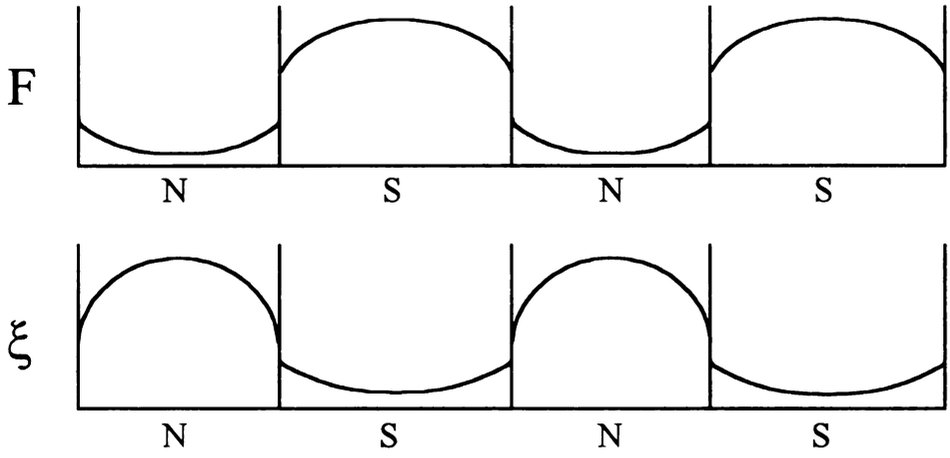

Figure 6.35: Schematic diagram of F and ξ as a function of position perpendicular to the layers of an S/N multilayer.

For a vortex penetrating an S/N multilayer, ξ_{xy}, ξ_z, and $\xi_{\|}$ represent different averages of ξ_n and ξ_s within the multilayer. $\xi_{\|}$ will always be related to an average of ξ_n and ξ_s within the entire sample, since each vortex passes through every layer. ξ_{xy} and ξ_z on the other hand average only over ξ_n and ξ_s in the vicinity of the core of the vortex. When ξ_{xy} and ξ_z are >> Λ (either near T_c, or in samples with very small Λ), they will effectively average over many S and N layers, and hence should be relatively unaffected by the discreet nature of the N and S layers. Therefore, in this regime $\xi_{xy} \sim \xi_{\|}$ and ξ_z, ξ_{xy}, and $\xi_{\|}$ should all be proportional to $(T_c\text{-}T)^{-1/2}$. As ξ_{xy} and ξ_z decrease, or Λ increases, they will become distorted by the influence of the layering. ξ_z, which typically averages over a few

S and N layers, will not be strongly affected by the layer in which the core of the vortex resides. ξ_{xy}, on the other hand, will be dominated by the value of ξ near the center of the vortex. For a vortex nucleated in the S and N layers respectively, the approximate cores are sketched in Figure 6.36. To reduce their condensation energies, the vortices will tend to nucleate at positions of lowest pair density, hence at the centers of the N layers. Therefore, ξ_{xy} will be dominated by ξ_n.

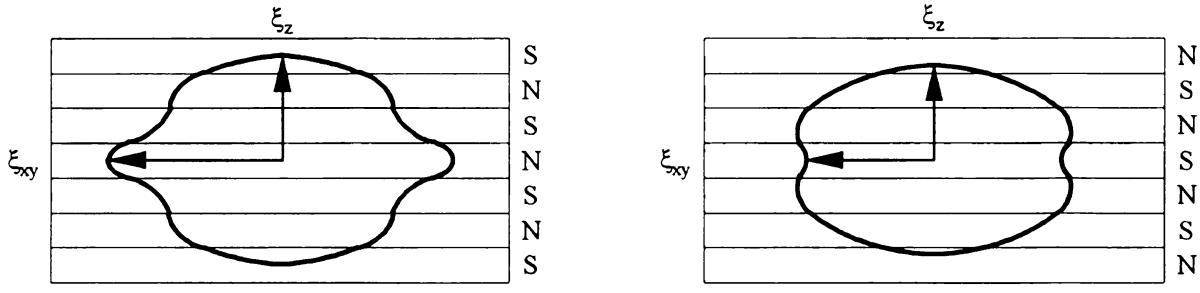

Vortex nucleated in N

Vortex nucleated in S

Figure 6.36: Approximate vortex cores for external fields directed parallel to the layers.

At low field densities there are two main factors which regulate the spacing and structure of the vortices:

First, there is the position dependence of the vortex nucleation energy. As discussed above, for an isolated vortex, the minimum energy position is at the center of a N layer. Therefore, the vortex structure will attempt to maximize the fraction of vortices which sit near the centers of the N layers.

Second, there is the anisotropy of the magnetic penetration depth. Far from the core of a vortex, the magnetic field density in a superconductor is related to the magnetic penetration depth λ, therefore, the magnetic repulsion between two vortices will also depend on λ. The anisotropy of λ in S/N multilayers has not received a great deal of experimental or theoretical attention, therefore, good models for predicting the magnitude

of the anisotropy do not exist. To obtain some measure of the anisotropy of λ, it was assumed that the anisotropy in a S/N multilayer would be less than the anisotropy of a single S film. For such a film, the ratio of the in-plane magnetic penetration depth λ_{xy} to the perpendicular magnetic penetration depth λ_z in the limit that $\xi_{xy} >> \xi_z$, is given by[61]

$$\frac{\lambda_{xy}}{\lambda_z} \cong \left[\frac{4}{3}\ln\left(\frac{\xi_{xy}(0)}{\xi_z(0)}\right)\right]^{1/2} \tag{6.39}$$

In the 3D regime very near T_c, ξ_{xy}/ξ_z can be approximated by $H_{c2\parallel}/H_{c2\perp}$ which is typically less than 4. This leads to λ_{xy}/λ_z less than 1.8. Hence, λ is fairly isotropic. This implies that the magnetic repulsion should be isotropic and the vortex lattice should also be isotropic.

Therefore, in small applied external fields, the vortex lattice should be fairly isotropic provided that the fraction of vortices centered in N layers is kept high. This leads to a vortex packing arrangement similar to that sketched in Figure 6.37. The approximate vortex cores are also illustrated in this figure.

As H increases, the vortex-vortex spacing decreases fairly uniformly until the spacing along the N layers becomes roughly equal to ξ_{xy}. When this occurs, the vortices will overlap within the N layers thereby destroying the induced superconductivity in N. Note, however, that when this occurs ξ_z remains less than the vortex spacing perpendicular to the layers, and so, superconductivity will not be destroyed in S. Once the superconductivity in N is destroyed, the S layers become decoupled and ξ_{xy} and ξ_z should change fairly abruptly to values characteristic of isolated S layers. Therefore, the FQ model predicts that the 3D to 2D crossover occurs as the magnetic field is increased. This leads to an extension of the 3D state shown approximately in Figure 6.38.

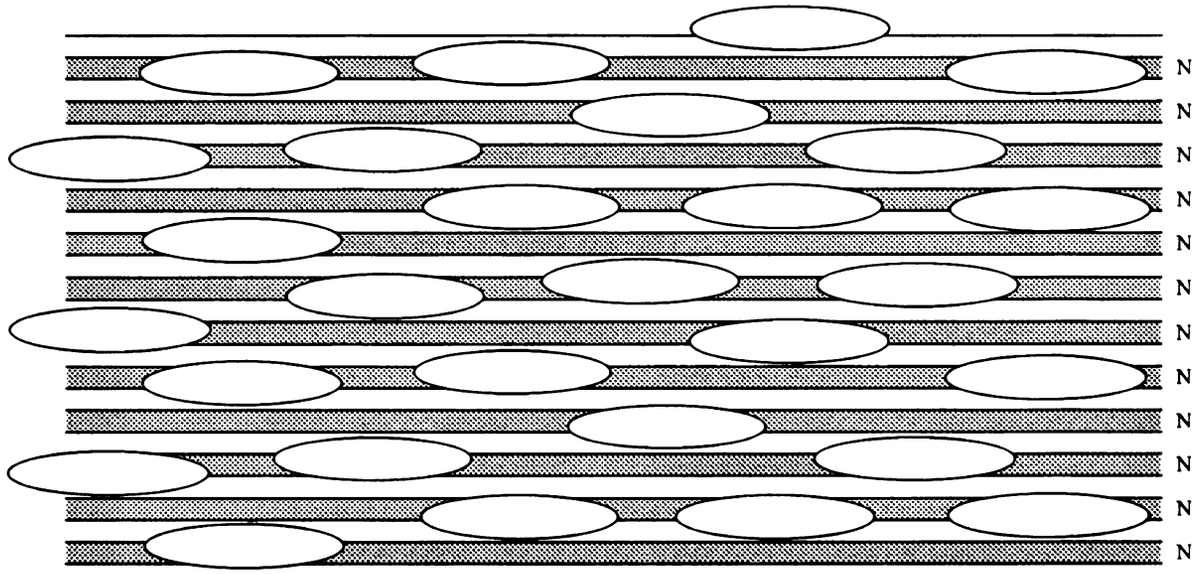

Figure 6.37: Approximate vortex structure in a S/N multilayer.

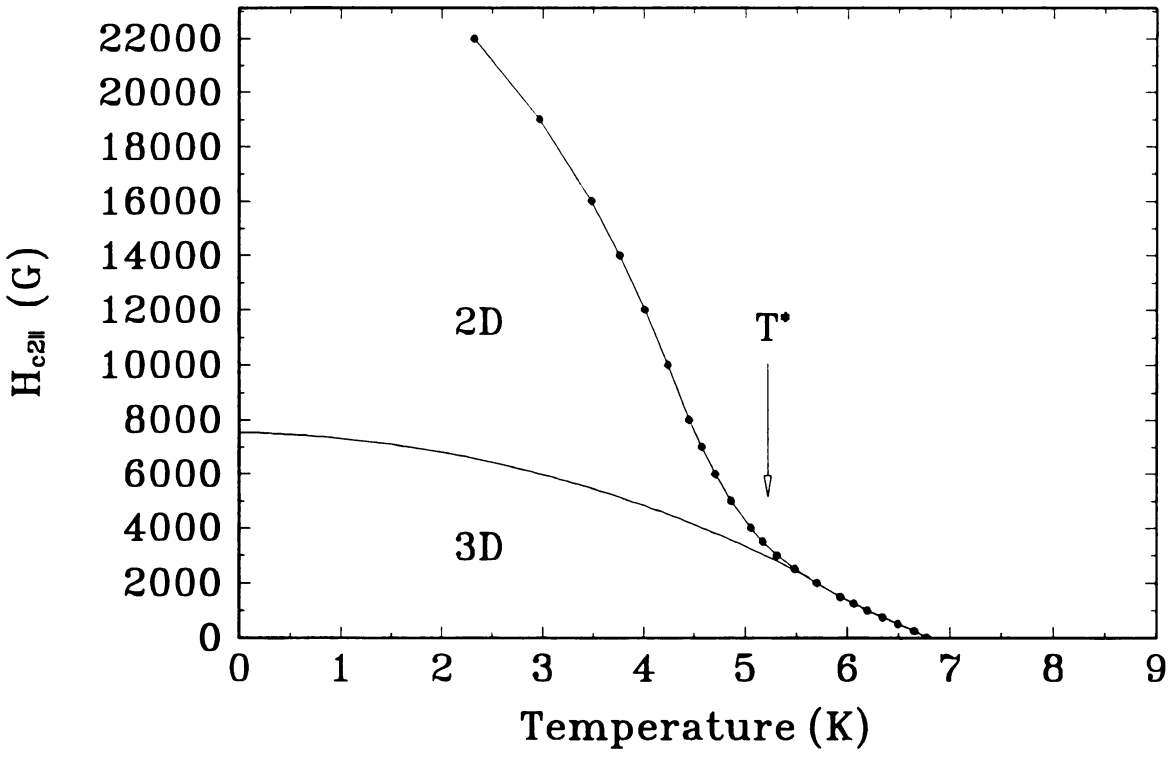

Figure 6.38: $H_{c2\parallel}(T)$ for Nb/Cu 28 nm/40 nm and the extension of the 2D state given by the FQ model.

The FQ model, predicts that dimensional crossover is predominantly related to $\xi_{xy}(T^*)$ provided that ξ_z is of the order of Λ. Therefore, ξ_z and Λ are related, but not in any analytic fashion. This concurs with the observation that ξ^* may or may not depend on Λ, (Figure 6.34). In addition, this model predicts that near and below crossover $\xi_{xy}(T)$ and $\xi_{\|}(T)$ are unrelated to one another. Hence, the change in the temperature dependence of $\xi_{xy}(T)$ will not effect the temperature dependence of $\xi_{\|}(T)$ or $H_{c2\perp}(T)$. Therefore, the data for $H_{c2\|}$ and $H_{c2\perp}$ in Nb/CuX multilayers qualitatively supports the validity of the FQ model over the TQ model in providing a mechanism for the occurrence of dimensional crossover.

Recent experiments by Koorevaar et al. also support the FQ model.[59] Their experiments focused on studies of the critical current $J_c(T, H)$ for T and H below the $H_{c2\|}(T)$ line. Their studies of $Nb/Nb_{0.5}Zr_{0.5}$ multilayers (where both the Nb and NbZr layers are bulk superconductors with $T_c^{Nb} \cong T_c^{NbZr}$) located two transitions in the vortex pinning potentials as H was increased.

At low field densities, they found that the vortices were not strongly pinned by the internal layering of the sample for any temperature below T_c. For H greater than H^*, J_c displayed behavior indicating that the vortices had become pinned within the Nb layers. Above a yet higher field density H^{**} the vortices shifted to lie within the NbZr layers.

The change in pinning sites was related to changes in the nucleation points for vortices penetrating the sample. Koorevaar argued that below H^* the vortices were not strongly pinned since ξ_z was large enough to average over many Nb and NbZr layers. This state is similar to the 3D-coupled state described above in Nb/CuX multilayers. Above H^*, the vortices became pinned within the Nb layers since Nb has a larger coherence length than NbZr. Hence, here Nb plays a role similar to the N layer in a S/N multilayer. Eventually, at H^{**} the superconductivity of the Nb layers was destroyed, leaving only isolated vortices in the NbZr layers.

By analogy, one may expect that in an S/N multilayer, H^* and H^{**} would roughly coincide leading to a single crossover line, as was observed in Nb/CuX. The TQ model cannot explain any of the features found in the Nb/NbZr data and so is not likely to be the decoupling mechanism operating in S/N multilayers.

CHAPTER 7
SPIN-FREEZING NEAR T_c

As discussed in the introduction, searches for interplay between superconducting (SC) and magnetic ordering have been driven by the very fact that magnetism tends to strongly attenuate superconductivity. Previous studies have definitively shown coexistent magnetic and superconductive order only in ternary rare earth (RE) alloys.[2] Recent searches for SC and magnetic order in transition metal systems have focused on superconducting/ferromagnetic multilayers.[2,4,5] Here, the magnetism and superconductivity are physically separated enough for both phase transitions to exist. While superconductivity has been observed at temperatures well below the magnetic phase transition T_f, the ferromagnetic state has not been studied at temperatures in the vicinity of T_c. It is this regime, where $T_f \sim T_c$, that the largest interactions between the ordered states are expected. In addition, coupling between S layers is very weak due to pair breaking by the ferromagnetic layers. This required very thin (~ .2 to 2 nm) ferromagnetic layers be used to observe any significant level of proximity effect coupling between S layers. At these layer thicknesses, fabrication problems related to layer thickness uniformity and growth become critically important. In addition, T_f only changes appreciably for very thin ferromagnetic layers. In Ni, T_f changes from 450 K at d_{Ni} = 2.5 nm to 0 K for d_{Ni} = 0.7 nm.[62] Hence, study of the regime where $T_c \sim T_f$ is virtually impossible using ferromagnetic layers.

To avoid some of these problems, superconducting/spin-glass (SC/SG) Nb/CuMn(1%) multilayers have been examined. Spin-glass magnetic layers offer four primary advantages over ferromagnetic layers: 1) CuMn(1%) is a dilute magnetic alloy and so has significantly fewer magnetic spins to scatter and destroy proximity induced pairs; 2) The spin-glass phase transition has no spontaneous moment, therefore, increased scattering caused by a spontaneous magnetization (as occurs for ferromagnets) will not occur; 3) The spin-freezing temperature of CuMn(1%) (11 K) is approximately equal to

the bulk superconducting transition temperature of Nb (9 K); 4) The spin-freezing temperature T_f is strongly dependent on the CuMn layer thickness for d_{CuMn} less than 25 nm,[9] therefore spin-glasses offer much more flexibility in setting T_f.

In the RE based systems, two general experiments were used to determine if coexistence occurred. First, T_c and T_f were measured for increasing values of the magnetic impurity concentration *y*. As *y* increased, T_f increased and T_c decreased. When $T_c \sim T_f$, T_c was often observed to drop precipitously to zero, or in some cases to show a "reentrant" behavior where at a temperature below T_c superconductivity was destroyed. These anomalies were shown to be related to the interplay of the magnetic and superconductive ordering. Hence, a drop in T_c when T_c is expected to be near T_f could signal a coexistent state. Second, the superconducting upper critical field $H_{c2}(T)$ of the RE alloys was found to drop in field for temperatures below T_f. Here T_f was measured at temperatures below T_c using neutron diffraction or Mössbauer measurements, and was found to correlate strongly with the observed decrease in $H_{c2}(T)$. In CuMn, T_f is strongly depressed and broadened by the application of magnetic fields larger than 1000 gauss. Since $H_{c2}(T)$ for Nb and Nb/CuX multilayers was found to be 10,000 to 50,000 gauss at low temperatures, $H_{c2}(T)$ experiments are unlikely to show evidence of coexistent behavior in Nb/CuMn multilayers.

As discussed in the experimental procedures chapter, T_f was measured magnetically while T_c was measured resistively. The problem here is that at temperatures below T_c, superconducting surface currents form which shield the interior of the sample from weak external fields, such as the T_f probe field. Therefore, T_f could not be measured for temperatures below T_c. Because of this dilemma, we focused on the layer thickness regime where T_f was expected to be greater than or equal to T_c. At temperatures above T_c, superconducting fluctuations occur which can couple to the magnetic state.

Previous studies of Nb/CuMn(*y*) multilayers have shown that T_f decreases with decreasing CuMn layer thickness similar to what was observed for Cu/CuMn multilayers.[9]

These studies also found that T_f is nearly independent of d_{Nb} for d_{Nb} greater than about 7 nm. Therefore, the search for changes in T_f in the vicinity of T_c were made for various series having fixed CuMn layer thickness, and hence fixed T_f, and varying Nb layer thickness. Any deviation observed would then almost necessarily be related to the superconducting state.

Figure 7.1 shows data for T_f and T_c vs. CuMn layer thickness at several values of the Nb layer thickness. As was expected, the T_f values follow nearly the same general curve independent of the Nb layer thickness used in the multilayers. The one exception to this trend is the Nb/CuMn(1%) 28.0 nm/6.0 nm sample. T_f for this sample is anomalously high by about 0.7 K. Given that the uncertainty in T_f is 0.5 K, this shift is just barely significant.

T_c is also observed to decrease with decreasing CuMn layer thicknesses for $d_{CuMn} < 20$ nm. This implies that superconductivity is induced throughout the CuMn layers for $d_{CuMn} < 20$ nm. Note, however, that there were no deviations in the T_c data as T_c was decreased to below T_f. This indicates that the spin-glass freezing transition has no effect on T_c.

Figure 7.2 shows the same data as in Figure 7.1 replotted to display T_f and T_c as functions of the Nb layer thickness at various constant values of the CuMn thickness. Here, T_f was observed to be independent of d_{Nb}, except for the $d_{CuMn} = 6.0$ nm series. This series shows a slight increase in T_f in the layer thickness regime where one expects $T_f \sim T_c$. M(T) for the Nb/CuMn(1%) 40.0 nm/6.0 nm, 28.0 nm/6.0 nm and 20.0 nm/6.0 nm samples are shown in Figure 7.3. The 40 nm sample shows that when $T_f << T_c$, there is no rounding of M(T) above T_c, as occurred for the 28 nm sample. Hence, the apparent shift in T_f of the 28.0 nm sample is not related to weak diamagnetism of the superconducting state above T_c.

One possible explanation for this shift is that the CuMn layer thickness was larger than expected. However, the CuMn layer thickness would have to be increased by about

30% to account for the observed change in T_f. The structural measurements of these samples show that such a change did not occur.

Therefore, fluctuation superconductivity for $T > T_c$ may be causing an increase in the effective spin-freezing temperature. In the present case, T_f was observed to increase by 0.7 K, when T_c was increased to just below the expected value of T_f. Further experiments are needed, however, to prove that fluctuation superconductivity, rather than some systematic artifact, is the cause of the observed change in T_f.

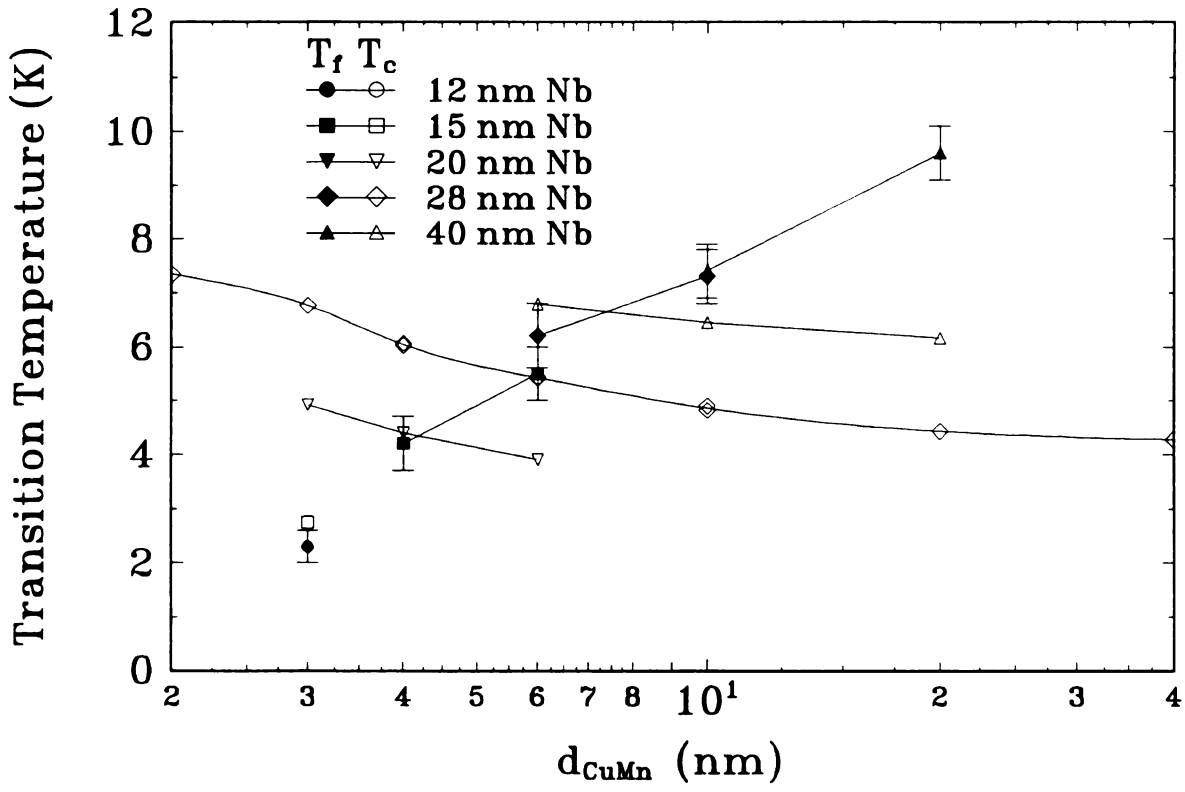

Figure 7.1: T_c (open symbols) and T_f (filled symbols) as functions of d_{CuMn} for various constant values of d_{Nb}.

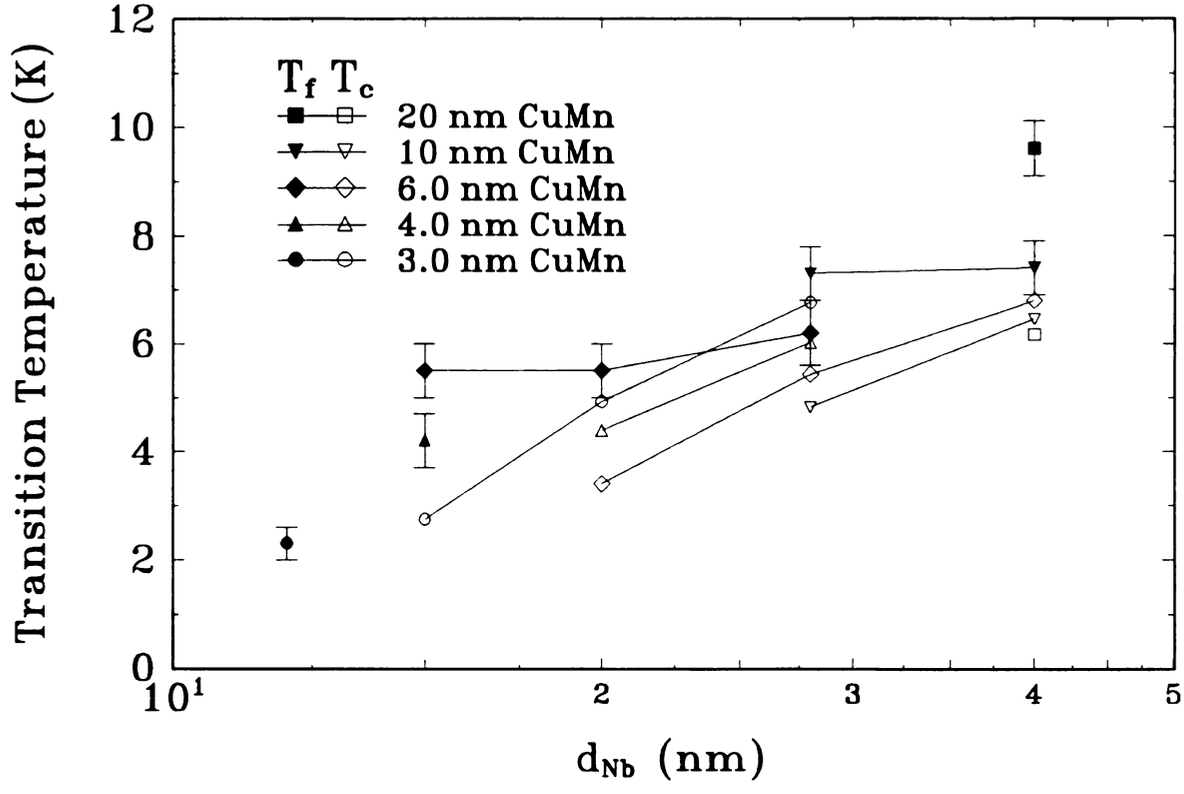

Figure 7.2: T_c (open symbols) and T_f (filled symbols) as functions of d_{Nb} for various constant values of d_{CuMn}.

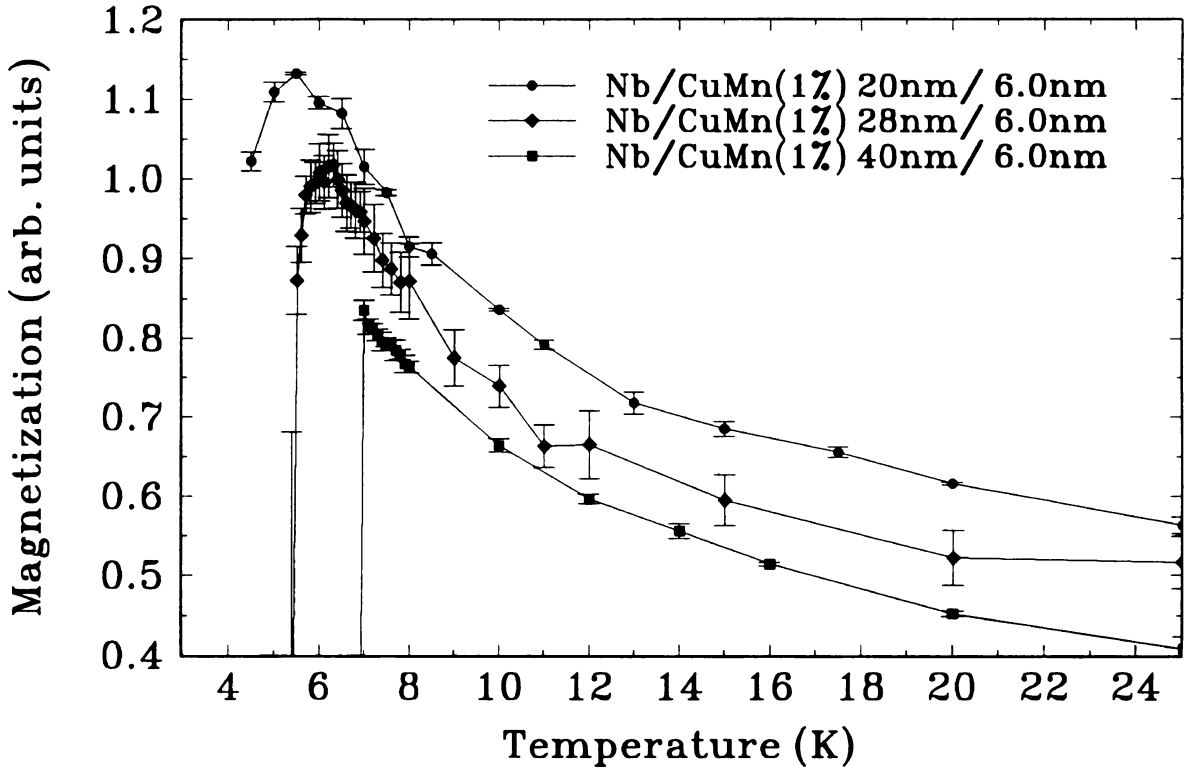

Figure 7.3: Zero-field-cooled magnetization data for three Nb/CuMn(1%) samples having d_{CuMn} = 6.0 nm. T_f is defined as the temperature at the peak of the zero-field-cooled magnetization.

CHAPTER 8
CONCLUSIONS

In this thesis, samples consisting of alternate layers of Nb and either pure Cu or Cu with a few percent Mn or Ge have been used to study the effects of magnetic interlayers on the superconducting properties of proximity coupled multilayers.

Structural analyses of these multilayers have shown that, other than a decrease in the mean crystallite size, there are no significant changes in the internal structure or the uniformity of the layering as the Nb and CuX layer thicknesses are decreased. For the thinnest Nb and CuX layers studied, there are some indications that their lattice spacings are different from those of bulk materials. However, the resolution of these experiments was not high enough to tell for certain.

The superconducting experiments focused on studies of how the superconducting transition temperature T_c and the superconducting upper critical field, H_{c2} depend on the Nb layer thickness d_s, the CuX layer thickness d_n, the impurity concentration, and the electron mean free path ℓ_n.

Many of the effects observed in the behavior of T_c have been attributed to how the proximity effect leads to an increase in the pair density in N, as well as a decrease in the pair density in S. In N, the type and concentration of impurities determine how the pairs are scattered. This leads to three limiting cases for a superconducting pair in N:

1. If $\ell_n > d_n$, electrons are not strongly scattered in N, and the probability for superconducting pairs to cross N is high. This leads to strong superconductive coupling between adjacent S layers and a T_c which approximately equal to the effective bulk transition temperature of S.
2. If $\ell_n < d_n$ due to scattering from magnetic impurities, superconducting pairs are broken as they travel in N. Hence, as the magnetic ion concentration is

increased, both the superconducting pair penetration depth and the superconducting transition temperature decrease.

3. If $\ell_n < d_n$ and there are no magnetic impurities present, the superconducting pairs are coherently backscattered in to the S layers. Therefore, as ℓ_n decreases, the superconducting pair density in S increases, the pair penetration depth in N decreases, and T_c is observed to increase.

All three of these behaviors have been observed and carefully studied in the Nb/CuX samples.

For a given N layer thickness and impurity concentration, T_c is observed to scale with d_s. The scaling exponent was found to depend strongly on the N layer thickness and the concentration of magnetic impurities, but was insensitive to changes in the concentration of nonmagnetic impurities. While scaling was found to be consistent with the limiting forms of two theoretical models, an additional dependence of the effective bulk transition temperature of Nb on d_s had to be included for the models to quantitatively predict the behavior of T_c for thin S and N layers.

The dependence of the upper critical field H_{c2} on the layer parameters and on the relative orientation of the applied field and the sample have proven quite complex and difficult to interpret. Both $H_{c2\parallel}$ and $H_{c2\perp}$ are related to a set of superconducting coherence lengths which are only partially related to one another.

The behavior of $H_{c2\perp}$ is very similar to that observed for T_c. There were some indications, however, that $H_{c2\perp}$ and T_c measure slightly different length scales in the N layer. Scaling of $H_{c2\perp}$ with d_s, supported by previously published studies, was not well established in Nb/CuX.

$H_{c2\parallel}(T)$ was observed to change from behavior indicative of a 3D coupled state near T_c, to a 2D decoupled state at a temperature where ξ_z is less than or equal to the bilayer thickness, to a 'bulk' state at still lower temperatures where both ξ_{xy} and ξ_z are small compared to any dimension of the layers.

These $H_{c2\|}$ results were interpreted in terms of two qualitative decoupling models, the temperature quench (TQ) model, and the field quench (FQ) model. The TQ model linked the decoupling transition to the temperature dependence of ξ_z. Therefore, it predicted that crossover occurs even in zero applied magnetic field. In the FQ model, on the other hand, the application of a magnetic field parallel to the layers was argued to preferentially destroy the induced superconductivity in N, thereby decoupling the S layers. Hence, the FQ model predicts that in zero applied field, a 3D coupled state exists at all temperatures. While the present data on Nb/CuX multilayers qualitatively support the validity of the FQ model over that of the TQ model, more studies still need to be performed.

As to the question of whether there are any significant interactions between the proximity induced superconducting and spin-glass states, the answer appears to be "possibly". While there are no significant deviations in T_c or $H_{c2}(T)$ in the vicinity of the spin freezing temperature T_f, a change in T_f due to fluctuation superconductivity above T_c may have been found. The results, however, are very speculative at this point, and a much more through study the spin-glass state in the vicinity of T_c is needed.

8.1 Future Directions of Study

Electron microscopy and electron diffraction studies of cross sections of multi-layers having thin Nb and Cu X layers are needed to accurately determine if there are lattice strains in either the Nb or CuX layers at small layer thicknesses.

In order to carefully study the dependence of T_c on d_n in the limit that $d_n \rightarrow 0$, experiments over a wider range of d_s are needed. These experiments should be able to then determine if the dependence of $T_c(d_n \rightarrow 0)$ on d_s is due to broadening of the Nb density of states or to some other structural effect.

In this same vein, studies of V/CuX multilayers would also be informative since V does not have a density of states peak near the Fermi energy and so in not susceptible to a change in T_c due to decreasing ℓ_n. Therefore, V/CuX multilayers would provide a more accurate test of the validity of the various proximity effect models and of the occurrence of a scaling of T_c with d_s.

Annealing studies of Nb/CuX multilayers can also be used to determine if the dependence of $T_c(d_n \rightarrow 0)$ on d_s is related to structural disorder. Nb and Cu are mutually immiscible, therefore annealing should lead to an improvement in their layering, an increase in their in-plane crystallite size, and hence, an increase in ℓ_s.

The FQ model for dimensional crossover needs to be checked by critical current measurements similar to those used by Koorevaar et al.[59] In addition, there is the possibility of examining the critical current of these multilayers using a current directed perpendicular to the layers. Such a system has been recently developed by Dr. William Pratt Jr. of Michigan State University to study the perpendicular resistance of a sample at fields up to 5 kG.[63] Such an experiment would provide a much cleaner test of the decoupling phenomenon since the multilayered sample can then be treated as a set of resistors in series rather than in parallel. Hence, one should be able to infer the resistance of the center of the N layer which is driven normal by the application of the applied magnetic field.

LIST OF REFERENCES

LIST OF REFERENCES

[1]For a good review of RE based magnetic superconductors see: S. Roth, Appl. Phys. **15**, 1 (1978), or M. Ishikawa, Contemp. Phys. **23**, 443 (1982).

[2]H. K. Wong, H. Q. Yang, B. Y. Jin, Y. H. Shen, W. Z. Cao, and J. B. Ketterson, J. Appl. Phys. **55**, 2494 (1984).

[3]H. K. Wong, B. Y. Jin, H. Q. Yang, J. B. Ketterson, and J. E. Hilliard, J. Low Temp. Phys. **63**, 307 (1985).

[4]H. Homma, C. S. L. Chun, G.-G. Zheng, and I. K. Schuller, Phys. Rev. B **33**, 3562 (1986).

[5]K. Kawaguchi, M. Sohma, Phys. Rev. B **46**, 14722 (1992).

[6]J. Bass, in *Metals: Electronic Transport Phenomena*, Vol. **15a**, of *Landolt-Börnstein Tables*, New Series Group III, Edited by K. H. Helwege (Springer-Verlag, Berlin, 1982), p. 177.

[7]M. L. Wilson, R. Loloee, and J. A. Cowen, Physica B **165-166**, 457 (1990).

[8]R. Stubi, L. Hoines, R. Loloee, I. Kraus, J. A. Cowen, and J. Bass, Europhys. Lett. **19**, 235 (1992).

[9]I. K. Schuller, R. Orbach, and P. M. Chaikin, Phys. Rev. Lett. **41**, 1413 (1978).

[10]H. C. Yang, and D. K. Finnemore, Phys. Rev. B **30**, 1260 (1984).

[11]J. L. Paterson, J. Low Temp. Phys. **35**, 371 (1979).

[12]L. Dumoulin, E. Guyon, and P. Nedellec, Phys. Rev. B **16**, 1086 (1977).

[13]J. J. Hauser, H. C. Theuerer, and N. R. Werthamer, Phys. Rev. **142**, 118 (1966).

[14]M. L. Wilson, and J. A. Cowen, to be published in Phys. Rev. B **49**.

[15]I. Bannerjee, Q. S. Yang, C. M. Falco, and I. K. Schuller, Solid State Commun. **41**, 805 (1982).

[16]N. Missert, and M. R. Beasley, Phys. Rev. Lett. **63**, 672 (1989).

[17]P. R. Auvil, and J. B. Ketterson, Solid State Commun. **67**, 1003 (1988).

[18]H. Lutz, H. Weismann, M. Gurvitch, A. Goland, O. F. Kammerer, and M. Strongin, in *Superconductivity of d- and f-band Metals, - Second Rochester Conference*, edited by D. H. Douglass (Plenum, New York, 1976), p. 535.

[19]J. E. Crow, M. Strongin, R. S. Thompson, and O. F. Kammerer, Phys. Lett. **30A**, 161 (1969).

[20]Y. Asada, and H. Nose, J. Phys. Soc. Jpn. **26**, 347 (1969).

[21]W. E. Lawrence, and S. Doniach, in *Proceedings of the 12th International Conference on Low Temperature Physics (Kyoto, Japan, 1970)*, edited by E. Kanda (Keigaku, Tokyo, 1971), p. 361.

[22]P. Koorevaar, Y. Suzuki, R. Coehoorn, and J. Aarts, Phys. Rev. B **49**, 441 (1994).

[23]C. L. S. Chun, G.-G. Zheng, J. L. Vicent, and I. K. Schuller, Phys. Rev. B **29**, 4915 (1984).

[24]K. Kanoda, H. Mazaki, N. Hosoito, and T. Shinjo, Phys. Rev. B **35**, 6736 (1987).

[25]D. Neerinck, K. Temst, C. Van Haesendonck, Y. Bruynseraede, A. Gilabert, and I. K. Schuller, Phys. Rev. B **43**, 8676 (1991).

[26]K. R. Biagi, V. G. Kogan, and J. R. Clem, Phys. Rev. B **32**, 7165 (1985).

[27]S. Takahashi, and M. Tachiki, Phys. Rev. B **33**, 4620 (1986).

[28]J. M. Slaughter, W. P. Pratt, Jr., and P. A. Schroeder, Rev. Sci. Instrum. **60**, 127 (1989).

[29]Silicon Quest International, 2904 Scott Blvd., Santa Clara, CA 95054.

[30]Angstrom Sciences, P. O. Box 18116, Pittsburgh, PA 15236.

[31]Aesar/Johnson Matthey Inc. P. O. Box 8247, Ward Hill, MA 01835-0747.

[32]K. H. Fischer, *Metals: Electronic Transport Phenomena*, Vol. **15a** of *Landolt-Börnstein Tables*, New Series Group III, Edited by K. H. Hellwege (Springer-Verlag, Berlin, 1982), p. 289.

[33]G. Zibold, *Magnetic Properties of Metals*, Vol. **19b** of *Landolt-Börnstein Tables*, New Series Group III, Edited by O. Madelung (Springer-Verlag, Berlin, 1983), pp. 14 - 37.

[34]B. D. Cullity, *Elements of X-Ray Diffraction*, (Addison-Wesley, Reading, Mass., 1956) p. 99.

[35]E. E. Fullerton, I. K. Schuller, H. Vanderstraeten, and Y. Bruynseraede, Phys. Rev. B **45**, 9292 (1992).

[36]B. D. Cullity, ibid. p. 460.

[37]MacXAFS version 2 was supplied by Lars Furenlid, NSLS.

[38]Carl Foiles, personal communication.

[39]D. R. Tilley, and J. Tilley, *Superfluidity and Superconductivity*, (Adam Hilger, New York, 1990), p. 233.

[40]L. N. Cooper, Phys. Rev. Lett. **6**, 689 (1961). Actually Cooper predicts $\log(T_c^f) \propto d_s$, which simplifies to Equation (5.1).

[41]H. K. Wong, and J. B. Ketterson, J. Low Temp. Phys. **63**, 139 (1986).

[42]W. L. McMillan, Phys. Rev. **175**, 537 (1968).

[43]P. G. De Gennes and E. Guyon, Phys. Lett. **3**, 168 (1963).

[44]A. B. Kaiser, and M. J. Zuckermann, Phys. Rev. B **1**, 229 (1970).

[45]J. J. Hauser, H. C. Theuerer, and N. R. Werthamer, Phys. Rev. **136**, A637 (1964).

[46]N. R. Werthamer, Phys. Rev. **132**, 2440 (1963).

[47]C. Kittel, *Introduction to Solid State Physics*, (John Wiley, New York, 1986), p. 328.

[48]A. B. Pippard, Rept. Progr. Phys. **23**, 176 (1960).

[49]N. W. Ashcroft, and N. D. Mermin, *Solid State Physics* (Saunders College, Philadelphia, 1976), p. 49.

[50]V. G. Kogan, Phys. Rev. B **26**, 88 (1982).

[51]J. Bass, in *Metals: Electronic Transport Phenomena*, Vol. **15a**, of *Landolt-Börnstein Tables*, New Series Group III, Edited by K. H. Helwege (Springer Verlag, Berlin, 1982), p. 139.

[52]R. Hultgren, P. D. Desai, D. T. Hawkins, M. Gleiser, and K. K. Kelley, *Selected Values of the Thermodynamic Properties of the Elements*, (Am. Soc. for Metals, Metals Park, OH, 1973), p. 151.

[53]R. Hultgren, P. D. Desai, D. T. Hawkins, M. Gleiser, and K. K. Kelley, *Selected Values of the Thermodynamic Properties of Binary Alloys*, (Am. Soc. for Metals, Metals Park, OH, 1973), p. 744.

[54]$N_i(0)$ determined by H. van Leuken, A. Lodder, and R. A. de Groot, J. Phys.: Condens. Matter **3**, 7651 (1991).

[55]J. Bardeen, L. N. Cooper, and J. R. Schrieffer, Phys. Rev. **108**, 1175 (1957).

[56]M. Tinkham, *Introduction to Superconductivity* (McGraw-Hill, New York, 1975)

[57]V. G. Kogan, Phys. Rev. B **32**, 139 (1985).

[58]K. R. Biagi, V. G. Kogan, J. R. Clem, Phys. Rev. B **33**, 3100 (1986).

[59]P. Koorevaar, W. Maj, P. H. Kes, and J. Aarts, Phys. Rev. B **47**, 934 (1993).

[60]R. A. Klemm, A. Luther, and M. R. Beasley, Phys. Rev. B **12**, 877 (1975).

[61]M. Tinkham, ibid. p. 85.

[62]M. R. Khan, P. Roack, and I. K. Schuller, Thin Solid Films **122**, 183 (1985).

[63]W. P. Pratt, Jr., S.-F. Lee, J. M. Slaughter, R. Loloee, P. A. Schroeder, and J. Bass, Phys. Rev. Lett. **66**, 3060 (1991) and references therin.